Non-Local Electrodynamics of Superconducting Wires: Implications for Flux Noise and Inductance

by

Pramodh Viduranga Senarath Yapa Arachchige
B.Sc., Carleton University, 2015

A Thesis Submitted in Partial Fulfillment of the
Requirements for the Degree of

MASTER OF SCIENCE

in the Department of Physics and Astronomy

Non-Local Electrodynamics of Superconducting Wires: Implications for Flux Noise and Inductance

by

Pramodh Viduranga Senarath Yapa Arachchige
B.Sc., Carleton University, 2015

Supervisory Committee

Dr. Rogério de Sousa, Supervisor
(Department of Physics and Astronomy)

Dr. Reuven Gordon, Outside Member
(Department of Electrical and Computer Engineering)

Supervisory Committee

Dr. Rogério de Sousa, Supervisor
(Department of Physics and Astronomy)

Dr. Reuven Gordon, Outside Member
(Department of Electrical and Computer Engineering)

ABSTRACT

The simplest model for superconductor electrodynamics are the London equations, which treats the impact of electromagnetic fields on the current density as a localized phenomenon. However, the charge carriers of superconductivity are quantum mechanical objects, and their wavefunctions are delocalized within the superconductor, leading to non-local effects. The Pippard equation is the generalization of London electrodynamics which incorporates this intrinsic non-locality through the introduction of a new superconducting characteristic length, ξ_0, called the Pippard coherence length. When building nano-scale superconducting devices, the inclusion of the coherence length into electrodynamics calculations becomes paramount. In this thesis, we provide numerical calculations of various electrodynamic quantities of interest in the non-local regime, and discuss their implications for building superconducting devices.

We place special emphasis on Superconducting QUantum Inteference Devices (SQUIDs), and their usage as flux quantum bits (qubits) in quantum computation. One of the main limitations of these flux qubits is the presence of intrinsic flux noise, which leads to decoherence of the qubits. Although the origin of this flux noise is not known, there is evidence that it is related to spin impurities within the superconducting material. We present calculations which show that the flux noise in the non-local regime is significantly different from the local case. We also demonstrate that non-local electrodynamics greatly affect the self-inductance of the qubit.

Contents

Supervisory Committee ii

Abstract iii

Table of Contents iv

List of Tables vii

List of Figures viii

List of Symbols and Acronyms x

Glossary xvi

Acknowledgements xvi

Dedication xvii

1 Introduction 1

2 Background: Superconductivity and SQUIDs 3

2.1 History of Superconductivity . . . 3

2.1.1 Ginzburg-Landau Theory . . . 6

2.1.2 London's Local Electrodynamics . . . 7

2.1.3 Analogy with Screening in Electrostatics . . . 9

2.1.4 Pippard's Non-Local Electrodynamics . . . 10

2.2 The rf-SQUID as a Qubit . . . 13

2.2.1 Flux Quantization in a Superconducting Loop . . . 13

2.2.2 The Josephson Effect . . . 15

2.2.3 The rf-SQUID . . . 17

2.3 Flux, Inductance and Magnetic Energy . . . 20

2.3.1 Flux . . . 20
2.3.2 Inductance . . . 22

3 Pippard Non-Local Electrodynamics 24
3.1 Approximations and Analogues . . . 24
3.1.1 Approximation to the 3D Pippard Kernel . . . 25
3.1.2 2D and 1D Analogues to the Pippard Kernel . . . 26
3.2 Superconducting Infinite Sheet . . . 27
3.2.1 Geometry . . . 28
3.2.2 Local London Electrodynamics . . . 28
3.2.3 Non-Local Electrodynamics . . . 30
3.2.4 Results . . . 31
3.3 Superconducting Cylindrical Wire . . . 39
3.3.1 Geometry . . . 39
3.3.2 Local London Electrodynamics . . . 39
3.3.3 Non-Local Pippard Electrodynamics . . . 40
3.3.4 Non-local Vector Potential and Current Density using the 2D Pippard Kernel . . . 42
3.3.5 Non-local Vector Potential and Current Density using the 3D Approximated Pippard Kernel . . . 46
3.3.6 Internal Inductance and Kinetic Inductance . . . 50

4 Flux Noise in SQUIDs 56
4.1 Flux Vector Model . . . 56
4.2 Effect of Non-Locality . . . 57
4.2.1 Flux Vector . . . 57
4.2.2 Flux Noise Power . . . 59

5 Conclusions 61

Appendix A: Mathematical Tools 63
A.1 Fredholm Integral Equations . . . 63
A.2 Green's Functions . . . 64
A.2.1 1D Poisson equation . . . 65
A.2.2 2D Poisson equation . . . 67

Appendix B: 1D vs 2D vs 3D Pippard Kernel: Geometrical Argument 70

Appendix C: Supplementary Plots of Infinite Superconducting Wire **73**
C.1 Current Density and Vector Potential using 2D Pippard 73
C.2 Current Density and Vector Potential using 3D Approximated Pippard 74
C.3 Flux Vector and Flux Noise Power using 3D Approximated Pippard . 75

Bibliography **78**

List of Tables

Table 1.1 λ and ξ_0 length for elemental superconductors 2

List of Figures

Figure 1 A superconducting squid xvii

Figure 2.1 Temperature dependence of Superconductivity 4
Figure 2.2 Meissner Effect 5
Figure 2.3 Superconducting Loop 14
Figure 2.4 Josephson Effect 15
Figure 2.5 Schematic of rf-SQUID 18
Figure 2.6 Double well potential in an rf-SQUID 19
Figure 2.7 Flux through a loop 20

Figure 3.1 Numerical Integration vs Approximated Function 26
Figure 3.2 Geometry of the Superconducting Infinite Sheet 28
Figure 3.3 $A(y)$ Non-local Infinite Sheet: $W = 500$ nm, $\xi = 10$ nm 31
Figure 3.4 $A(y)$ Non-local Infinite Sheet: $W = 2000$ nm, $\xi = 10$ nm . . . 32
Figure 3.5 $J(y)$ Non-local Infinite Sheet: $W = 500$ nm, $\xi = 10$ nm 33
Figure 3.6 $J(y)$ Non-local Infinite Sheet: $W = 2000$ nm, $\xi = 10$ nm . . . 33
Figure 3.7 $A(y)$ Non-local Infinite Sheet: $W = 500$ nm, $\xi = 200$ nm . . . 34
Figure 3.8 $A(y)$ Non-local Infinite Sheet: $W = 500$ nm, $\xi = 1000$ nm . . . 35
Figure 3.9 $A(y)$ Non-local Infinite Sheet: $W = 2000$ nm, $\xi = 200$ nm . . . 35
Figure 3.10 $A(y)$ Non-local Infinite Sheet: $W = 2000$ nm, $\xi = 1000$ nm . . 36
Figure 3.11 $J(y)$ Non-local Infinite Sheet: $W = 500$ nm, $\xi = 200$ nm . . . 37
Figure 3.12 $J(y)$ Non-local Infinite Sheet: $W = 500$ nm, $\xi = 1000$ nm . . . 37
Figure 3.13 $J(y)$ Non-local Infinite Sheet: $W = 2000$ nm, $\xi = 200$ nm . . . 38
Figure 3.14 $J(y)$ Non-local Infinite Sheet: $W = 2000$ nm, $\xi = 1000$ nm . . 38
Figure 3.15 Infinite Superconducting Cylinder Geometry 39
Figure 3.16 $A(\rho)$ Non-local Infinite Cylinder: $R = 500$ nm, 2D Pippard . . 43
Figure 3.17 $A(\rho)$ Non-local Infinite Cylinder: $R = 1000$ nm, 2D Pippard . 43
Figure 3.18 $A(\rho)$ Non-local Infinite Cylinder: $R = 2000$ nm, 2D Pippard . 44
Figure 3.19 $J(\rho)$ Non-local Infinite Cylinder: $R = 500$ nm, 2D Pippard . . 45

Figure 3.20 $J(\rho)$ Non-local Infinite Cylinder: $R = 1000$ nm, 2D Pippard . 45
Figure 3.21 $J(\rho)$ Non-local Infinite Cylinder: $R = 2000$ nm, 2D Pippard . 46
Figure 3.22 $A(\rho)$ Non-local Infinite Cylinder: $R = 500$ nm, 3D Pippard . . 47
Figure 3.23 $A(\rho)$ Non-local Infinite Cylinder: $R = 1000$ nm, 3D Pippard . 48
Figure 3.24 $A(\rho)$ Non-local Infinite Cylinder: $R = 2000$ nm, 3D Pippard . 48
Figure 3.25 $J(\rho)$ Non-local Infinite Cylinder: $R = 500$ nm, 2D Pippard . . 49
Figure 3.26 $J(\rho)$ Non-local Infinite Cylinder: $R = 1000$ nm, 3D Pippard . 49
Figure 3.27 $J(\rho)$ Non-local Infinite Cylinder: $R = 2000$ nm, 3D Pippard . 50
Figure 3.28 L_k Non-local Infinite Cylinder: 2D Pippard 51
Figure 3.29 L_{int} Non-local Infinite Cylinder: 2D Pippard 52
Figure 3.30 L_k/L_{int} Non-local Infinite Cylinder: 2D Pippard 52
Figure 3.31 L_k Non-local Infinite Cylinder: 3D Pippard 53
Figure 3.32 L_{int} Non-local Infinite Cylinder: 3D Pippard 54
Figure 3.33 L_k/L_{int} Non-local Infinite Cylinder: 3D Pippard 54

Figure 4.1 $F_\theta(\rho)$ Infinite Cylinder: $R = 500$ nm, 2D Pippard 58
Figure 4.2 $F_\theta(\rho)$ Infinite Cylinder: $R = 1000$ nm, 2D Pippard 58
Figure 4.3 $F_\theta(\rho)$ Infinite Cylinder: $R = 2000$ nm, 2D Pippard 59
Figure 4.4 Flux Noise Power Infinite Cylinder: 2D Pippard 60

Figure A.1 Poisson's Equation on 2D Plane 68

Figure B.1 Simplified 1D, 2D and 3D Kernels 71
Figure B.2 Volume outside simplified 1D, 2D and 3D Kernels 72

Figure C.1 $A(\rho)$ and $J(\rho)$ Infinite Cylinder: $R = 5000$ nm, 2D 73
Figure C.2 $A(\rho)$ and $J(\rho)$ Infinite Cylinder: $R = 10000$ nm, 2D 74
Figure C.3 $A(\rho)$ and $J(\rho)$ Infinite Cylinder: $R = 5000$ nm, 3D 74
Figure C.4 $A(\rho)$ and $J(\rho)$ Infinite Cylinder: $R = 10000$ nm, 3D 74
Figure C.5 $F_\theta(\rho)$ Infinite Cylinder: $R = 500$ nm, 3D Pippard 75
Figure C.6 $F_\theta(\rho)$ Infinite Cylinder: $R = 1000$ nm, 3D Pippard 76
Figure C.7 $F_\theta(\rho)$ Infinite Cylinder: $R = 2000$ nm, 3D Pippard 76
Figure C.8 Flux Noise Power Infinite Cylinder: 3D Pippard 77

List of Symbols and Acronyms

In order of appearance

Chapter 1

ξ_0	Pippard coherence length in pure superconductor
SQUID	Superconducting QUantum Interference Device
$\mathbf{S}_i$	spin operator for spin impurity i
$\mathbf{R}_i$	location of spin impurity i
Φ_i	magnetic flux produced by spin impurity i
$\mathbf{F}_i$	flux vector at location $\mathbf{R}_i$
ξ	Pippard coherence length in impure superconductor
SC	superconducting
λ	superconducting penetration depth
l	electron's mean free path
rf-SQUID	radio frequency Superconducting QUantum Interference Device

Chapter 2

K	degrees Kelvin
T_c	superconducting critical temperature
ρ	electrical resistivity
GL	Ginzburg-Landau
BCS	Bardeen-Cooper-Schrieffer
$\Psi(\mathbf{r})$	superconducting order parameter (pseudo-wavefunction) at position $\mathbf{r}$
n_s	super-carrier (Cooper pair) charge density
$\boldsymbol{\nabla}$	gradient operator
e^*	Cooper pair charge, $e^* = 2e$
$\hbar$	reduced Planck constant, $\frac{h}{2\pi}$
$\mathbf{A}(\mathbf{r})$	magnetic vector potential at position $\mathbf{r}$
F_{SC}	superconducting free energy density
F_N	normal metal free energy density
α	coefficient of $\lvert\Psi\rvert^2$ in Ginzburg-Landau free energy
β	coefficient of $\lvert\Psi\rvert^4$ in Ginzburg-Landau free energy
m^*	Cooper pair effective mass

μ_0	permeability constant in vacuum
$\mathbf{B}(\mathbf{r})$	magnetic field at position $\mathbf{r}$
e	electron charge
ξ_{GL}	Ginzburg-Landau coherence length
$\mathbf{J}(\mathbf{r})$	current density at position $\mathbf{r}$
$\hat{\boldsymbol{n}}$	unit vector normal to superconductor surface
ρ_e	charge density
λ_e	electrostatic screening length
T_F	Fermi temperature
Φ_e	electrostatic potential
ϵ_0	dielectric constant in vacuum
σ	electrical conductivity
k_B	Boltzmann constant
v_F	Fermi velocity
Δp	uncertainty in momentum
Δx	uncertainty in position
a	numerical constant in Pippard coherence length
$\|\uparrow\rangle$	wavefunction of electron in spin up state
$\|\downarrow\rangle$	wavefunction of electron in spin down state
$\theta(\boldsymbol{r})$	phase of superconducting wavefunction at position $\mathbf{r}$
C	contour deep within superconductor
$\mathbb{Z}$	set of integers
Φ	magnetic flux
Φ_0	magnetic flux quantum
h	Planck's constant
Ψ_∞	wavefunction of superconductor far from Josephson junction
I_{SC}	superconducting current
I_c	critical superconducting current
E_{CP}	energy of Cooper pair
ϵ_F	Fermi energy
$V(\boldsymbol{r})$	voltage at point $\boldsymbol{r}$
E_{JJ}	energy stored in Josephson junction
E_J	magnitude of energy stored in Josephson junction
$\mathcal{H}_{SQUID}$	Hamiltonian of SQUID
L	inductance

I	current
Φ_{ext}	external magnetic flux
Q	charge operator
$\|\circlearrowright\rangle$	wavefunction of SQUID with current circulating clockwise
$\|\circlearrowleft\rangle$	wavefunction of SQUID with current circulating counter-clockwise
$\|0\rangle$	wavefunction of qubit in binary state 0
$\|1\rangle$	wavefunction of qubit in binary state 1
Φ_{11}	self-flux of circuit 1
$\boldsymbol{J}_1(\boldsymbol{r})$	current density in circuit 1 at position $\boldsymbol{r}$
$\boldsymbol{A}_{J_1}(\boldsymbol{r})$	vector potential from current density in circuit 1 at position $\boldsymbol{r}$
$\boldsymbol{B}_{J_1}(\boldsymbol{r})$	magnetic field from current in circuit 1 at position $\boldsymbol{r}$
$\Phi_{11,Int}$	self-flux of circuit inside the superconductor
$\Phi_{11,Ext}$	self-flux of circuit outside the superconductor
$E_k(\boldsymbol{r})$	kinetic energy density of charge super-carriers at position $\boldsymbol{r}$
$v_s(\boldsymbol{r})$	velocity of charge super-carriers at position $\boldsymbol{r}$
$E_m(\boldsymbol{r})$	magnetic energy density inside superconductor at position $\boldsymbol{r}$
L_k	kinetic inductance
L_{int}	internal inductance

Chapter 3

$K_{3DApproxPipp}$	approximated 3D Pippard kernel
K_{3DAP}	approximated 3D Pippard kernel with superfluous variables integrated out
K_{2DPipp}	2D Pippard kernel
K_{2DP}	2D Pippard kernel with superfluous variables integrated out
K_{1DPipp}	1D Pippard kernel
K_{1DP}	1D Pippard kernel with superfluous variables integrated out
W	infinite sheet width
$G(\boldsymbol{r}, \boldsymbol{r}')$	Green's function
K_{Pipp}	general Pippard kernel
R	radius of superconducting cylindrical wire
$I_0(\rho)$	modified Bessel's function of the first kind
$K_0(\rho)$	modified Bessel's function of the second kind
Ω	internal region of superconductor

$\partial\Omega$	boundary region of superconductor
$\hat{\boldsymbol{r}}$	unit vector pointing radially outward
FIE	Fredholm Integral Equation
I_{enc}	current enclosed
μ_s	Bohr magneton
g	g-factor of electron
$F_\theta(\rho)$	flux vector in $\hat{\theta}$ direction
s	total spin of impurity (eigenvalue of $\boldsymbol{S}_i^2$ is $s(s+1)$)
σ_2	density of spins on the surface of the superconductor
σ_3	density of spins in the bulk of the superconductor

Chapter 5

λ_{NL}	modified penetration depth for non-local superconductors

Appendix A

$K(x, x')$	kernel in Fredholm integral equation
ω_j	weighting factor for discretized kernel
$\delta(\boldsymbol{x} - \boldsymbol{x}')$	Dirac delta function

Glossary

Cooper pair The charge carriers of superconductivity, composed of a pair of electrons in a bound state. This pair is formed due to lattice interaction in BCS theory.

Diamagnetism Repulsion from or expulsion of an external magnetic field from an object.

Flux qubit A quantum bit which uses a SQUID as the physical architecture to encode information. The magnetic flux through the SQUID is used to control the state of the SQUID.

Green's function A function defined in relation to an operator such that the operator acting on the Green's function produces a Dirac delta distribution.

Josephson junction A junction between two superconductors that is small enough to allow tunneling of Cooper pairs from one superconductor to the other. The material in-between the superconductors can be an insulator, a normal metal, a constriction, or even vacuum.

London equations Phenomenological electrodynamic equations describing superconductivity, which relate current density in the superconductor to electromagnetic fields. These equations are local in the sense that the current density at a point is dependent only on the fields at that point.

Order parameter A function which distinguishes two phases of matter; it has a value of zero in the non-ordered phase and non-zero in the ordered phase. The order parameter for a superconductor is $\Psi(\boldsymbol{r})$, the pseudo-wavefunction for Cooper pairs, with the Cooper pair density given by $n_s = |\Psi(\boldsymbol{r})|^2$.

Pippard equation A generalization of the London equations, to take into account the position uncertainty or effective size of the Cooper pair wavefunction. This equation is non-local as the current density at a point is dependent on a volume around it, characterized by the Pippard coherence length.

ACKNOWLEDGEMENTS

Just as it takes a village to raise a child, a thesis does not spring from a solitary mind. Thanking every person who contributed to the substance of this document would far exceed the limits of this one page. Therefore I will paint my gratitude in broad brush-strokes and ask forgiveness from the many who are unnamed; your support is the strong force that binds this little nucleus.

I extend my heartfelt gratitude to:

My parents and sister, P. Senarath Yapa, Rohini Amarasingha and Upekha Senarath Yapa, for their endless love and encouragement. All my accomplishments are yours as well.

Dr. Rogério de Sousa for his insight and patience throughout the last two years.

Matthias Le Dall for being the perfect role model and mentor to a fledgling graduate student.

Tyler Makaro and Jean-Paul Barbosa for their hard work as undergraduate research assistants.

Trevor Lanting and D-Wave Systems, Inc. for the opportunity to work in the exciting field of quantum computing.

All the graduate students with whom I have formed deep friendships. Karaoke nights at Felicitas and every day spent with you all over the last two years have kept me counting my blessings.

The UVic Caving Club for being the greatest club on campus.

A book is not an isolated being: it is a relationship,
an axis of innumerable relationships.
Jorge Luis Borges

DEDICATION

To my family.

Figure 1: A superconducting squid

Chapter 1

Introduction

Superconducting QUantum Interference Devices (SQUIDs) are high sensitivity magnetometers, composed of a superconducting loop interrupted by thin, insulating barriers known as Josephson junctions, which are capable of detecting magnetic flux of the order 10^{-17} T [1]. Due to their extreme sensitivity, SQUIDs are used in wide variety of fields —in medicine to detect biomagnetism from neural activity and the heart [2]; in physics for tests of general relativity, and probing semiconductor and metal properties; in geology for natural resource prospecting and mineral characterization etc [1, 3]. In addition to these areas, they are also used in quantum computing applications as flux qubits, in particular by D-Wave Systems in their quantum annealing processor. However, the flux noise of the SQUIDs need to be reduced for them to become robust qubits. This is necessary as a reduction in flux noise would not only increase the speed and the accuracy of current calculations [4], but is required for building a reliable quantum computer, which must have an error correction threshold of 10^{-4} errors per quantum gate [5]. To achieve this limit, a $100\times$ reduction in flux noise power at low frequencies must be attained.

SQUIDs are affected by intrinsic flux noise due to the magnetic fluctuation of impurities at the device surfaces and interfaces [6, 7]. Recently, a flux-vector model based on local London electrodynamics was proposed [8, 9], predicting that the flux caused by a spin $\mathbf{s}_i$ located at position $\mathbf{R}_i$ produces a flux $\Phi_i = -\mathbf{F}_i \cdot \mathbf{s}_i$, where $\mathbf{F}_i$ is directly proportional to the magnetic field generated by the supercurrent at location $\mathbf{R}_i$. Such a model is therefore local, in the sense that the spin only "talks" to the supercurrent at $\mathbf{R}_i$. The hallmark of superconductivity is that the supercurrent is a very "quantum" object; it is carried by Cooper-pairs that are delocalized by a length scale ξ, the superconducting (SC) coherence length. This means that the Cooper-pairs are located within a region of the size of ξ. The local London electrodynamics

used in [8, 9] are only valid in the limit that ξ is small compared to the penetration depth λ, i.e. in the regime $\xi/\lambda \ll 1$. For many superconducting materials, this condition does not always hold true, see Table 1.1.

Superconductor	λ (nm)	ξ_0 (nm)
Al	50	1600
Pb	39	83
Sn	51	230
In	64	440
Nb	45	38
Cd	130	760

Table 1.1: Penetration depth λ, and coherence length ξ_0 for some pure, elemental superconductors (Values taken from Tables 2.1 and 2.2 of [10]). For impure superconductors, ξ is reduced according to $\frac{1}{\xi} = \frac{1}{\xi_0} + \frac{1}{l}$, where l is the mean free path for electrons in the normal state ($l < \infty$ due to effects such as electron-impurity scattering)

In this thesis, I use Pippard's theory for non-local electrodynamics in superconductors to calculate the supercurrent distribution in cylindrical superconducting wires with arbitrary radius. I use these results to calculate and discuss the impact of non-locality on flux noise and inductance of superconducting wires.
The thesis is structured in the following manner:

Chapter 2 provides the background to the results presented in this thesis, separated into two sections. The first is a phenomenological introduction to superconductivity and some historical detail. The second is an introduction to the rf-SQUID and its usage as a flux qubit.

Chapter 3 presents my original calculations of the non-local electrodynamics of superconductors. The results are calculated for two geometries: the infinite superconducting sheet and the infinite superconducting cylinder. The differences from the local solution are discussed, and various electrodynamic properties are presented.

Chapter 4 connects the non-local electrodynamic properties of the superconductor to the SQUID. The consequences for the flux noise are presented and discussed.

Chapter 5 presents my conclusions and an overview of my most important results.

Chapter 2

Background: Superconductivity and SQUIDs

An understanding of both the general principles of superconductivity and the structure of a SQUID are essential to understand the calculations herein. In this chapter, I present an overview of the physics of superconductivity and an outline of how to use SQUIDs as qubits.

2.1 History of Superconductivity

Superconductivity had a humble inception as an offshoot of a larger scientific effort - the race to liquefy the known gases. Developments in techniques of liquefaction of gases in the late 1800s led to most of the commonly known gases at the time being liquefied by scientists such as William Hampson, Carl von Linde and James Dewar [11]. Helium, only discovered on Earth in 1895, was liquefied after much effort by Dutch Physicist Kamerlingh Onnes in 1908. With liquid Helium at his disposal, Onnes was the only experimental physicist of his time with the capacity to reach temperatures as low as 1 K. Upon investigating the material properties of mercury at low temperatures, Onnes discovered superconductivity [12]; the phenomenon in which the resistivity of certain metals drops sharply to zero when cooled below a critical temperature, T_c. This temperature dependence is illustrated in Figure 2.1.

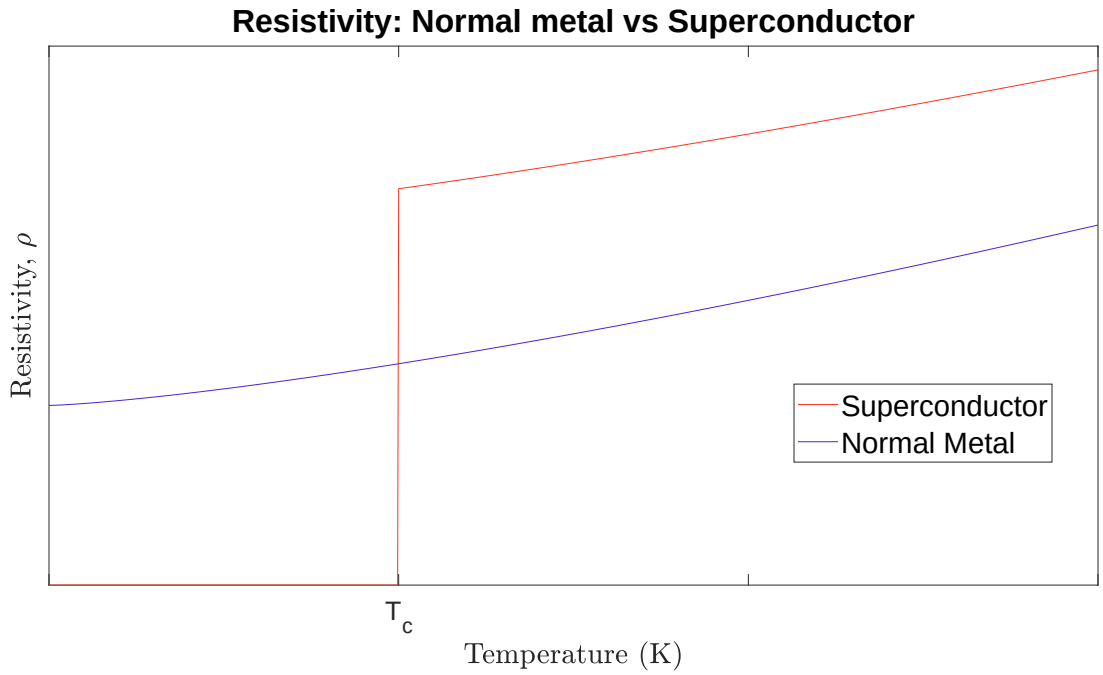

Figure 2.1: Temperature dependence of the resistivity of a normal metal versus a superconductor

Onnes confirmed this observation was not an aberration by finding similar behaviour in lead and tin, thus establishing the first hallmark of superconductivity: **perfect conductivity** below a material dependent temperature T_c. In other words, current could flow in a superconductor without energy being lost as heat.

The second hallmark of superconductivity was discovered by Meissner and Ochsenfeld in 1933 [13] - the expulsion of magnetic flux from within a superconductor as it is cooled from a normal state to the superconducting state. This phenomenon cannot be understood as originating from the perfect conductivity of the superconductor, as a perfect conductor would trap flux within when it passed into a perfect conducting state. This **perfect diamagnetism** was then established as a separate defining characteristic of the superconducting state, and is referred to as the *Meissner Effect*. Figure 2.2 illustrates this effect.

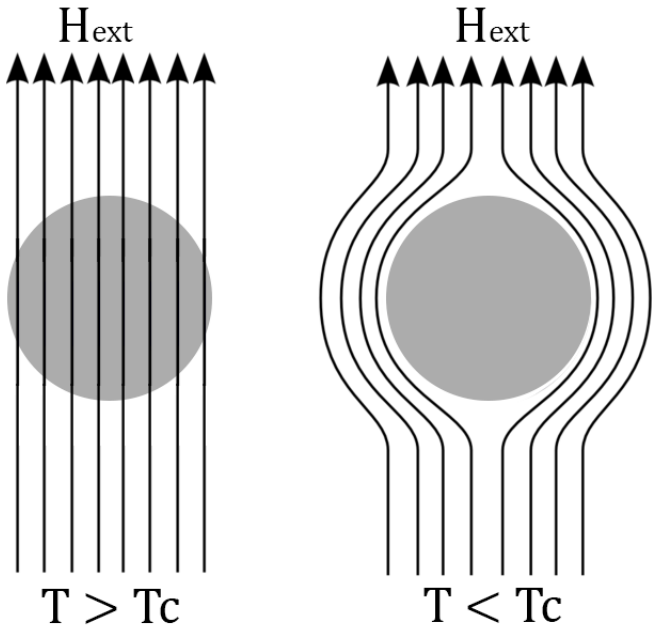

Figure 2.2: The Meissner Effect, or flux expulsion, in a superconductor when cooled below T_c

As these experimental observations of the superconducting state were being made, many attempts were made to build a coherent theory of superconductivity, but progress proved slow. The first phenomenological theory to describe superconductivity was posited by the brothers F. and H. London in 1935. This theory was put onto firmer theoretical foundations by the work of V.L. Ginzburg and L.D. Landau, through the eponymous *Ginzburg-Landau* (GL) theory in 1950 [14]. Their approach, using a free energy expansion in powers of a complex pseudo-wavefunction, has since been established as a versatile tool in many areas outside of superconductivity. Though both the GL theory and London theory were able to explain many aspects of superconductivity, they did not provide a mechanism at the microscopic scale. That description had to wait until 1957, when Bardeen, Cooper and Schrieffer (BCS) published their theory of superconductivity [15], which has stood as the best model for conventional superconductivity[1] since. BCS theory showed that superconductivity could be explained through the pairing of electrons to form a composite particle known as a Cooper pair. Thus the charge carriers of superconductivity have twice the charge of an ordinary electron.

[1]This model is insufficient to explain high temperature superconductivity found in certain metal oxides. In fact, a complete description of the origin of high temperature superconductivity has not been found to this day.

2.1.1 Ginzburg-Landau Theory

Ginzburg and Landau approached the problem of superconductivity through the general theory of second order phase transitions; the transition from the normal state to the superconducting state can be considered a transition from a disordered state to an ordered state, and can be distinguished through an order parameter. This order parameter is defined to take a value of zero in the disordered (normal metal) state and a non-zero value in the ordered (superconducting) state. For this purpose, they introduced a complex-valued pseudo-wavefunction $\Psi(\boldsymbol{r})$ within the superconductor. The density of charge super-carriers, n_s, functions as the order parameter for the superconducting state and is related to the pseudo-wavefunction through the relation,

$$n_s = |\Psi(\boldsymbol{r})|^2. \tag{2.1}$$

Ginzburg and Landau then wrote the free energy density of the superconductor in a magnetic field as a truncated Taylor series expansion in powers of $|\Psi(\boldsymbol{r})|^2$. This means that this theory is valid only near T_c, when $|\Psi(\boldsymbol{r})|^2$ (or super-carrier density) is small. To allow $\Psi(\boldsymbol{r})$ to vary in space, this expression had to include the gradient, and due to gauge invariance the gradient operator must be changed to $\boldsymbol{\nabla} \rightarrow \boldsymbol{\nabla} + \frac{e^*}{i\hbar}\boldsymbol{A}(\boldsymbol{r})$. And finally, as the magnetic field contains energy, the magnetic energy must be taken into account, which culminates in the GL expression for the free energy density in the superconducting state:

$$F_{SC} = F_N + \alpha|\Psi(\boldsymbol{r})|^2 + \frac{\beta}{2}|\Psi(\boldsymbol{r})|^4 + \frac{1}{2m^*}\big|(-i\hbar\boldsymbol{\nabla} - e^*\boldsymbol{A}(\boldsymbol{r}))\Psi(\boldsymbol{r})\big|^2 + \frac{1}{2\mu_0}\boldsymbol{B}(\boldsymbol{r})^2, \tag{2.2}$$

where F_N is the energy density of the normal metal state. The charge and mass in the above equation are specially marked as they correspond to the charge and mass of a Cooper pair. The Cooper pair charge is related to the electron charge through $e^* = 2e < 0$. Taking the functional derivative of this equation with respect to $\Psi(\boldsymbol{r})$ produces the differential equation,

$$\frac{1}{2m^*}\big(-i\hbar\boldsymbol{\nabla} - e^*\boldsymbol{A}(\boldsymbol{r})\big)^2\Psi(\boldsymbol{r}) + \beta|\Psi(\boldsymbol{r})|^2\Psi(\boldsymbol{r}) = -\alpha\Psi(\boldsymbol{r}). \tag{2.3}$$

This equation is reminiscent of the Schrödinger equation with the addition of a non-linear term. From this equation, we can derive the two defining characteristic length scales of superconductivity: λ, the penetration depth and ξ_{GL}, the GL coherence

length. In this section we will derive the ξ_{GL} and leave λ for discussion in the following section. Consider a 1-dimensional version of the above equation in the absence of any external fields:

$$-\frac{\hbar^2}{2m^*}\frac{\partial^2}{\partial x^2}\Psi(x)+\beta|\Psi(x)|^2\Psi(x)+\alpha\Psi(x)=0. \tag{2.4}$$

Let $f(x)=\frac{\Psi(x)}{\Psi_\infty}$, and $\Psi_\infty^2=-\frac{\alpha}{\beta}$. This produces an equation which has a coefficient with units of length squared in front of $\frac{\partial^2}{\partial x^2}\Psi(x)$,

$$-\frac{\hbar^2}{2m^*\alpha}\frac{\partial^2}{\partial x^2}f(x)-f(x)^3+f(x)=0. \tag{2.5}$$

We define this to be the Ginzburg-Landau characteristic coherence length ξ_{GL},

$$\xi_{GL}=\left(\frac{\hbar^2}{2m^*\alpha(T)}\right)^{\frac{1}{2}}. \tag{2.6}$$

ξ_{GL} can be thought of as the length scale characterizing the variation of the Cooper-pair density throughout the superconductor; the density of supercarriers is not allowed to change abruptly, but must vary smoothly over this length scale.

Taking the functional derivative of the free energy with respect to $\boldsymbol{A}(\boldsymbol{r})$ produces the equation for current density,

$$\boldsymbol{J}(\boldsymbol{r})=-\frac{ie^*\hbar}{2m^*}(\Psi^*\boldsymbol{\nabla}\Psi-\Psi\boldsymbol{\nabla}\Psi^*)-\frac{e^{*2}}{m^*}|\Psi(\boldsymbol{r})|^2\boldsymbol{A}(\boldsymbol{r}). \tag{2.7}$$

We will use this equation to develop the electrodynamics of superconductors in the 'local' London regime and the 'non-local' Pippard regime.

2.1.2 London's Local Electrodynamics

In the approximation of London local electrodynamics, we assume the pseudo-wavefunction does not have any spatial variation (i.e. the Cooper-pair density n_s is assumed constant throughout the superconductor), which reduces the current density equation to,

$$\boldsymbol{J}(\boldsymbol{r})=-\frac{e^{*2}}{m^*}n_s\boldsymbol{A}(\boldsymbol{r}). \tag{2.8}$$

Setting $\frac{m^*}{\mu_0 e^{*2} n_s}=\lambda^2$, the London penetration depth, we arrive at the London equation:

$$\boldsymbol{J}(\boldsymbol{r}) = -\frac{1}{\mu_0 \lambda^2}\boldsymbol{A}(\boldsymbol{r}). \tag{2.9}$$

It must be noted that this equation is only valid in the London gauge, which is defined as,

$$\boldsymbol{\nabla} \cdot \boldsymbol{A}(\boldsymbol{r}) = 0, \tag{2.10}$$

$$\boldsymbol{A}(\boldsymbol{r}) \cdot \hat{\boldsymbol{n}} = 0, \tag{2.11}$$

where $\hat{\boldsymbol{n}}$ is the unit vector that is perpendicular to the boundary of the superconductor. For a gauge other than London's we cannot assume $\boldsymbol{\nabla}\Psi = 0$ in Equation 2.7. We can use the two magnetostatic Maxwell equations,

$$\boldsymbol{\nabla} \cdot \boldsymbol{B}(\boldsymbol{r}) = 0, \tag{2.12}$$

$$\boldsymbol{\nabla} \times \boldsymbol{B}(\boldsymbol{r}) = \mu_0 \boldsymbol{J}(\boldsymbol{r}), \tag{2.13}$$

to derive some useful relations from the London equation. We substitute the 2^{nd} relation directly into the London equation to obtain,

$$\boldsymbol{\nabla} \times \boldsymbol{B}(\boldsymbol{r}) = -\frac{1}{\lambda^2}\boldsymbol{A}(\boldsymbol{r}). \tag{2.14}$$

Taking the cross product of both sides of this equation yields,

$$\boldsymbol{\nabla} \times \boldsymbol{\nabla} \times \boldsymbol{B}(\boldsymbol{r}) = -\frac{1}{\lambda^2}\boldsymbol{\nabla} \times \boldsymbol{A}(\boldsymbol{r}), \tag{2.15}$$

$$= -\frac{1}{\lambda^2}\boldsymbol{B}(\boldsymbol{r}). \tag{2.16}$$

And finally we use the vector calculus identity $\boldsymbol{\nabla} \times \boldsymbol{\nabla} \times \boldsymbol{F} = \boldsymbol{\nabla}(\boldsymbol{\nabla} \cdot \boldsymbol{F}) - \nabla^2 \boldsymbol{F}$ and Equation 2.12 to arrive at:

$$\nabla^2 \boldsymbol{B}(\boldsymbol{r}) = \frac{1}{\lambda^2}\boldsymbol{B}(\boldsymbol{r}). \tag{2.17}$$

This equation describes the Meissner Effect - the magnetic field is exponentially screened from the interior of the superconductor by a length scale λ. We can produce

similar relations for $\boldsymbol{J}(\boldsymbol{r})$ and $\boldsymbol{A}(\boldsymbol{r})$ using the Maxwell equations and working in the London gauge:

$$\nabla^2 \boldsymbol{J}(\boldsymbol{r}) = \frac{1}{\lambda^2}\boldsymbol{J}(\boldsymbol{r}), \tag{2.18}$$

$$\nabla^2 \boldsymbol{A}(\boldsymbol{r}) = \frac{1}{\lambda^2}\boldsymbol{A}(\boldsymbol{r}). \tag{2.19}$$

From the entirety of the London theory, we glean a couple of salient points:

1. London electrodynamics is inherently local. This can be seen from Equation 2.9, as it ties the current density at any given point to the vector potential at that point.

2. The current density is a maximum at the boundary of the superconductor, and is exponentially screened over the same length scale as the magnetic field. This is analogous to the skin effect in normal metals at high frequencies; therefore, the supercurrent exhibits a 'DC skin-effect'.

3. There will be no electric fields within the superconductor when the supercurrent density is static, i.e. $\boldsymbol{\nabla} \cdot \boldsymbol{J}(\boldsymbol{r}) = -\frac{\partial n_s}{\partial t} = 0$.

2.1.3 Analogy with Screening in Electrostatics

The London electrodynamics of a superconductor has a direct mathematical analogy in classical electrostatics. This analogy can provide a framework with which to derive qualitative solutions of difficult problems in superconductivity. We can observe this analogy through considering injecting a normal conductor with a charge density, ρ. As we know the electric field inside a conductor is zero in equilibrium, this charge density must redistribute itself within the conductor to screen out the electric field. In doing this, the charge will come to reside on the surface of the conductor. However, they are not distributed precisely on the surface, but instead occupy a region characterized by the screening length. The screening length for a Fermi gas at $T << T_F$ is given by Thomas-Fermi theory, while for a classical gas with $T >> T_F$, it is given by Debye-Hückel theory. The equations derived from those theories when taken in conjunction with the Maxwell equations become:

$$\begin{aligned} \nabla^2 \Phi_e &= -\frac{\rho_e}{\epsilon_0}, \\ \Phi_e &= -\lambda_e^2 \frac{\rho_e}{\epsilon_0}. \end{aligned} \tag{2.20}$$

The latter equation describes the screening of the electrostatic potential Φ_e over the screening length λ_a. We can immediately see that these are remarkably similar to the equations derived in the previous section:

$$\begin{aligned} \nabla^2 \boldsymbol{A} &= -\mu_0 \boldsymbol{J}, \\ \boldsymbol{A} &= -\lambda^2 \mu_0 \boldsymbol{J}. \end{aligned} \tag{2.21}$$

For most problems, $\boldsymbol{J}$ can be assumed to point along a single direction within a cross-section of the wire, $\boldsymbol{J} = J\hat{z}$. In this case we also have $\boldsymbol{A} = A\hat{z}$ in the London gauge, and the analogy with electrostatics becomes exact. The correspondence is given by,

$$\begin{aligned} \mu_0 \boldsymbol{J} &\leftrightarrow \frac{\rho_e}{\epsilon_0} \\ \boldsymbol{A} &\leftrightarrow \Phi_e \end{aligned} \tag{2.22}$$

In the next section, I will outline the non-local generalization to the London equation. I am not aware of an analogous "non-local screening" in electrostatics.

2.1.4 Pippard's Non-Local Electrodynamics

Brian Pippard's generalization of London electrodynamics was spurred by his experimental observations that could not be adequately explained by the local electrodynamic theory [16, 17]; the penetration depth of tin, λ, was found to increase with the addition of indium impurities, while other thermodynamics properties such as the critical temperature, T_c remained the relatively unchanged. As described in the previous section, in the London theory $\lambda = \left(\frac{m^*}{\mu_0 e^{*2} n_s}\right)^{\frac{1}{2}}$, which contains constants of the superconducting material as parameters - if T_c remains the same, then these must also be unchanged. Thus the London theory is unable to account for the change in the penetration depth with the addition of impurities. Pippard proposed a new phenomenological model to account for this fact by borrowing from the theory of the

anomalous skin-effect in the conductivity of (non-superconducting) metals [18]. In a normal metal, the relation between current density and electric field can be expressed using Ohm's Law:

$$\boldsymbol{J}(\boldsymbol{r}) = \sigma \boldsymbol{E}(\boldsymbol{r}). \tag{2.23}$$

However, this relation only holds when the mean free path of the metal, l, is small enough that the electric field can be considered to be constant over a region l. As the mean free path gets larger, the conduction electrons move through a region of space in which the electric field varies, and the linear relationship of Ohm's Law no longer holds. Thus the current density must take into account the non-local interactions of the conduction electrons with the electric field, which leads to the non-local generalization of Ohm's Law:

$$\boldsymbol{J}(\boldsymbol{r}) = -\frac{3\sigma}{4\pi l}\int \frac{(\boldsymbol{r}-\boldsymbol{r}')[(\boldsymbol{r}-\boldsymbol{r}')\cdot\boldsymbol{E}(\boldsymbol{r}')]}{(\boldsymbol{r}-\boldsymbol{r}')^4}\exp\left(-\frac{|\,\boldsymbol{r}-\boldsymbol{r}'\,|}{l}\right)d^3\boldsymbol{r}'. \tag{2.24}$$

As $l \to 0$, the integrand in the above equation approaches a Dirac delta times the electric field, and the local Ohm relation is recovered. Equation 2.24 above describes the anomalous skin-effect, a phenomenon observed in high purity metals at low temperatures, in which the high frequency oscillations of the current and electric field are localized along the surface of the metal within a "non-local" length scale that is different from the local one obtained with the usual Ohm's Law.

Using Equation 2.24 as inspiration, Pippard put forward a similar expression for the electrodynamics of superconductors, in which he proposed a new phenomenological parameter, the superconducting coherence length ξ_0, in place of the mean free path in metals,

$$\boldsymbol{J}(\boldsymbol{r}) = -\frac{3}{4\pi\mu_0\xi_0\lambda^2}\int \frac{(\boldsymbol{r}-\boldsymbol{r}')[(\boldsymbol{r}-\boldsymbol{r}')\cdot\boldsymbol{A}(\boldsymbol{r}')]}{(\boldsymbol{r}-\boldsymbol{r}')^4}\exp\left(-\frac{|\,\boldsymbol{r}-\boldsymbol{r}'\,|}{\xi}\right)d^3\boldsymbol{r}'. \tag{2.25}$$

In the above equation ξ_0 is a material parameter, while ξ is related to the purity of the material through the relation:

$$\frac{1}{\xi} = \frac{1}{l} + \frac{1}{\xi_0}. \tag{2.26}$$

Pippard arrived at this coherence length through an argument based on the Heisen-

berg uncertainty principle [19]. In a superconductor, only electrons that lie within $\sim k_B T_c$ of the Fermi energy can be in a superconducting state. The momentum range of these electrons is then $\Delta p \approx \frac{k_B T_c}{v_F}$, where v_F is the Fermi velocity. Thus we get that the range of position is given by,

$$\Delta x \geqslant \frac{\hbar}{\Delta p} \approx \frac{\hbar v_F}{k_B T_c}. \tag{2.27}$$

Pippard related this to ξ up to a numerical constant, a:

$$\xi_0 = a \frac{\hbar v_F}{k_B T_c}. \tag{2.28}$$

Using experimental data Pippard determined $a = 0.15$ [20] and this finding was later validated by the microscopic theory of BCS, which predicted $a = 0.18$ [15]. The Pippard kernel itself can be derived from BCS theory and is remarkably similar to the phenomenological kernel proposed by Pippard (See Section 3.10.3 of [19]).

The Pippard equation can be interpreted in the same manner as the non-local Ohm's Law - as the superconducting electrons (Cooper pairs) move through the superconductor, they move coherently through regions in which $\boldsymbol{A}(\boldsymbol{r})$ is not a constant, and thus the current density at any point within the superconductor is dependent on the vector potential in a volume surrounding that point, characterized by the length scale ξ.

NOTE: The Pippard coherence lengths, ξ and ξ_0, and the Ginzburg-Landau coherence length, ξ_{GL}, - though they share the same name and notation - are <u>not</u> the same quantity. ξ_0 describes the effective size of the Cooper pair and ξ_{GL} describes the characteristic length scale over which variations of the Cooper-pair density occur. The latter diverges as $T \to T_c$, while ξ_0 is temperature independent. However, at $T = 0$, the two quantities are the same and $\xi_{GL}(T = 0) = \xi_0$. When $0 < T < T_c$, $\xi_0 < \xi_{GL}(T)$. For an extended discussion on the differences between these coherence lengths, see Section 2.3.5 of [10].

The calculations performed in this thesis incorporate the Pippard coherence length, but not the Ginzburg-Landau coherence length into the superconductor electrodynamics. In a physical sense, this means that we consider that the number density of supercarriers is the same as in the London regime (it is constant throughout the superconductor), but the response of the current density is non-local. The results of this thesis are only valid for homogeneous superconductors; for an inhomogeneous superconducting structure such as a Josephson junction, a quantum version

of Ginzburg-Landau theory would have to be used instead of the Pippard equation [21].

2.2 The rf-SQUID as a Qubit

The foundation of all modern computation and digital communication is the bit - the most basic unit of information. In conceptual form it is simply a binary digit which take on one of two values, typically represented by 0 or 1, but it can be physically represented by any system that has two distinct states. This could be a punch card, which either has a hole punched in it or not; a switch, which is either on or off; a digital circuit, which outputs above or below a set voltage, or even a coin, which lands either heads or tails. Thus any system which is sufficiently malleable (can be manipulated from one state to the other), and is robust in its ability to remain in one state over the period of computation can be used as the basis for a computer.

In the same manner that the above *classical* objects have two states that can be manipulated, quantum mechanics provides many simple examples of two state systems: an electron can be spin up, $|\uparrow\rangle$, or spin down, $|\downarrow\rangle$; a photon can be in a right circular polarized state, or a left circular polarized state etc. However, the difference lies in the fact that in a classical system the states are always a single array of bits, while in a quantum system, the system can be put into a superposition of many different bit arrays. As a result, a logical operation acts on many superposition states at the same time. This "quantum parrallelism" can be exploited to provide a *quantum speedup* effect in certain types of computational problems.

One architecture for a quantum computer is to use a SQUID as a flux qubit. The world's first commercial quantum computer manufacturer, D-Wave systems in Burnaby, BC, uses this architecture in their quantum computer design. In the following sections we will outline the physical principles underlying a flux qubit.

2.2.1 Flux Quantization in a Superconducting Loop

Consider a superconducting loop containing some current density in an external field.

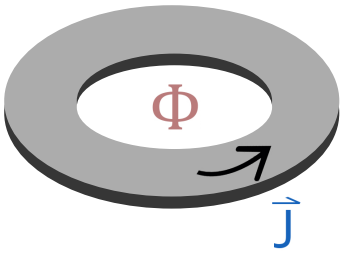

Figure 2.3: Superconducting Loop

The definition of the current density is,

$$\boldsymbol{J}(\boldsymbol{r}) = \frac{1}{2m^*}[\Psi^*(\boldsymbol{r})(-i\hbar\boldsymbol{\nabla} - e^*\boldsymbol{A}(\boldsymbol{r}))\Psi(\boldsymbol{r}) - \Psi(\boldsymbol{r})(-i\hbar\boldsymbol{\nabla} - e^*\boldsymbol{A}(\boldsymbol{r}))\Psi^*(\boldsymbol{r})]. \quad (2.29)$$

Assume that the $\Psi(\boldsymbol{r}) = |\Psi|e^{i\theta(\boldsymbol{r})}$. Then we get,

$$\boldsymbol{J}(\boldsymbol{r}) = \frac{n_s e^*}{m^*}(\hbar\boldsymbol{\nabla}\theta(\boldsymbol{r}) - e^*\boldsymbol{A}(\boldsymbol{r})). \quad (2.30)$$

Now consider a contour C deep within the superconductor, such that $\boldsymbol{J}(\boldsymbol{r}) = 0$ along that contour. If we perform a contour integral of the above equation, we obtain:

$$\oint_C \frac{\hbar}{e^*}\nabla\theta(\boldsymbol{r}) \cdot d\boldsymbol{l} = \oint_C \boldsymbol{A}(\boldsymbol{r}) \cdot d\boldsymbol{l}. \quad (2.31)$$

As the wavefunction must be single-valued, the change in θ after a loop around the superconductor must be $2\pi n$ where $n \in \mathbb{Z}$. We can use Stoke's theorem on the right side of the above equation to get, $\oint_C \boldsymbol{A}(\boldsymbol{r}) \cdot d\boldsymbol{l} = \int(\boldsymbol{\nabla} \times \boldsymbol{A}(\boldsymbol{r})) \cdot d\boldsymbol{S} = \int \boldsymbol{B}(\boldsymbol{r}) \cdot d\boldsymbol{S} = \Phi$. Thus we can rearrange to obtain,

$$\Phi = n\frac{2\pi\hbar}{e^*},\ n \in \mathbb{Z}. \quad (2.32)$$

We see that the flux enclosed by a superconducting loop is quantized in integer multiples of the flux quantum, Φ_0,

$$\Phi_0 = \frac{h}{e^*} = \frac{h}{2e}. \quad (2.33)$$

2.2.2 The Josephson Effect

The Josephson Effect describes the tunneling of Cooper pairs across a thin, insulating barrier sandwiched between two superconductors, as shown in the figure below. This thin barrier is known as a Josephson junction, and in general, the barrier could also be made of a normal metal or simply be a physical constriction of the superconductor.

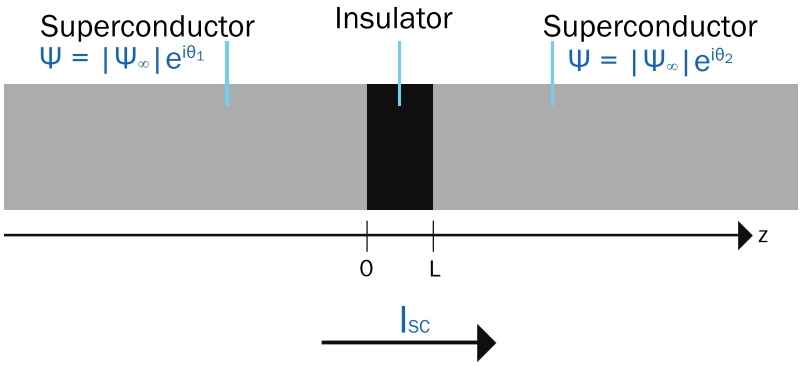

Figure 2.4: Josephson Effect

Josephson predicted in 1962 [22] that a current should flow across this barrier due to the phase difference between the wavefunctions of the two superconductors. We can derive this effect through Ginzburg-Landau theory.
Assume that the wavefunction inside the superconductors are given by,

$$\Psi(\boldsymbol{r}) = |\Psi|e^{i\theta}, \tag{2.34}$$

where θ is the superconducting phase. When the size of the insulator $L << \xi_{GL}$, the GL equation can be approximated by [19],

$$-\frac{\hbar^2}{2m^*}\nabla^2\Psi(\boldsymbol{r}) \approx 0. \tag{2.35}$$

This Laplace equation has a solution in 1D of the form,

$$\Psi(z) = a + bz. \tag{2.36}$$

When both the superconductors are in equilibrium, we must have $|\Psi(z = 0)| =$

$|\Psi(z = L)| = |\Psi_\infty|$, where $|\Psi_\infty|$ is $\sqrt{n_s}$ far from the insulating junction. Since the phase can differ, we can define the boundary conditions as,

$$\begin{aligned} \Psi(z = 0) &= |\Psi_\infty| e^{i\theta_1}, \\ \Psi(z = L) &= |\Psi_\infty| e^{i\theta_2}. \end{aligned} \tag{2.37}$$

Thus the solution to the Laplace equation is,

$$\Psi(z) = |\Psi_\infty| \left[\left(1 - \frac{z}{L} \right) e^{i\theta_1} + \frac{z}{L} e^{i\theta_2} \right]. \tag{2.38}$$

The supercurrent density in the absence of electromagnetic fields is given by,

$$\begin{aligned} \boldsymbol{J}(\boldsymbol{r}) &= \frac{e^* \hbar}{2m^* i} [\Psi(\boldsymbol{r})^* \boldsymbol{\nabla} \Psi(\boldsymbol{r}) - \Psi(\boldsymbol{r}) \boldsymbol{\nabla} \Psi(\boldsymbol{r})^*] \\ &= \frac{e^* \hbar}{m^*} \mathrm{Im}\big(\Psi(\mathrm{r})^* \boldsymbol{\nabla} \Psi(\mathrm{r})\big). \end{aligned} \tag{2.39}$$

Thus we get,

$$\begin{aligned} J_z &= \frac{e^* \hbar}{m^*} |\Psi_\infty|^2 \mathrm{Im}\left(\left[\left(1 - \frac{\mathrm{z}}{\mathrm{L}} \right) \exp^{-\mathrm{i}\theta_1} + \frac{\mathrm{z}}{\mathrm{L}} \exp^{-\mathrm{i}\theta_2} \right] \left[-\frac{1}{\mathrm{L}} \exp^{\mathrm{i}\theta_1} + \frac{1}{\mathrm{L}} \exp^{\mathrm{i}\theta_2} \right] \right) \\ &= \frac{e^* \hbar}{m^*} |\Psi_\infty|^2 \left(\frac{1}{L} (1 - \frac{z}{L}) \sin(\theta_2 - \theta_1) + \frac{z}{L^2} \sin(\theta_2 - \theta_1) \right) \\ &= \frac{e^* \hbar}{m^*} |\Psi_\infty|^2 \sin(\theta_2 - \theta_1). \end{aligned} \tag{2.40}$$

Therefore, the supercurrent is given by,

$$I_{SC} = I_C \sin(\theta_2 - \theta_1), \tag{2.41}$$

with $I_C = \frac{Ae^* \hbar n_s}{m^* L}$ in the above equation, where A is the cross-sectional area of the insulating junction. As it is only the phase difference that is observable, we can set $\theta = \theta_2 - \theta_1$.

The Josephson energy can be calculated by considering the dynamics of $\Psi(\boldsymbol{r}, t)$. Interpreting $\Psi(\boldsymbol{r}, t)$ as the wavefunction of the center of mass of the Cooper-pair, we can separate it into $\Psi(\boldsymbol{r}, t) = \Psi(\boldsymbol{r}, 0) e^{-i \frac{E_{CP} t}{\hbar}}$. As the energy of the Cooper-pairs are close to the Fermi energy, we can set $E_{CP} = 2\epsilon_F$. In equilibrium, the Cooper-pair

density does not depend on time, and since $n_S = |\Psi(\boldsymbol{r},t)|^2$, the time-dependence must be within the phase θ.

$$\begin{aligned} \theta(\boldsymbol{r},t) &= \theta(\boldsymbol{r},t) - \frac{2\epsilon_F t}{\hbar}, \\ \therefore \frac{\partial\theta(\boldsymbol{r},t)}{\partial t} &= -\frac{2\epsilon_F}{\hbar} = -\frac{2}{\hbar}[\epsilon_F(V=0) - eV(\boldsymbol{r})], \end{aligned} \tag{2.42}$$

where $V(\boldsymbol{r})$ is the voltage at the point $\boldsymbol{r}$ and $e < 0$ is the electron charge. At the junction, we get the relations,

$$\begin{aligned} \frac{\partial\theta_1(\boldsymbol{r},t)}{\partial t} &= -\frac{2}{\hbar}[\epsilon_F(V=0) - eV_1], \\ \frac{\partial\theta_2(\boldsymbol{r},t)}{\partial t} &= -\frac{2}{\hbar}[\epsilon_F(V=0) - eV_2]. \end{aligned} \tag{2.43}$$

As $\theta = \theta_2 - \theta_1$, and using the definition of the flux quantum from Equation 2.33, we get:

$$\frac{\partial\theta(\boldsymbol{r},t)}{\partial t} = -\frac{2\pi V}{\Phi_0}, \tag{2.44}$$

where $V = V_2 - V_1$. The energy stored in the Josephson junction is given by,

$$\begin{aligned} E_{JJ} &= \int I_{SC} V \, dt \\ &= -\int I_C \sin(\theta) \frac{\Phi_0}{2\pi} \frac{d\theta}{dt} \, dt \\ &= -\frac{\Phi_0 I_C}{2\pi} \int \sin(\theta) d\theta \\ &= \frac{\Phi_0 I_C}{2\pi} \cos(\theta) \\ &= E_J \cos(\theta). \end{aligned} \tag{2.45}$$

2.2.3 The rf-SQUID

The rf-SQUID is a superconducting loop interrupted by a single Josephson junction. Through the application of an external flux, an effective two state system is formed in the SQUID at low temperatures. This can be thought of as one state with a clockwise

rotating current and the other with an anti-clockwise current. This two state system forms the basis of its usage as a flux qubit [23].

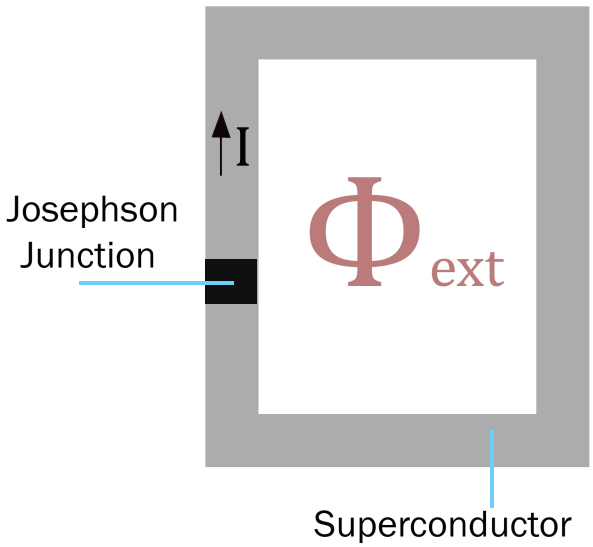

Figure 2.5: Schematic of rf-SQUID in an external flux

The energy of the SQUID can be split into the Josephson energy, magnetostatic energy and electrostatic energy.

$$\mathcal{H}_{SQUID} = -E_J \cos(\theta) + \frac{1}{2}LI^2 + \frac{1}{2}CV^2. \tag{2.46}$$

We can relate all three of these quantities to the flux enclosed by the SQUID. In the earlier section, we showed that the flux is quantized due to the change in the phase θ having to be to $2\pi n$ when we travel around the loop. We can now invert this relationship to write θ in terms of the flux:

$$\theta = 2\pi\Big(\frac{\Phi}{\Phi_0} + n\Big),\ n \in \mathbb{Z}. \tag{2.47}$$

The definition of inductance is $\Phi = \Phi_{ext} + LI$. And finally, $V = \frac{Q}{C} = \frac{e^* n_S}{C}$. The charge Q can be considered the conjugate operator of the flux with, $Q = i\hbar\frac{\partial}{\partial\Phi}$. Putting all this together:

$$\mathcal{H}_{SQUID} = -E_J \cos\left(2\pi\frac{\Phi}{\Phi_0}\right) + \frac{(\Phi - \Phi_{ext})^2}{2L} - \frac{\hbar^2}{2C}\frac{d^2}{d\Phi^2}. \tag{2.48}$$

Define $x = 2\pi\frac{\Phi}{\Phi_0}$, $x_{ext} = 2\pi\frac{\Phi_{ext}}{\Phi_0}$, $E_0 = \frac{1}{L}\left(\frac{\Phi_0}{2\pi}\right)^2$, $\beta_L = \frac{2\pi E_J L}{\Phi_0^2}$ and $m = \frac{C}{L}\left(\frac{\Phi_0}{2\pi}\right)^4$. Thus we get,

$$\frac{\mathcal{H}_{SQUID}}{E_0} = -\beta_L \cos(x) + \frac{1}{2}(x - x_{ext})^2 - \frac{\hbar^2}{2m}\frac{d^2}{dx^2} = V(x) - \frac{\hbar^2}{2m}\frac{d^2}{dx^2}. \tag{2.49}$$

When $\Phi_{ext} = \frac{\Phi_0}{2}$,

$$V(x) = \beta_L \cos(x - \pi) + \frac{1}{2}(x - \pi)^2. \tag{2.50}$$

For $x' = (x - \pi) << 1$, we can expand this as,

$$\begin{aligned} V(x') &= \beta_L\left[1 - \frac{x'^2}{2} + \frac{x'^4}{4!} + \mathcal{O}(x'^6)\right] + \frac{1}{2}x'^2, \\ &= \beta_L - \frac{1}{2}(\beta_L - 1)x'^2 + \frac{x'^4}{4!} + \mathcal{O}(x'^6). \end{aligned} \tag{2.51}$$

Thus for $\beta_L \geq 1$ the rf-SQUID forms a double well potential near $x \approx \pi$ ($\Phi = \frac{\Phi_0}{2}$). The state in each well can be thought of as the current in the SQUID circulating clockwise, $|\circlearrowright\rangle$, or counter-clockwise, $|\circlearrowleft\rangle$.

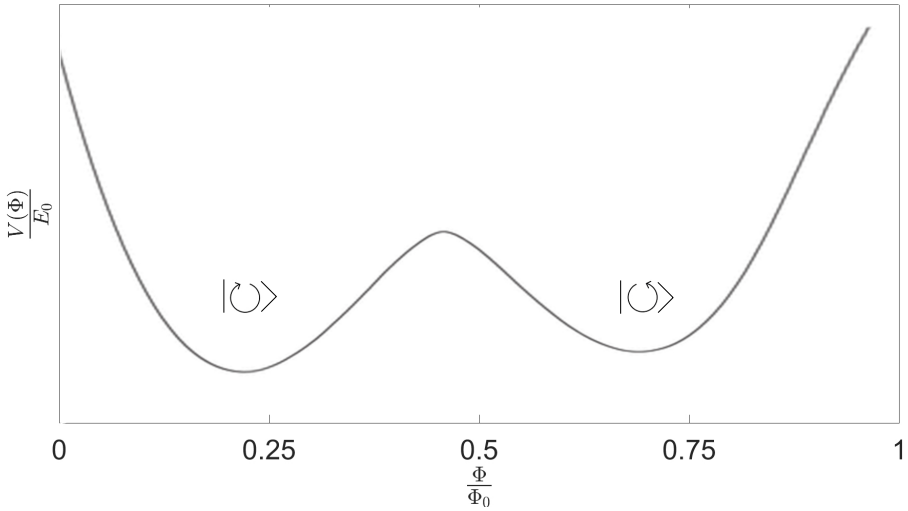

Figure 2.6: Double well potential in an rf-SQUID

The energy eigenstates of this system are,

$$|0\rangle = \frac{1}{\sqrt{2}}(|\circlearrowright\rangle + |\circlearrowleft\rangle), \tag{2.52}$$

$$|1\rangle = \frac{1}{\sqrt{2}}(|\circlearrowright\rangle - |\circlearrowleft\rangle). \tag{2.53}$$

These two states form the basis for quantum computation using the rf-SQUID.

2.3 Flux, Inductance and Magnetic Energy

Flux and inductance play a large part in the behaviour of a SQUID qubit, and thus must be rigorously defined. In this section, we will present an overview of how we define these quantities in a superconducting loop.

2.3.1 Flux

The flux produced by a loop C of infinitesimal cross-section is given by,

$$\Phi_C = \int_{S_C} \boldsymbol{B}(\boldsymbol{r}) \cdot \hat{\boldsymbol{n}}\, dA = \oint_C \boldsymbol{A}(\boldsymbol{r}) \cdot d\boldsymbol{l}. \tag{2.54}$$

This flux can be interpreted as the flux threading the internal area S_C bounded by the curve C, or as the flux picked up by an electron as it loops around the wire.

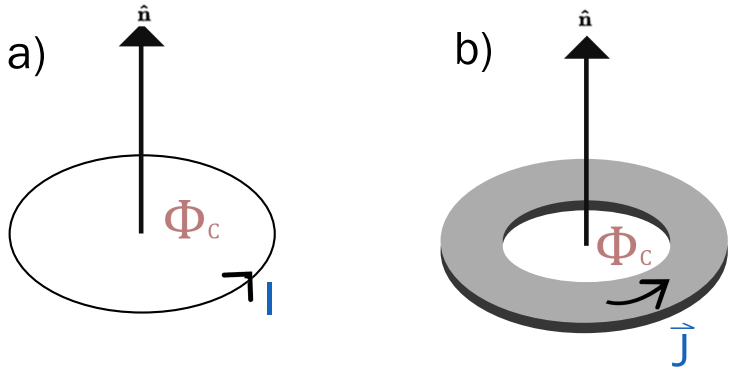

Figure 2.7: a) Infinitesimal wire loop with current I flowing through it. b) A loop formed by an infinite set of infinitesimal loops, with a current density $\boldsymbol{J}(\boldsymbol{r})$.

For a thick wire loop with a current density $\boldsymbol{J}(\boldsymbol{r})$ flowing through it, through

dividing the wire into infinitesimal loops and summing over the paths through, $d\boldsymbol{l} = \frac{\boldsymbol{J}(\boldsymbol{r})}{I}\, d^3r$, a weighting factor that represents the fraction of current flowing through each path:

$$\Phi_C = \frac{1}{I}\int \boldsymbol{A}(\boldsymbol{r}) \cdot \boldsymbol{J}(\boldsymbol{r})\, d^3\boldsymbol{r}. \tag{2.55}$$

As defined above, this flux is a general definition and serves as a means to compute the flux measured by a SQUID. We can also use this to define the *self-flux* of the circuit. The self-flux is defined as the flux produced by the current density of the wire itself:

$$\Phi_{11} = \frac{1}{I}\int \boldsymbol{A}_{J_1}(\boldsymbol{r}) \cdot \boldsymbol{J}_1(\boldsymbol{r})\, d^3\boldsymbol{r}, \tag{2.56}$$

where the '11' stands for the flux that circuit 1 applies on itself. The vector potential here is defined using the Green's function solution for the Maxwell relation $\nabla^2 \boldsymbol{A}_{J_1}(\boldsymbol{r}) = \mu_0 \boldsymbol{J}_1(\boldsymbol{r})$:

$$\boldsymbol{A}_{J_1}(\boldsymbol{r}) = \frac{\mu_0}{4\pi}\int \frac{\boldsymbol{J}_1(\boldsymbol{r})}{|\boldsymbol{r}-\boldsymbol{r}'|} d^3\boldsymbol{r}'. \tag{2.57}$$

The second Maxwell's equation for magnetostatics relates this magnetic field and the current density,

$$\boldsymbol{\nabla} \times \boldsymbol{B}_{J_1}(\boldsymbol{r}) = \mu_0 \boldsymbol{J}_1(\boldsymbol{r}). \tag{2.58}$$

We can insert this relation into equation into Equation 2.56 to get,

$$\Phi_{11} = \frac{1}{\mu_0 I}\int \boldsymbol{A}_{J_1}(\boldsymbol{r}) \cdot \boldsymbol{\nabla} \times \boldsymbol{B}_{J_1}(\boldsymbol{r})\, d^3\boldsymbol{r}, \tag{2.59}$$

Using the fact the magnetic field also obeys the relation is $\boldsymbol{B}_{J_1}(\boldsymbol{r}) = \boldsymbol{\nabla} \times \boldsymbol{A}_{J_1}(\boldsymbol{r})$, and the vector calculus identity $\boldsymbol{X} \cdot [\boldsymbol{\nabla} \times \boldsymbol{Y}] = \boldsymbol{Y} \cdot [\boldsymbol{\nabla} \times \boldsymbol{X}] - \boldsymbol{\nabla} \cdot [\boldsymbol{X} \times \boldsymbol{Y}]$, we can rewrite this as,

$$\begin{aligned}\Phi_{11} &= \frac{1}{\mu_0 I}\int \left[\boldsymbol{B}_{J_1}(\boldsymbol{r}) \cdot \left(\boldsymbol{\nabla} \times \boldsymbol{A}_{J_1}(\boldsymbol{r})\right) - \boldsymbol{\nabla} \cdot \left(\boldsymbol{A}_{J_1}(\boldsymbol{r}) \times \boldsymbol{B}_{J_1}(\boldsymbol{r})\right)\right] d^3\boldsymbol{r}, \\ &= \frac{1}{\mu_0 I}\int B^2_{J_1}(\boldsymbol{r})\, d^3\boldsymbol{r} - \frac{1}{\mu_0 I}\int \left(\boldsymbol{A}_{J_1}(\boldsymbol{r}) \times \boldsymbol{B}_{J_1}(\boldsymbol{r})\right) \cdot \hat{\boldsymbol{n}}\, d^2\boldsymbol{r}.\end{aligned} \tag{2.60}$$

In the above, we used the divergence theorem to convert the second integral into a

surface integral. As the surface of integration is arbitrary, we can consider the surface at infinity. We can see then that the terms in the bracket vanishes and thus the second term is zero. Thus the self-flux can also be written as,

$$\Phi_{11} = \frac{1}{\mu_0 I} \int B_{J_1}^2(\boldsymbol{r})\, d^3\boldsymbol{r}. \tag{2.61}$$

In the above, the integration must be performed over all space, and thus can be broken up into two parts corresponding to the integral inside the superconductor and outside the superconductor:

$$\begin{aligned} \Phi_{11} &= \frac{1}{\mu_0 I} \int_{Int} B_{J_1}^2(\boldsymbol{r})\, d^3 r + \frac{1}{\mu_0 I} \int_{Ext} B_{J_1}^2(\boldsymbol{r})\, d^3\boldsymbol{r}, \\ &= \Phi_{11,Int} + \Phi_{11,Ext}. \end{aligned} \tag{2.62}$$

2.3.2 Inductance

The kinetic energy density inside a superconductor is given by,

$$E_k(\boldsymbol{r}) = \frac{1}{2} m^* v_s^2(\boldsymbol{r}) n_s, \tag{2.63}$$

where $v_s(\boldsymbol{r})$ and n_s are the velocity and the number density of the supercurrent carriers, and m^* is the mass. As we know $J(\boldsymbol{r}) = n_s e^* v_s(\boldsymbol{r})$ and $\lambda^2 = \frac{m^*}{\mu_0 n_s e^{*2}}$, we can rewrite this as,

$$E_k = \frac{1}{2} \mu_0 \lambda^2 J^2(\boldsymbol{r}). \tag{2.64}$$

The magnetic energy density inside a superconductor is given by,

$$E_m(\boldsymbol{r}) = \frac{1}{2\mu_0} B^2(\boldsymbol{r}). \tag{2.65}$$

We can relate both these to inductance through the relation,

$$\frac{1}{2} L I^2 = \int_{SC} E(\boldsymbol{r})\, d^3\boldsymbol{r}, \tag{2.66}$$

where the integral is performed within the superconductor. Thus we obtain expressions for the kinetic inductance, L_k, and the internal magnetic inductance, L_{int}:

$$L_k = \int_{SC} \frac{\mu_0 \lambda^2 J^2(\boldsymbol{r})}{I^2}\, d^3\boldsymbol{r}, \tag{2.67}$$

$$L_{int} = \int_{SC} \frac{B^2(\boldsymbol{r})}{\mu_0 I^2}\, d^3\boldsymbol{r}. \tag{2.68}$$

We note that L_{int} is equivalent to the inductance which can be calculated using the Flux-Inductance Theorem, $\Phi = LI$, and the internal flux of Equation 2.62.

Chapter 3

Pippard Non-Local Electrodynamics

In this chapter we will present calculations of the current density and vector potential in two simple geometries, using an approximation to the Pippard Equation. For the entirety of this thesis, we will be working in the London gauge, defined by:

$$\boldsymbol{\nabla} \cdot \boldsymbol{A}(\boldsymbol{r}) = 0, \tag{3.1}$$

$$\boldsymbol{A}(\boldsymbol{r}) \cdot \hat{\boldsymbol{n}} = 0, \tag{3.2}$$

where the $\hat{\boldsymbol{n}}$ is the unit vector that is perpendicular to the surface of the superconductor.

3.1 Approximations and Analogues

The Pippard equation as originally developed has the form:

$$\boldsymbol{J}(\boldsymbol{r}) = -\frac{3}{4\pi\mu_0\xi\lambda^2}\int \frac{(\boldsymbol{r}-\boldsymbol{r}')[(\boldsymbol{r}-\boldsymbol{r}')\cdot\boldsymbol{A}(\boldsymbol{r}')]}{(\boldsymbol{r}-\boldsymbol{r}')^4}\exp\left(-\frac{|\,\boldsymbol{r}-\boldsymbol{r}'\,|}{\xi}\right)d^3\boldsymbol{r}'. \tag{3.3}$$

In the physical geometries we explore within this thesis, we always constrain $\boldsymbol{A}(\boldsymbol{r})$ and $\boldsymbol{J}(\boldsymbol{r})$ to only have one non-zero component. Namely,

$$\boldsymbol{A}(\boldsymbol{r}) = A(\boldsymbol{r})\hat{\boldsymbol{z}}, \tag{3.4}$$

$$\boldsymbol{J}(\boldsymbol{r}) = J(\boldsymbol{r})\hat{\boldsymbol{z}}, \tag{3.5}$$

where $\boldsymbol{r} = (x, y) = (\rho\cos(\theta), \rho\sin(\theta))$. The spatial extent of our geometry in the z-direction is also taken to extend from $-\infty$ to ∞. With these constraints, we can simplify the above Pippard equation to a scalar equation:

$$J(\boldsymbol{r}) = \frac{-3}{4\pi\mu_0\xi\lambda^2}\int\int_{-\infty}^{\infty}\frac{(z-z')^2 A(\boldsymbol{r})}{[(z-z')^2+|\boldsymbol{r}-\boldsymbol{r}'|^2]^2}\exp\left[-\frac{\sqrt{(z-z')^2+|\boldsymbol{r}-\boldsymbol{r}'|^2}}{\xi}\right]dz'd^2\boldsymbol{r}. \tag{3.6}$$

Although we can theoretically integrate the z-dependence out of the above equation, this turns out be analytically intractable and has to be done numerically. However, in many superconductor geometries, a full calculation of the 3D integral either has negligible contributions along one spatial dimension, or is numerically impractical. Due to these reasons, it is useful to derive lower dimensional Pippard equation analogues and approximations to the 3D Pippard equation respectively.

3.1.1 Approximation to the 3D Pippard Kernel

We will first look at deriving an approximation for the integral over z in the above equation. The integral we must then do is,

$$f(\boldsymbol{r}) = \int_{-\infty}^{\infty}\frac{(z-z')^2}{[(z-z')^2+|\boldsymbol{r}-\boldsymbol{r}'|^2]^2}\exp\left[-\frac{\sqrt{(z-z')^2+|\boldsymbol{r}-\boldsymbol{r}'|^2}}{\xi}\right]dz'. \tag{3.7}$$

Since our final result will have no z-dependence, our choice of z is arbitrary, and we can set $z = 0$. We can also make this a dimensionless integration by absorbing the ξ into our variables. That is $\frac{z'}{\xi} \to \upsilon$ and $\frac{|\boldsymbol{r}-\boldsymbol{r}'|}{\xi} \to \tau$.

$$f(\boldsymbol{r}) = \frac{1}{\xi}\int_{-\infty}^{\infty}\frac{\upsilon^2}{[\upsilon^2+\tau^2]^2}\exp\left[-\sqrt{\upsilon^2+\tau^2}\right]d\upsilon. \tag{3.8}$$

By using Mathematica to perform the numerical integration, we obtained a baseline to compare expressions which approximate the integral.

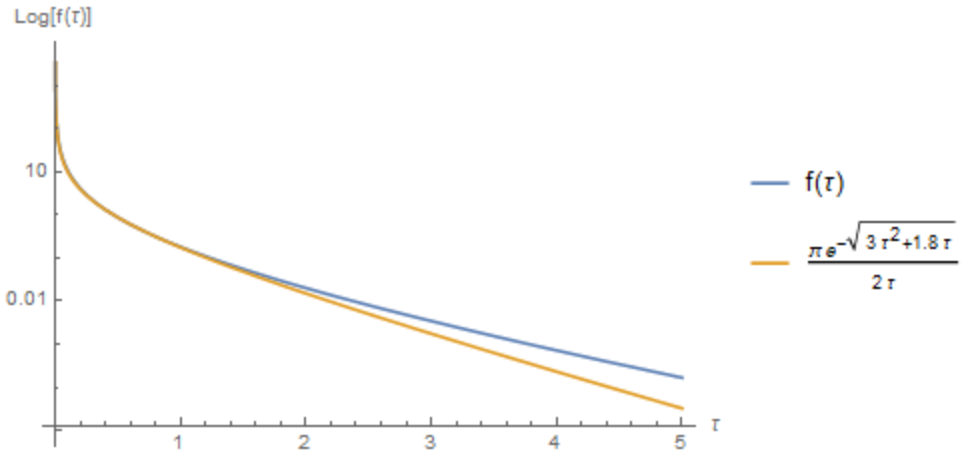

Figure 3.1: Numerical Integration vs Approximated Function

The function $f(\tau)$ is the numerically integrated function and $\pi\frac{\exp\left[-\sqrt{3\tau^2+1.8\tau}\right]}{2\tau}$ is the approximating function. By inspection, we see that the functions are very similar over the plotted domain, and thus we can substitute it into the Pippard equation. For a cylindrical wire we get,

$$\begin{aligned} J(\rho) &= -\frac{3}{8\mu_0\xi\lambda^2}\int_0^R\int_0^{2\pi} A(\rho')\frac{\exp\left[-\sqrt{1.8\frac{|\boldsymbol{r}-\boldsymbol{r}'|}{\xi}+3\frac{|\boldsymbol{r}-\boldsymbol{r}'|^2}{\xi^2}}\right]}{|\,\boldsymbol{r}-\boldsymbol{r}'\,|}\rho' d\theta' d\rho' \\ &= \int_0^R\left[\int_0^{2\pi} K_{3DApproxPipp}(\theta,\theta',\rho,\rho')d\theta'\right]A(\rho')\rho' d\rho' \\ &= \int_0^R K_{3DAP}(\rho,\rho')A(\rho')\rho' d\rho'. \end{aligned} \tag{3.9}$$

The second line in the above equation has an integration over θ' that must be performed numerically to obtain the final kernel $K_{3DAP}(\rho,\rho')$. We will refer to this kernel as the 3D approximation to the Pippard kernel.

3.1.2 2D and 1D Analogues to the Pippard Kernel

Having obtained an approximation to the full 3D Pippard kernel, we will now derive an exact Pippard kernel in 2D and 1D. The Pippard equation must always satisfy the condition that it must reduce to the London relation as $\xi \to 0$. If we set the vector potential to only have radial dependence, $\boldsymbol{A}(\boldsymbol{r}') = \boldsymbol{A}(r')$, within the integral in the

original Pippard equation[1], and perform the trivial angular integrations in spherical coordinates, the integral will take the form of the exponential representation of the Dirac delta function.

$$\begin{aligned} \boldsymbol{J}(\boldsymbol{r}) &= -\frac{1}{\mu_0\lambda^2}\int \boldsymbol{A}(r')\frac{\exp\left(-\frac{|r-r'|}{\xi}\right)}{2\xi}dr' \\ &\underset{\xi\to 0}{=} -\frac{\boldsymbol{A}(r)}{\mu_0\lambda^2}. \end{aligned} \tag{3.10}$$

Thus we see that the London equation is a limiting case of the Pippard equation. Using this as our guiding principle, we can develop 2D and 1D analogues to the Pippard equation.

$$\begin{aligned} J(\rho) &= -\frac{1}{2\pi\mu_0\xi\lambda^2}\int A(\rho')\frac{\exp\left(-\frac{|\boldsymbol{r}-\boldsymbol{r}'|}{\xi}\right)}{\mid \boldsymbol{r}-\boldsymbol{r}' \mid}d^2\boldsymbol{r}' \\ &= \int_0^R \left[\int_0^{2\pi} K_{2DPipp}(\theta,\theta',\rho,\rho')d\theta'\right]A(\rho')\rho' d\rho' \\ &= \int_0^R K_{2DP}(\rho,\rho')A(\rho')\rho' d\rho'. \end{aligned} \tag{3.11}$$

and in 1D, we will revert to simple Cartesian coordinates, where the extent of the superconductor is from $x \in [-\frac{w}{2}, \frac{w}{2}]$:

$$\begin{aligned} J(x) &= -\frac{1}{2\mu_0\xi\lambda^2}\int_{-\frac{w}{2}}^{\frac{w}{2}} A(x')\exp\big(-\frac{\mid x-x' \mid}{\xi}\big)dx' \\ &= \int_{-\frac{w}{2}}^{\frac{w}{2}} K_{1DP}(x,x')A(x')dx'. \end{aligned} \tag{3.12}$$

3.2 Superconducting Infinite Sheet

The superconducting infinite sheet serves both as good testing ground for the ideas that we will develop further in this chapter and as a model for a ground plane in

[1] which is valid as the vector potential will not have any angular dependence as $\xi \to 0$

superconducting devices.

3.2.1 Geometry

The infinite sheet is taken to have a width, w, in the $\hat{y}$ direction while extending infinitely in the $\hat{x}$ and $\hat{z}$ directions. A current I is being transported along the wire in the $\hat{\boldsymbol{z}}$ direction per unit length in the $\hat{\boldsymbol{x}}$ direction.

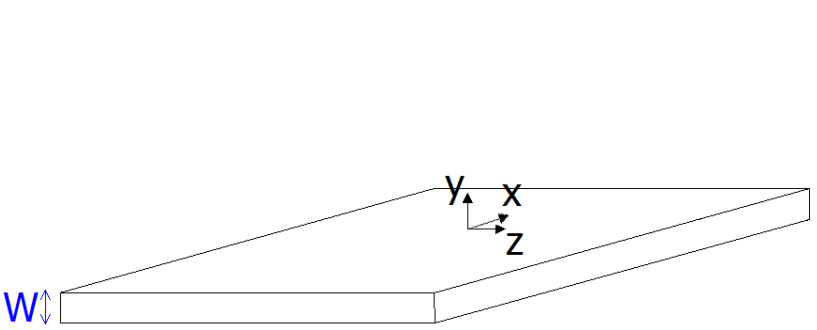

(a) 3D view

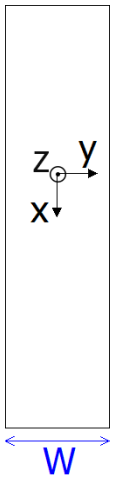

(b) Edge-on view

Figure 3.2: Geometry of the Superconducting Infinite Sheet

The penetration depth for this superconductor was chosen to be $\lambda = 70$ nm, and two values of the width were chosen: $W = 500$ nm and $W = 2000$ nm. As this geometry is infinite in both the $\hat{\boldsymbol{x}}$ and $\hat{\boldsymbol{z}}$ directions, by translation invariance there cannot be any variation of either the current density or the vector potential in those directions. That is, $\boldsymbol{J}(\boldsymbol{r}) = \boldsymbol{J}(y)$ and $\boldsymbol{A}(\boldsymbol{r}) = \boldsymbol{A}(y)$. This effectively makes the problem a 1-dimensional calculation.

We remark that the infinite sheet is a useful approximation for the shielding plane used in superconducting devices (See Chapter 3.09 of [24]).

3.2.2 Local London Electrodynamics

The current density and the vector potential are taken to be parallel to the z-axis.

$$\boldsymbol{J}(\boldsymbol{r}) = J(y)\hat{\boldsymbol{z}}. \tag{3.13}$$

$$\boldsymbol{A}(\boldsymbol{r}) = A(y)\hat{\boldsymbol{z}}. \tag{3.14}$$

Note that the last equation satisfies the London gauge. The London equation relates these two quantities:

$$\boldsymbol{J}(\boldsymbol{r}) = -\frac{1}{\lambda^2\mu_0}\boldsymbol{A}(\boldsymbol{r}). \tag{3.15}$$

Inside the superconductor, the current density satisfies:

$$\boldsymbol{\nabla}^2\boldsymbol{J}(\boldsymbol{r}) = \frac{\boldsymbol{J}(\boldsymbol{r})}{\lambda^2}. \tag{3.16}$$

As this is a 1-dimensional problem, $\boldsymbol{\nabla}^2 = \frac{\partial^2}{\partial y^2}$. Collating the above information, we have the simple differential equation,

$$\frac{\partial^2}{\partial y^2}J(y) = \frac{J(y)}{\lambda^2}. \tag{3.17}$$

Using the fact that the solution must be even due to reflection symmetry across the y-axis, the solution is:

$$J(y) = J_0\cosh\Big(\frac{y}{\lambda}\Big). \tag{3.18}$$

We can normalize this across the y-axis to find out J_0.

$$\int_{-\frac{w}{2}}^{\frac{w}{2}} J_0\cosh\Big(\frac{y}{\lambda}\Big)dy = \frac{I}{L} \tag{3.19}$$

$$\implies J_0 = \frac{I}{2\lambda\sinh\big(\frac{W}{2\lambda}\big)L}, \tag{3.20}$$

where I is the total current and L is the length of the sheet in the x-direction. Thus the normalized current density is,

$$J(y) = \frac{I\cosh\big(\frac{y}{\lambda}\big)}{2\lambda\sinh\big(\frac{W}{2\lambda}\big)L}, \quad -\frac{w}{2} \le y \le \frac{w}{2}, \tag{3.21}$$

and zero otherwise. Using the London equation, the vector potential inside the superconductor is given by,

$$A(y) = -\frac{\mu_0 I\lambda}{2L\sinh\big(\frac{W}{2\lambda}\big)}\cosh\Big(\frac{y}{\lambda}\Big), \quad -\frac{w}{2} \le y \le \frac{w}{2}. \tag{3.22}$$

3.2.3 Non-Local Electrodynamics

To solve for the vector potential and current density in a non-local scenario, we first consider the Maxwell relation,

$$\boldsymbol{\nabla} \times \boldsymbol{B}(\boldsymbol{r}) = \mu_0 \boldsymbol{J}(\boldsymbol{r}). \tag{3.23}$$

We can use $\boldsymbol{B}(\boldsymbol{r}) = \boldsymbol{\nabla} \times \boldsymbol{A}(\boldsymbol{r})$ and the vector calculus identity $\boldsymbol{\nabla} \times \boldsymbol{\nabla} \times \boldsymbol{A}(\boldsymbol{r}) = \boldsymbol{\nabla}(\boldsymbol{\nabla} \cdot \boldsymbol{A}(\boldsymbol{r})) - \nabla^2 \boldsymbol{A}(\boldsymbol{r})$ to simplify this equation. As we are working in the London gauge, the first term disappears and we are left with,

$$\nabla^2 \boldsymbol{A}(\boldsymbol{r}) = -\mu_0 \boldsymbol{J}(\boldsymbol{r}). \tag{3.24}$$

As we took $\boldsymbol{A}(\boldsymbol{r}) = A(y)\hat{\boldsymbol{z}}$ and $\nabla^2 = \frac{\partial^2}{\partial y^2}$ in 1D, we arrive at a Poisson equation with Dirichlet boundary conditions:

$$\frac{\partial^2}{\partial y^2} A(y) = -\mu_0 J(y), \tag{3.25}$$

$$A\big(y = -\frac{w}{2}\big) = A\big(y = \frac{w}{2}\big) = A_0. \tag{3.26}$$

In Appendix A, we developed the tools to solve this problem, thus we can simply write down the solution:

$$A(y) = h(y) + \mu_0 \int_{-\frac{w}{2}}^{\frac{w}{2}} G(y, y') J(y') dy'. \tag{3.27}$$

Where $h(y) = \frac{\partial G(y,y')}{\partial y'}\Big|_{-\frac{w}{2}} A_0 - \frac{\partial G(y,y')}{\partial y'}\Big|_{\frac{w}{2}} A_0$. The Green's function for the operator $\nabla^2 = \frac{\partial^2}{\partial y^2}$ with the above boundary conditions was calculated to be,

$$G(y, y') = \begin{cases} \frac{1}{2}(y - y' + yy' - 1) & y' \leqslant y, \\ \frac{1}{2}(y + 1)(y' - 1) & y \leqslant y'. \end{cases}$$

We obtain a Fredholm integral equation by substituting the Pippard equation, which has the form:

$$J(y') = \int_{-\frac{w}{2}}^{\frac{w}{2}} K_{Pipp}(y', y'') A(y'') dy''. \tag{3.28}$$

$$\implies A(y) = h(y) + \mu_0 \int_{-\frac{w}{2}}^{\frac{w}{2}} \int_{-\frac{w}{2}}^{\frac{w}{2}} G(y, y') K_{Pipp}(y', y'') A(y') dy' dy'. \tag{3.29}$$

We solve the above Fredholm integral equation using the tools developed in Appendix A. As described in Section 3.1, we have three Pippard kernels at our disposal: the 1D Pippard kernel K_{1DP}, the 2D Pippard kernel K_{2DP}, and the 3D approximated Pippard kernel K_{3DAP} (with K_{2DP} and K_{3DAP} converted to Cartesian coordinates). To illustrate the differences between these three kernels, we showcase the results using all three below. Once $A(y)$ was calculated, $J(y)$ was calculated using the respective Pippard equation.

3.2.4 Results

As Pippard electrodynamics must converge to London in the limit $\xi \to 0$, we first show results for $A(y)$ for an infinite sheet with width $W = 500$ nm and $W = 2000$ nm, with $\xi = 10$ nm. (For lower values of ξ, a finer mesh would have had to be used for the numerical calculations.)

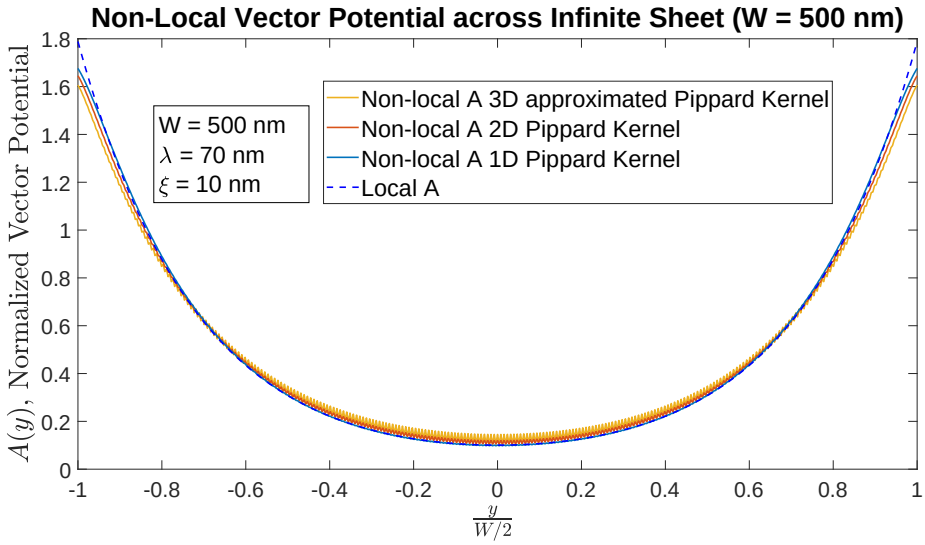

Figure 3.3: Normalized vector potential for infinite sheet with $W = 500$ nm and $\xi = 10$ nm

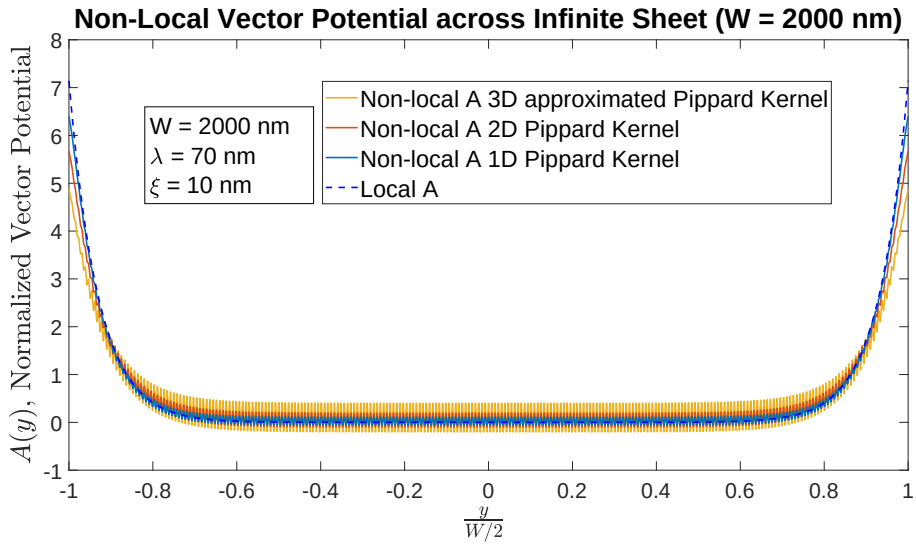

Figure 3.4: Normalized vector potential for infinite sheet with $W = 2000$ nm and $\xi = 10$ nm

From the above plots, it can be seen that all 3 kernels closely follow the local result. However, we can see that the 3D approximated Pippard kernel is computationally costly and thus has numerical oscillations which affect the accuracy of the results. The numerical oscillations are seen to increase as the ratio $\frac{\xi}{W}$ becomes smaller. This is not a significant concern however, as the results of interest are when ξ is large compared to the geometry - the small ξ values are shown to verify that the calculations are working as expected.

If we calculate $J(y)$ from the above results, we obtain the following plots:

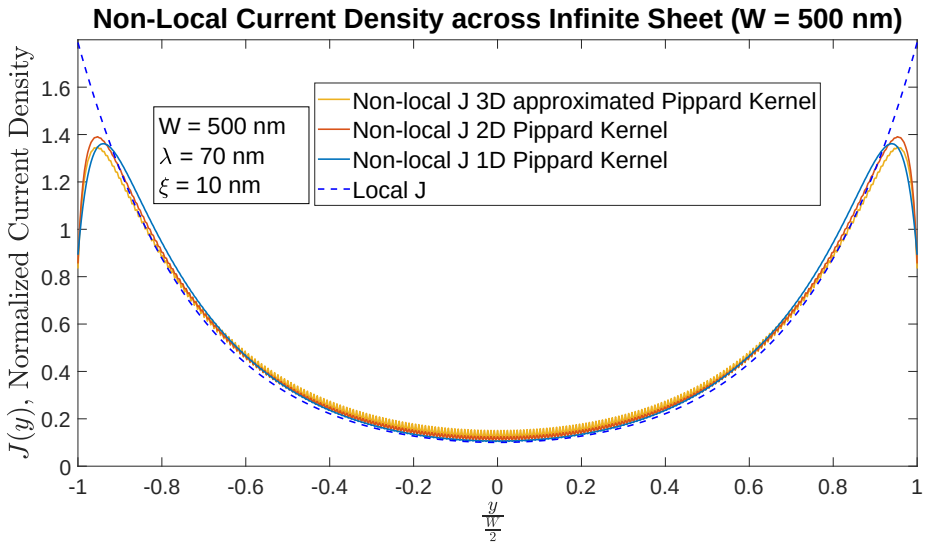

Figure 3.5: Normalized current density for infinite sheet with $W = 500$ nm and $\xi = 10$ nm

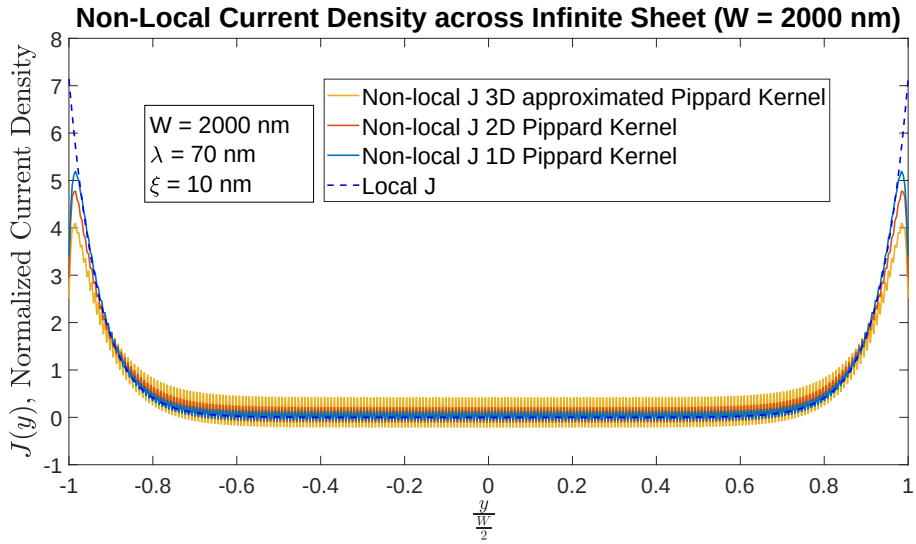

Figure 3.6: Normalized current density for infinite sheet with $W = 2000$ nm and $\xi = 10$ nm

The main features of the above plots are that while they all are compatible with the local London distribution, the peak of the current is off the edge of the superconductor. Due to the numerical oscillations, it's difficult to put any significance into the

observation that 1D Pippard kernel produces the highest peaked $J(y)$ for $W = 2000$ nm, then the 2D Pippard and lastly the 3D Approximated Pippard.

To make any conclusions in that regard, we must obtain results that are more numerically stable. We can achieve that by looking at large values of ξ. The below plots show results for $A(y)$ for an infinite sheet with widths $W = 500$ nm and $W = 2000$ nm, and with $\xi = 200$ nm and $\xi = 1000$ nm.

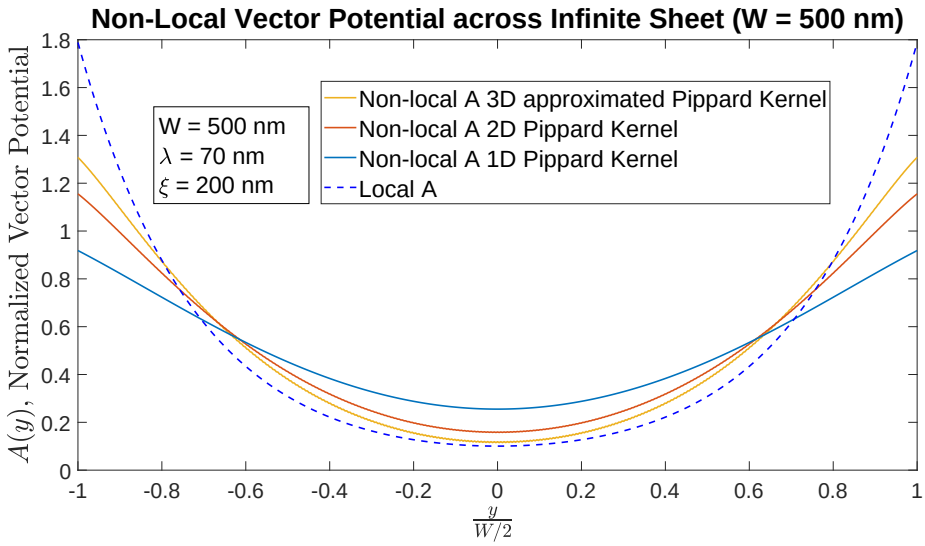

Figure 3.7: Normalized vector potential for infinite sheet with $W = 500$ nm and $\xi = 200$ nm

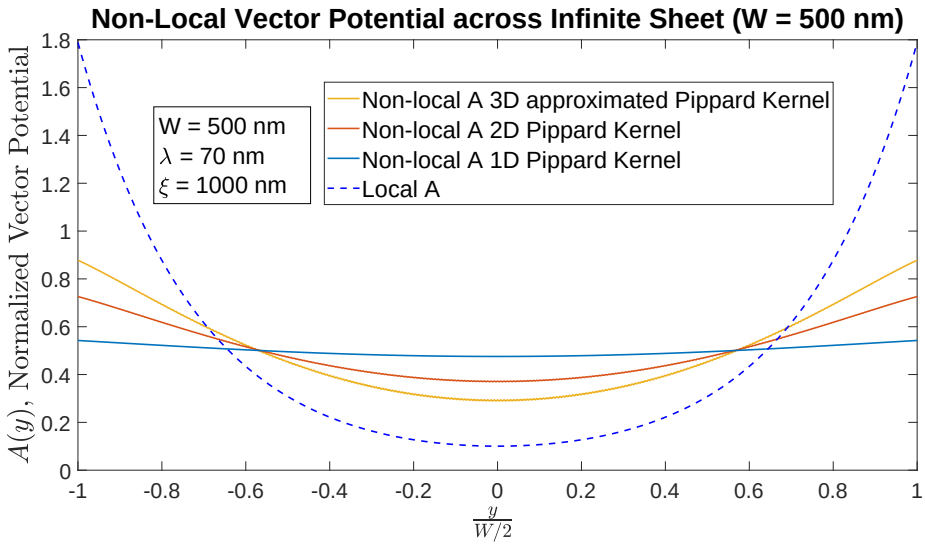

Figure 3.8: Normalized vector potential for infinite sheet with $W = 500$ nm and $\xi = 1000$ nm

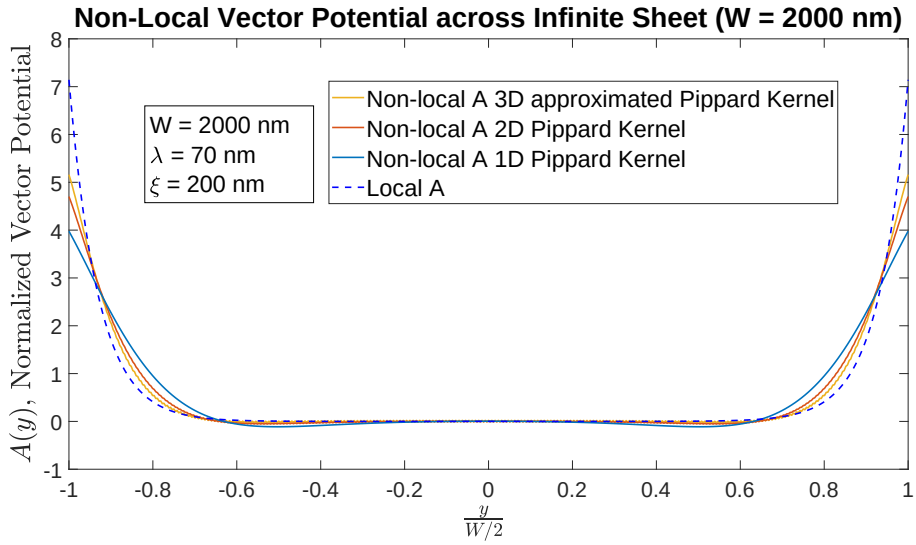

Figure 3.9: Normalized vector potential for infinite sheet with $W = 2000$ nm and $\xi = 200$ nm

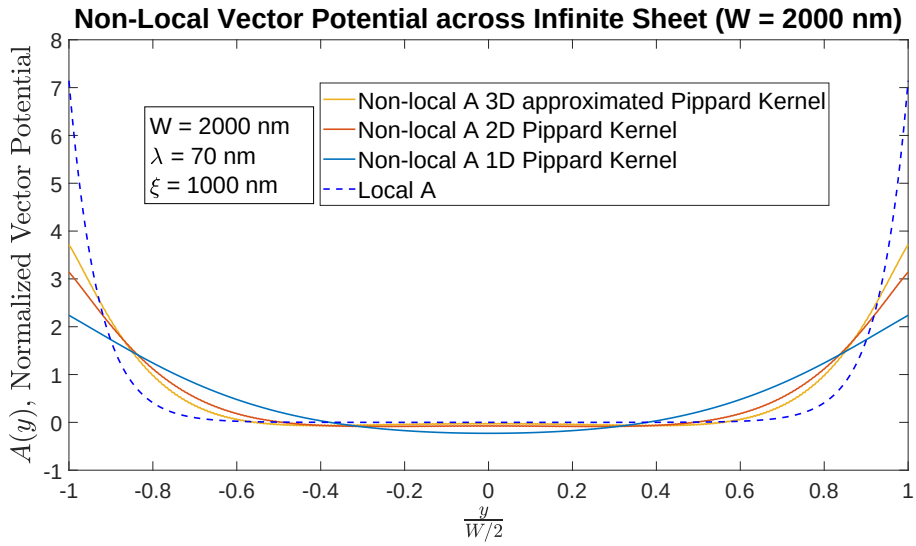

Figure 3.10: Normalized vector potential for infinite sheet with $W = 2000$ nm and $\xi = 1000$ nm

These figures show that $A(y)$ is highest for the 3D Approximated Pippard Kernel, then 2D and lastly 1D for both widths. In the $W = 500$ nm case, the vector potentials for all the non-local cases deviate significantly from the local case and show a flattened distribution. The current density plots show similar features:

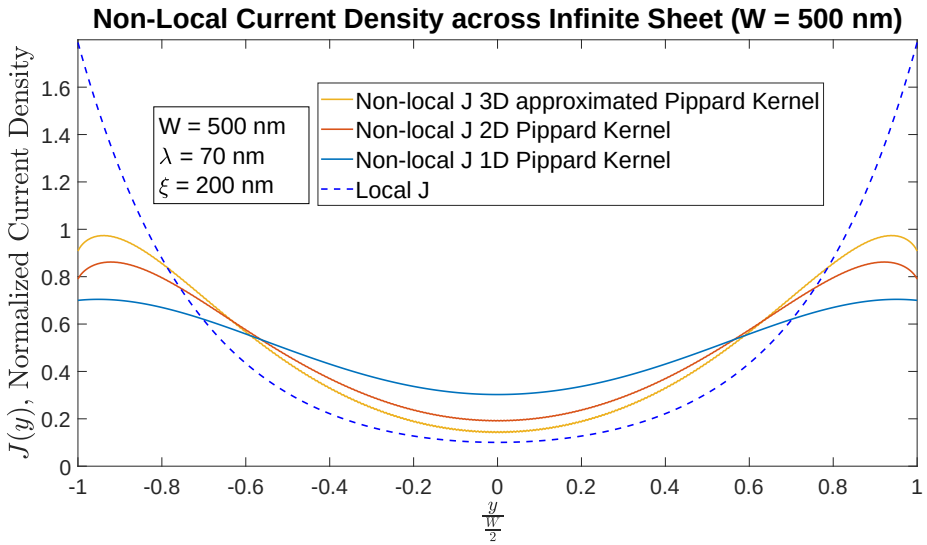

Figure 3.11: Normalized current density for infinite sheet with $W = 500$ nm and $\xi = 200$ nm

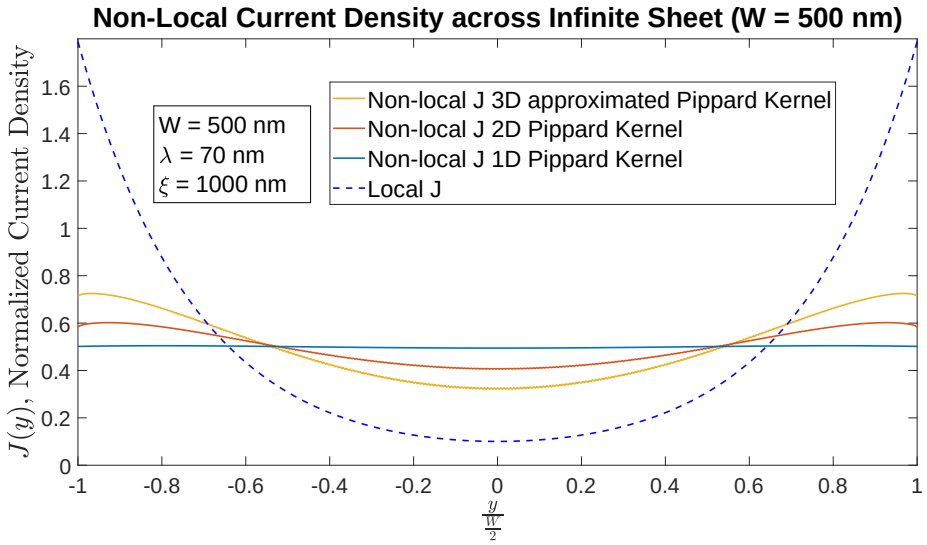

Figure 3.12: Normalized current density for infinite sheet with $W = 500$ nm and $\xi = 1000$ nm

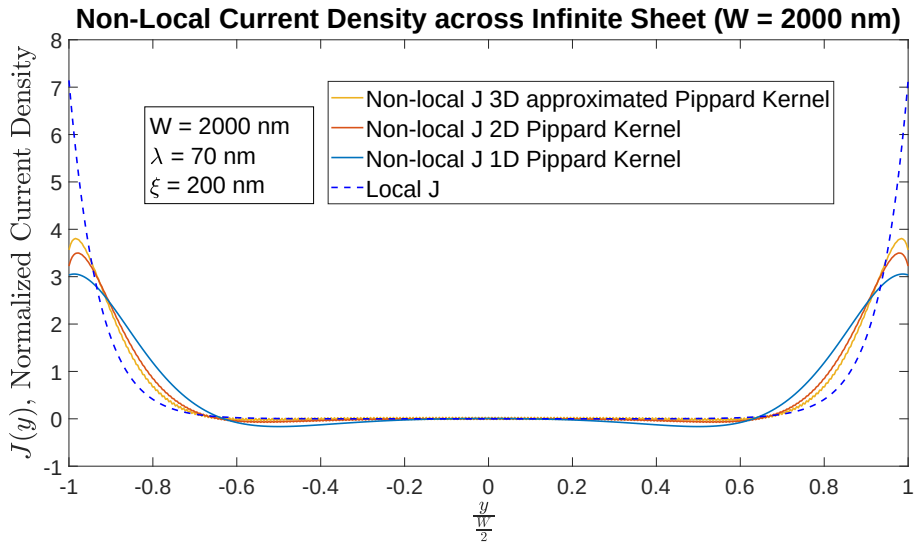

Figure 3.13: Normalized current density for infinite sheet with $W = 2000$ nm and $\xi = 200$ nm

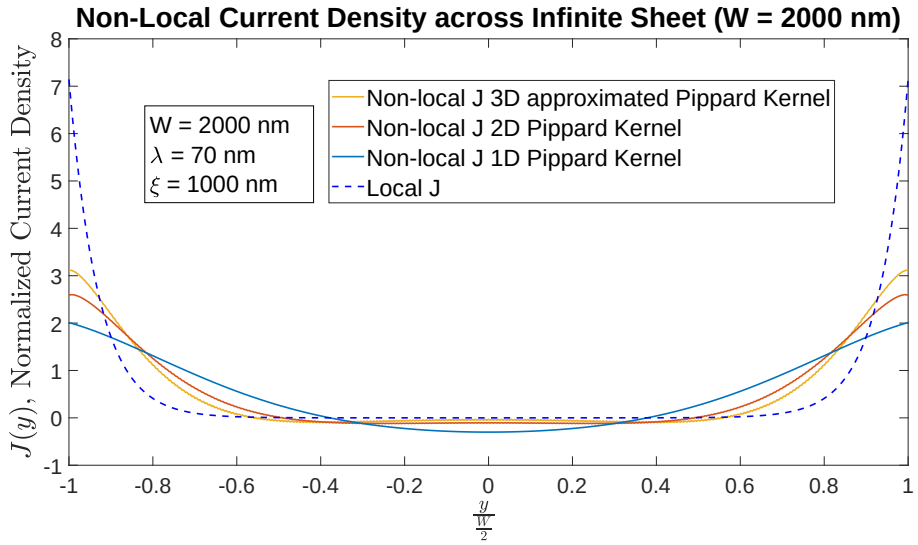

Figure 3.14: Normalized current density for infinite sheet with $W = 2000$ nm and $\xi = 1000$ nm

Interestingly, for large values of ξ, the off-edge peak seem to disappear and we have $J(y)$ having its maximum value at the edge just as in the local case. However,

unlike the local case, the majority of the current does not flow at the edge, but has a significant amount being transported in the bulk.

The trend of the 3D approximated Pippard kernel having the largest peak, the 2D kernel the next largest peak and the 1D kernel having the lowest peak is confirmed across different widths and values of ξ. This can be understood through a simple geometrical argument which is elucidated in Appendix B.

3.3 Superconducting Cylindrical Wire

3.3.1 Geometry

We consider an infinitely long, straight, cylindrical, superconducting wire, with a total current I being transported along the wire in the $\hat{z}$ direction. The penetration depth is $\lambda = 70$ nm, and we consider wire radii between $R = 500$ nm and $R = 5000$ nm.

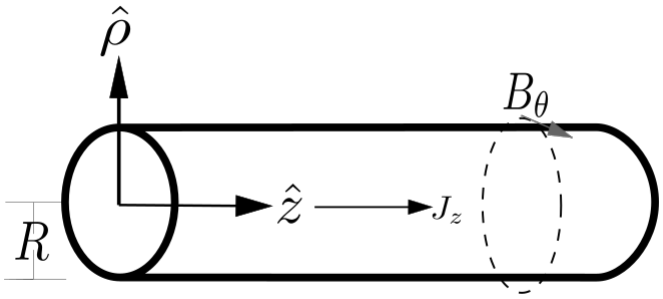

Figure 3.15: Infinite Superconducting Cylinder Geometry

3.3.2 Local London Electrodynamics

The current density and the vector potential are taken to be parallel to the z-axis,

$$\boldsymbol{J}(\boldsymbol{r}) = J(\rho)\hat{\boldsymbol{z}}, \tag{3.30}$$

$$\boldsymbol{A}(\boldsymbol{r}) = A(\rho)\hat{\boldsymbol{z}}, \tag{3.31}$$

leading to the London equation for the current in cylindrical coordinates,

$$\frac{1}{\rho}\frac{\rho\partial}{\partial\rho}\left(\frac{\partial J(\rho)}{\partial\rho}\right) = \frac{J(\rho)}{\lambda^2}. \tag{3.32}$$

The solutions to this differential equation can expressed in the form of modified Bessel functions.[2]

$$J(\rho) = c_0 I_0\left(\frac{\rho}{\lambda}\right) + c_1 K_0\left(-\frac{\rho}{\lambda}\right). \tag{3.33}$$

At $\rho = 0$, K_0 diverges, so $c_1 = 0$. Thus we get,

$$J(\rho) = c_0 I_0\left(\frac{\rho}{\lambda}\right). \tag{3.34}$$

c_0 can be determined from the total current I,

$$I = \iint_R J(\rho)dA = 2\pi c_0 \int_0^R I_0\left(\frac{\rho}{\lambda}\right)\rho d\rho = 2\pi c_0 \lambda R I_1\left(\frac{R}{\lambda}\right). \tag{3.35}$$

Thus:

$$J(\rho) = \frac{I}{2\pi\lambda R}\frac{I_0(\rho/\lambda)}{I_1(R/\lambda)}, \quad 0 \le \rho \le R. \tag{3.36}$$

And then using the London equation, we can write down the expression for $A(\rho)$ as well.

$$A(\rho) = -\frac{\lambda\mu_0 I}{2\pi R}\frac{I_0(\rho/\lambda)}{I_1(R/\lambda)}, \quad 0 \le \rho \le R. \tag{3.37}$$

3.3.3 Non-Local Pippard Electrodynamics

To solve for the vector potential and current density in a non-local scenario, we will proceed in the same manner as the previous section and use the Maxwell relation for $\boldsymbol{A}(\boldsymbol{r}) = A(\rho)\,\hat{\boldsymbol{z}}$,

$$\nabla^2 A(\rho) = -\mu_0 J(\rho), \tag{3.38}$$

$$A(\rho = R) = A_0. \tag{3.39}$$

The boundary conditions are due to the fact that we have rotational symmetry in our problem, thus the value of $A(\rho)$ must be the same on the boundary. As developed in

[2] I_0 and K_0 are modified Bessel functions of the zeroth order and first, second kinds respectively.

Appendix A, the solution for such an equation is given by,

$$A(\rho) = -\mu_0 R^2 \int\int_\Omega G(\boldsymbol{r}' - \boldsymbol{r}) J(\rho') \rho' d\rho' d\theta' - \oint_{\partial\Omega} \left[A(\rho') \boldsymbol{\nabla}_{\boldsymbol{x}'} G(\boldsymbol{r}' - \boldsymbol{r}) \right] . \hat{\boldsymbol{n}} dS. \quad (3.40)$$

In the above equation, we have factored out the radius R so that we can work with dimensionless variables. Thus the geometry we are working with is the unit disk, and the Green's function for the Laplacian on the unit disk has the form:

$$G(\boldsymbol{r}' - \boldsymbol{r}) = \frac{1}{4\pi} \ln \left[\frac{\rho^2 + .\rho'^2 - 2\rho\rho' \cos(\theta - \theta')}{\rho^2 \rho'^2 + 1 - 2\rho\rho' \cos(\theta - \theta')} \right]. \quad (3.41)$$

The unit vector perpendicular to the surface of the superconductor points out radially, $\hat{\boldsymbol{n}} = \hat{\boldsymbol{r}}$. Thus we can simplify the 2$^{\text{nd}}$ term in Equation 3.40:

$$\begin{aligned} \oint_{\partial\Omega} \left[A(\rho') \boldsymbol{\nabla}_{\boldsymbol{x}'} G(\boldsymbol{r}' - \boldsymbol{r}) \right] . \hat{\boldsymbol{n}} dS &= \int_0^{2\pi} A_0 \left(\frac{\partial}{\partial \rho'} G(\boldsymbol{r}' - \boldsymbol{r}) \right) \rho' d\theta' \Big|_{\rho'=1} && (3.42) \\ &= A_0 \int_0^{2\pi} \frac{1}{2\pi} \ln \left[\frac{1 - \rho^2}{\rho^2 + 1 - 2\rho \cos(\theta - \theta')} \right] d\theta' && (3.43) \\ &= A_0. && (3.44) \end{aligned}$$

Therefore our equation for $A(\rho)$ is,

$$A(\rho) = A_0 - \mu_0 R^2 \int_0^{2\pi} \int_0^1 G(\boldsymbol{r}' - \boldsymbol{r}) J(\rho') \rho' d\rho' d\theta'. \quad (3.45)$$

As $J(\rho')$ has no angular dependence, the integration over θ' can be performed. However, this integration is analytically intractable and must be performed numerically, which results in:

$$A(\rho) = A_0 - \mu_0 R^2 \int_0^1 G_\rho(\rho, \rho') J(\rho') \rho' d\rho'. \quad (3.46)$$

Within the integral, we can substitute the Pippard equation for non-local electrodynamics in the place of $J(\rho')$. Both the 3D approximated Pippard kernel and the 2D Pippard kernel described in Section 3.1 were used to investigate the different solutions they produced. In the below equation we use $K_{Pipp}(\rho', \rho')$ as a placeholder for either kernel, and work with dimensionless variables.

$$A(\rho) = A_0 - \mu_0 R^2 \int_0^1 \int_0^1 G_\rho(\rho, \rho') K_{Pipp}(\rho', \rho'') A(\rho'') \rho'' d\rho'' \rho' d\rho' d\theta'. \tag{3.47}$$

This is a Fredholm Integral Equation, and we can find a solution to this equation as discussed in Appendix A. Upon obtaining $A(\rho)$, we can then use the respective Pippard equation to obtain a result for $J(\rho)$. The MATLAB program FIE was used to calculate $A(\rho)$ for various values of ξ and R. The numerical integrations required to produce the Pippard kernels and the Green's function kernels were done using MATLAB's inbuilt trapezoidal integration function. The mesh for the numerical calculations was limited to 512 subdivisions, due to limitations in the computational resources. For ease of plotting, $A(\rho)$ was normalized before plotting using $\frac{A(\rho)\pi R^2}{2\pi \int_0^R A(\rho) d\rho}$.

3.3.4 Non-local Vector Potential and Current Density using the 2D Pippard Kernel

The following are the results using the 2D Pippard kernel:

$$J(\rho) = -\frac{1}{2\pi\mu_0 \xi \lambda^2} \int A(\rho') \frac{\exp\left(-\frac{|\boldsymbol{r}-\boldsymbol{r}'|}{\xi}\right)}{|\ \boldsymbol{r} - \boldsymbol{r}'\ |} \boldsymbol{d}^2\boldsymbol{r}' \tag{3.48}$$

$$= \int_0^R \left[\int_0^{2\pi} K_{2DPipp}(\theta, \theta', \rho, \rho') d\theta' \right] A(\rho') \rho' d\rho' \tag{3.49}$$

$$= \int_0^R K_{2DP}(\rho, \rho') A(\rho') \rho' d\rho'. \tag{3.50}$$

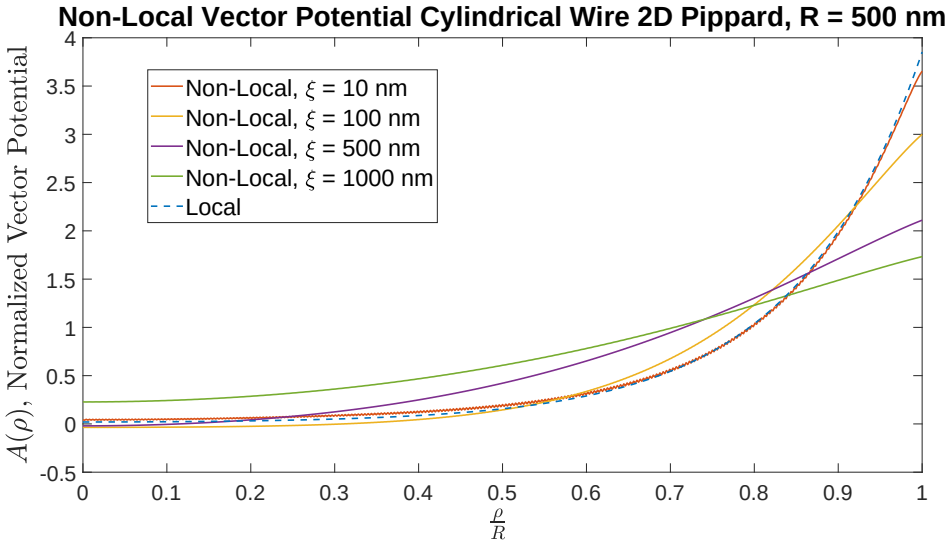

Figure 3.16: Plot of $A(\rho)$ for different values of the non-local parameter ξ for a superconducting cylinder with radius $R = 500$ nm using the 2D Pippard kernel

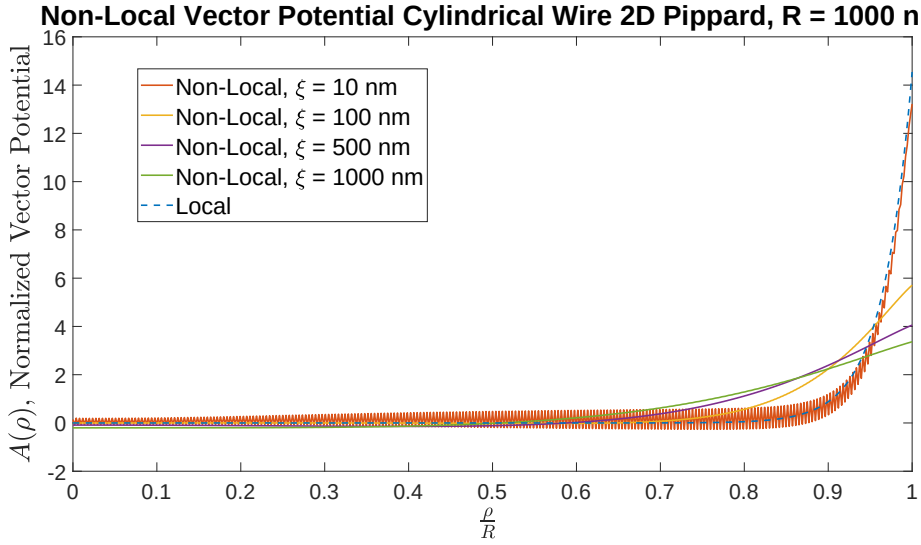

Figure 3.17: Plot of $A(\rho)$ for different values of the non-local parameter ξ for a superconducting cylinder with radius $R = 1000$ nm using the 2D Pippard kernel

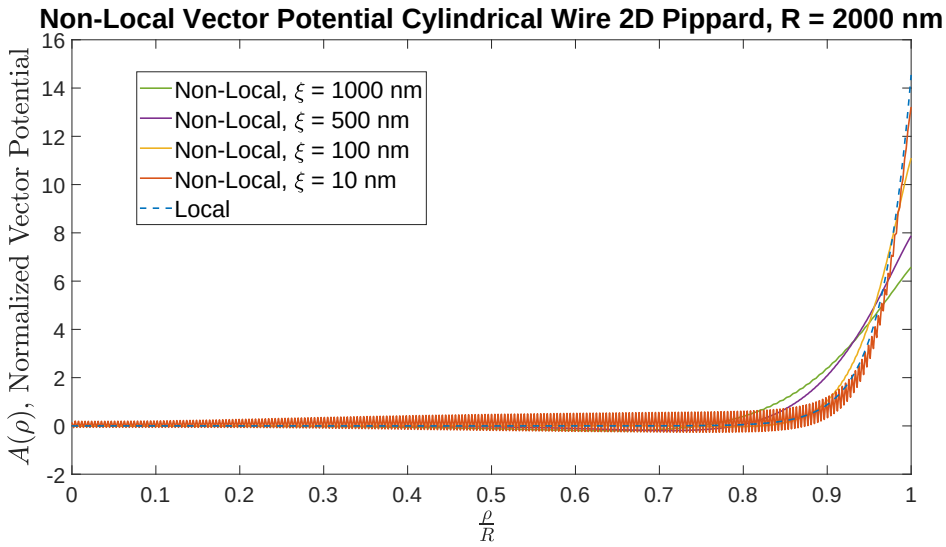

Figure 3.18: Plot of $A(\rho)$ for different values of the non-local parameter ξ for a superconducting cylinder with radius $R = 2000$ nm using the 2D Pippard kernel

The trends seen in the Infinite Sheet calculations can be see here as well:

- The non-local results show the expected convergence to the local solution as $\xi \to 0$
- Numerical oscillations can be seen as the ratio $\frac{\xi}{R}$ decreases
- As ξ increases, it flattens the distribution of $A(\rho)$.

If we run these results through the Pippard kernel, we obtain $J(\rho)$ for each case.

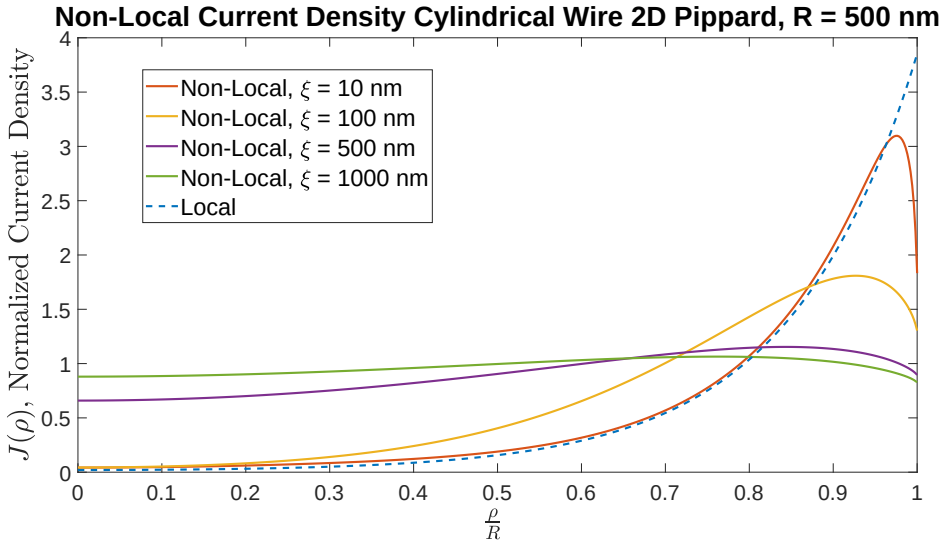

Figure 3.19: Plot of $J(\rho)$ for different values of the non-local parameter ξ for a superconducting cylinder with radius $R = 500$ nm using the 2D Pippard kernel

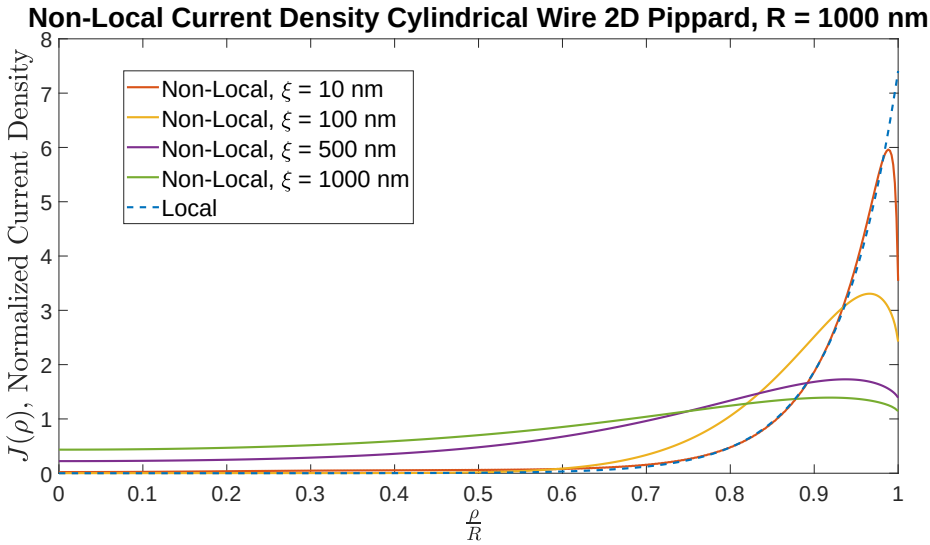

Figure 3.20: Plot of $J(\rho)$ for different values of the non-local parameter ξ for a superconducting cylinder with radius $R = 1000$ nm using the 2D Pippard kernel

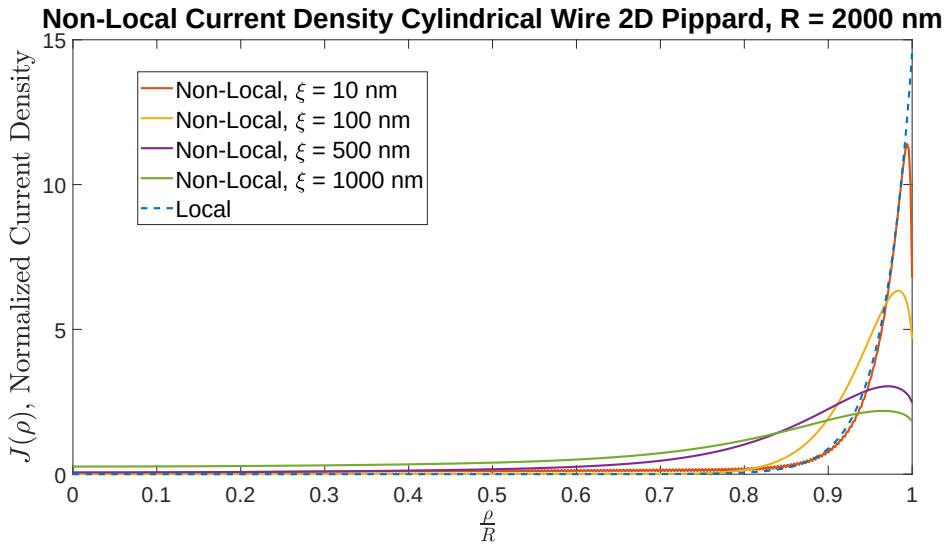

Figure 3.21: Plot of $J(\rho)$ for different values of the non-local parameter ξ for a superconducting cylinder with radius $R = 2000$ nm using the 2D Pippard kernel

These results show that non-local electrodynamics show significantly behaviour from the local case. In the local regime, $J(\rho)$ is always peaked at the edge of the superconductor and it falls of exponentially within the interior. In the non-local regime, both these qualities are not present. The peak in $J(\rho)$ is off the edge of the superconductor in this regime, and it moves inwards with increasing ξ. The current distribution is also significantly flattened, and does not display the exponential fall-off present in the local regime. Under London electrodynamics, it was assumed that the current in superconductors always flowed along the boundary; however, as all superconductors have a degree of non-locality, we can see that this does not always hold true, and a significant portion of the current can flow through the bulk.

3.3.5 Non-local Vector Potential and Current Density using the 3D Approximated Pippard Kernel

The following are the results using the 3D Approximated Pippard kernel:

$$
\begin{aligned}
J(\rho) &= -\frac{3}{8\mu_0\xi\lambda^2}\int_0^R\int_0^{2\pi} A(\rho')\frac{\exp\left[-\sqrt{1.8\frac{|\boldsymbol{r}-\boldsymbol{r}'|}{\xi}+3\frac{|\boldsymbol{r}-\boldsymbol{r}'|^2}{\xi^2}}\right]}{|\,\boldsymbol{r}-\boldsymbol{r}'\,|}\rho' d\theta' d\rho' \\
&= \int_0^R\left[\int_0^{2\pi} K_{3DApproxPipp}(\theta,\theta',\rho,\rho')d\theta'\right]A(\rho')\rho' d\rho' \\
&= \int_0^R K_{3DAP}(\rho,\rho')A(\rho')\rho' d\rho'.
\end{aligned}
\tag{3.51}
$$

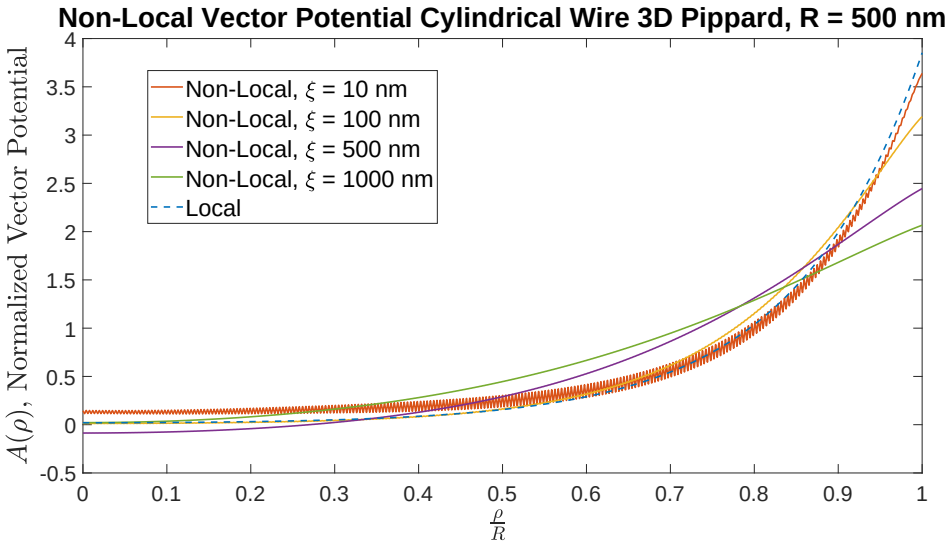

Figure 3.22: Plot of $A(\rho)$ for different values of the non-local parameter ξ for a superconducting cylinder with radius $R = 500$ nm using the 3D approximated Pippard kernel

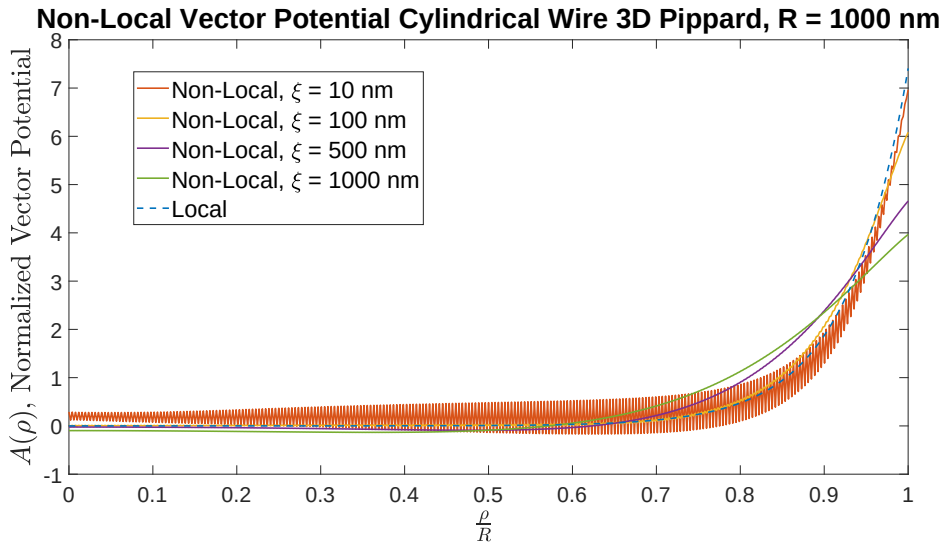

Figure 3.23: Plot of $A(\rho)$ for different values of the non-local parameter ξ for a superconducting cylinder with radius $R = 1000$ nm using the 3D approximated Pippard kernel

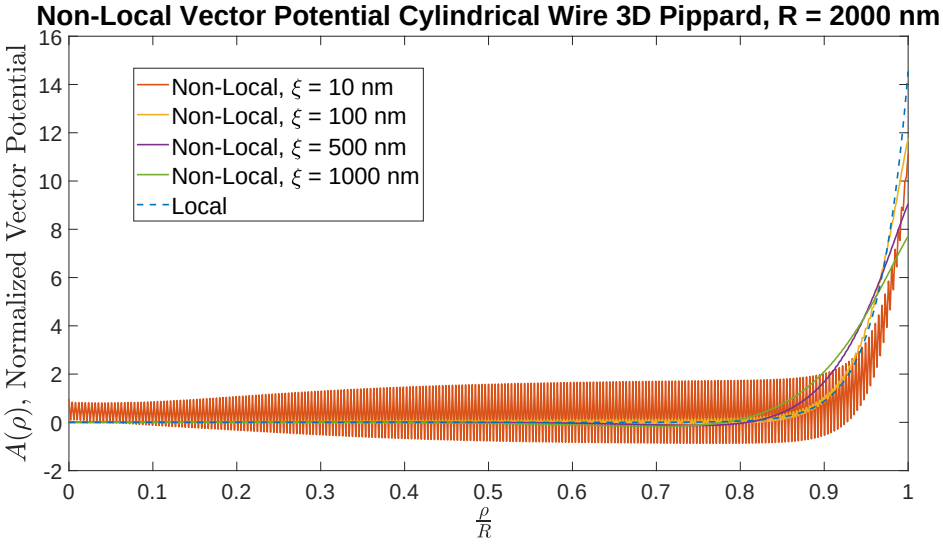

Figure 3.24: Plot of $A(\rho)$ for different values of the non-local parameter ξ for a superconducting cylinder with radius $R = 2000$ nm using the 3D approximated Pippard kernel

We can run the above results through the Pippard kernel to obtain $J(\rho)$.

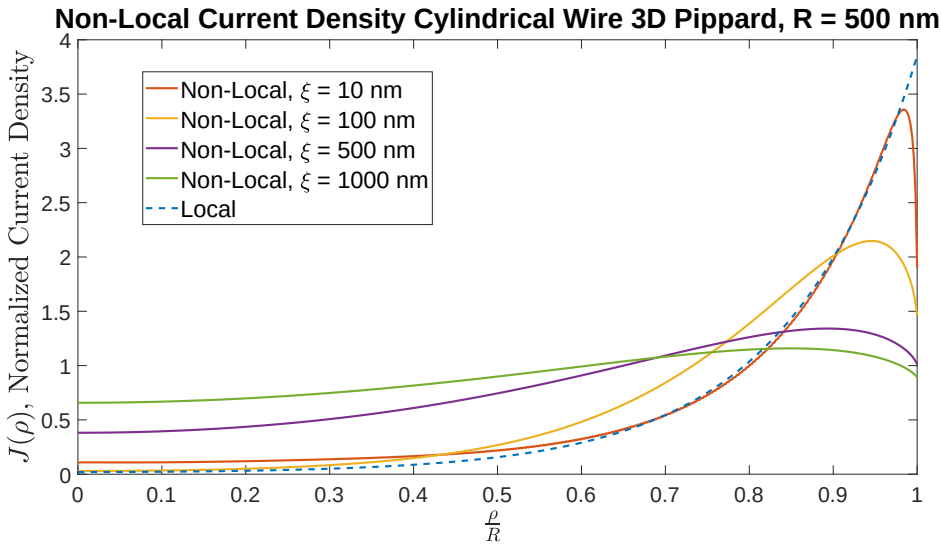

Figure 3.25: Plot of $J(\rho)$ for different values of the non-local parameter ξ for a superconducting cylinder with radius $R = 500$ nm using the 3D approximated Pippard kernel

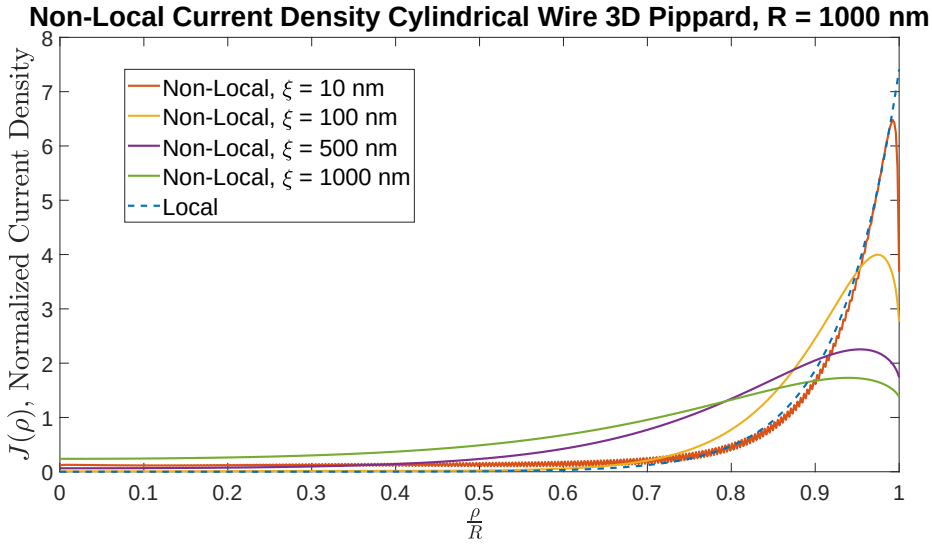

Figure 3.26: Plot of $J(\rho)$ for different values of the non-local parameter ξ for a superconducting cylinder with radius $R = 1000$ nm using the 3D approximated Pippard kernel

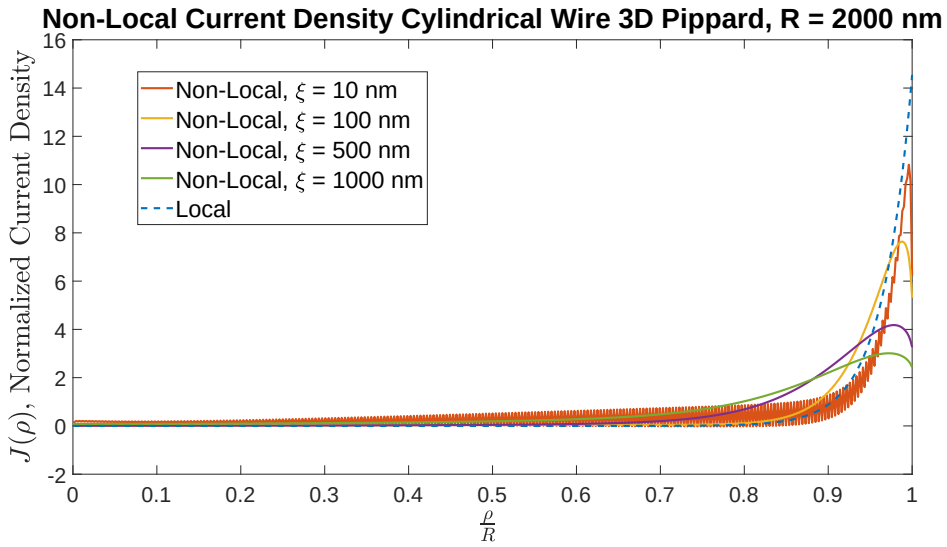

Figure 3.27: Plot of $J(\rho)$ for different values of the non-local parameter ξ for a superconducting cylinder with radius $R = 2000$ nm using the 3D approximated Pippard kernel

3.3.6 Internal Inductance and Kinetic Inductance

The expressions for the kinetic inductance, L_k, and the internal magnetic inductance, L_{int} were found in Chapter 2 to be:

$$L_k = \int_{SC} \frac{\mu_0 \lambda^2 J^2(\boldsymbol{r})}{I^2} \, d^3\boldsymbol{r}, \tag{3.52}$$

$$L_{int} = \int_{SC} \frac{B^2(\boldsymbol{r})}{\mu_0 I^2} \, d^3\boldsymbol{r}. \tag{3.53}$$

Using Ampere's law, we can derive the magnetic field inside the wire:

$$\oint \boldsymbol{B}(\boldsymbol{r}) \cdot \boldsymbol{dl} = \mu_0 I_{enc}, \tag{3.54}$$

$$B(\rho) 2\pi\rho = \mu_0 2\pi \int_0^\rho J(\rho')\rho' d\rho', \tag{3.55}$$

$$B(\rho) = \mu_0 \frac{\int_0^\rho J(\rho')\rho' d\rho'}{\rho}. \tag{3.56}$$

Performing the integral with the expression for the local $J(\rho)$ from Equation 3.36 gives,

$$B(\rho) = \frac{\mu_0}{2\pi R}\frac{I_1(\rho/\lambda)}{I_1(R/\lambda)}. \tag{3.57}$$

Therefore, the inductances per unit length in the $\hat{z}$ direction for the local case have the form,

$$\frac{L_k}{l} = \frac{\mu_0}{2\pi R^2}\frac{1}{I_1^2(\rho/\lambda)}\int_0^R I_1^2(\rho/\lambda)\, d\rho, \tag{3.58}$$

$$\frac{L_{int}}{l} = \frac{\mu_0}{2\pi R^2}\frac{1}{I_1^2(\rho/\lambda)}\int_0^R I_0^2(\rho/\lambda)\, d\rho. \tag{3.59}$$

With these expressions in hand, we can investigate the non-local effects on these quantities. We first present the results using the 2D Pippard kernel.

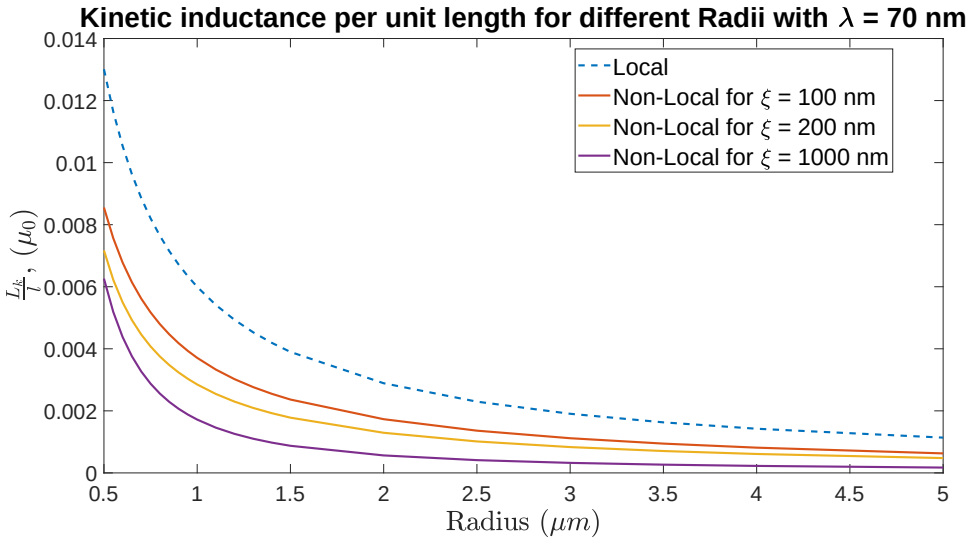

Figure 3.28: Effect of non-locality on the kinetic inductance using the 2D Pippard kernel

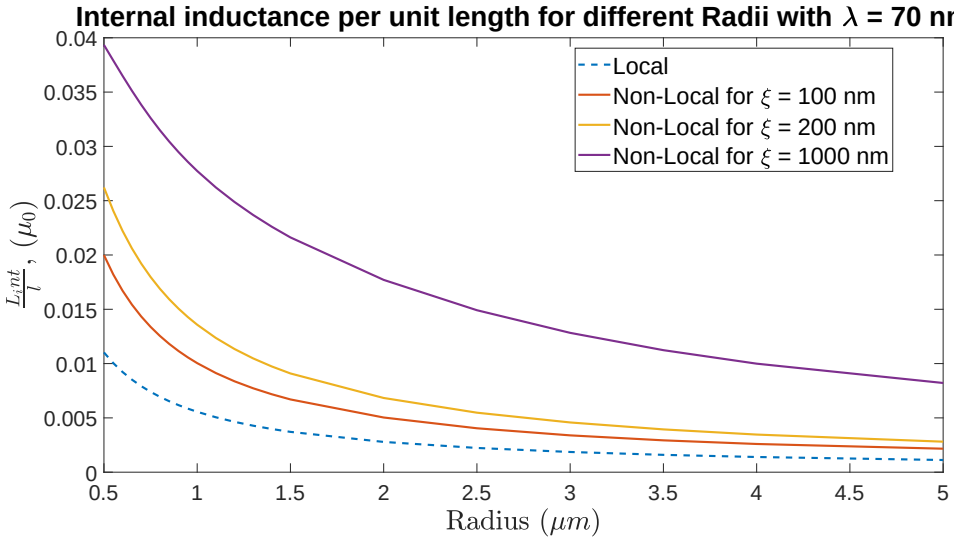

Figure 3.29: Effect of non-locality on the internal magnetic inductance using the 2D Pippard kernel

From these plots it's clear that kinetic inductance decreases as ξ increases, while the internal inductance increases.

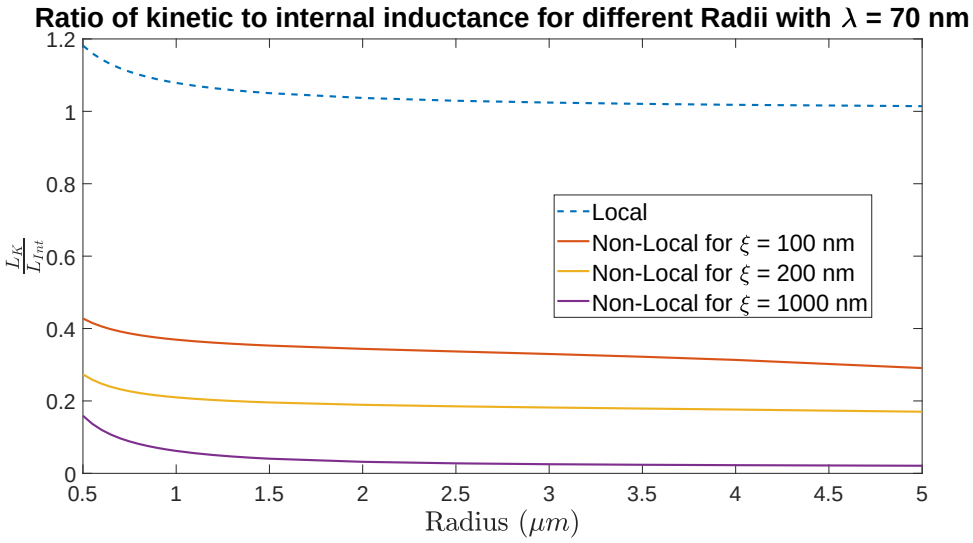

Figure 3.30: Effect of non-locality on the ratio of inductances using the 2D Pippard kernel

In the local regime, the kinetic inductance is higher than the internal magnetic

inductance for small wire radii, and approaches unity as the radius is increased. This is consistent with similar calculations performed on superconducting thin films [24]. In the non-local regime, this no longer is true; the internal magnetic inductance is always larger than the kinetic inductance, and this disparity increases as ξ increases.

The results with the 3D approximated Pippard kernel show the same trends, however the results at larger wire radii become unreliable due to numerical oscillations. The cross-over seen in the $\xi = 100$ nm and $\xi = 200$ nm case are a consequence of this numerical error and are not a physical effect.

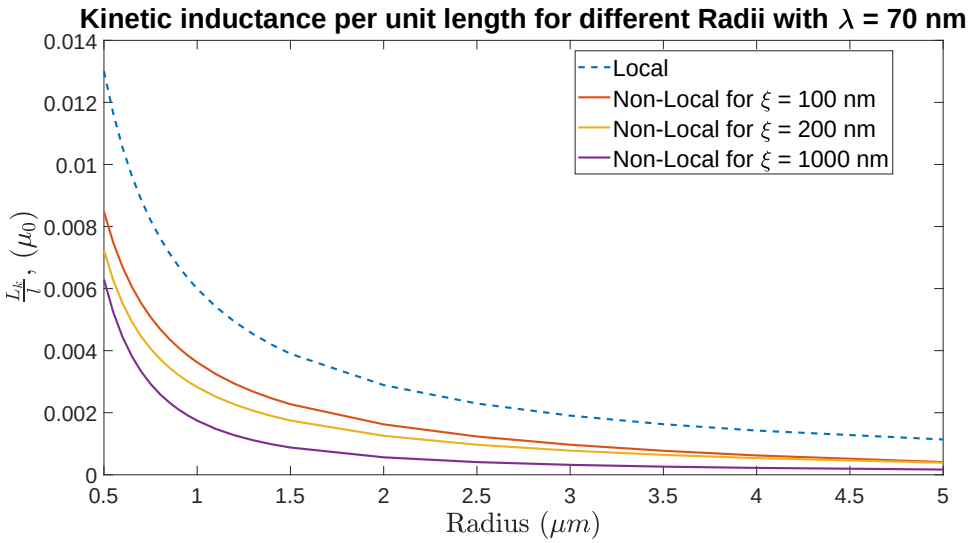

Figure 3.31: Effect of non-locality on the kinetic inductance using the 3D Pippard kernel

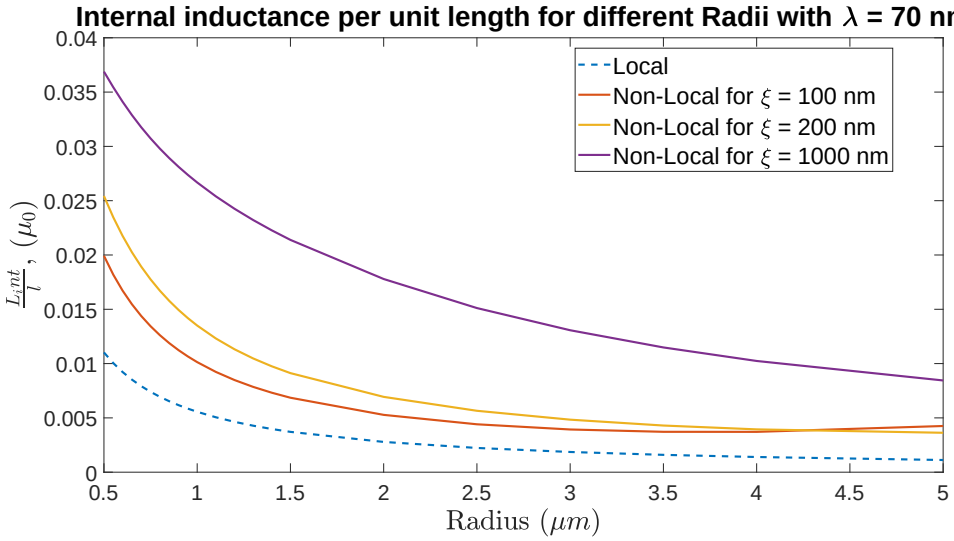

Figure 3.32: Effect of non-locality on the internal magnetic inductance using the 3D Pippard kernel

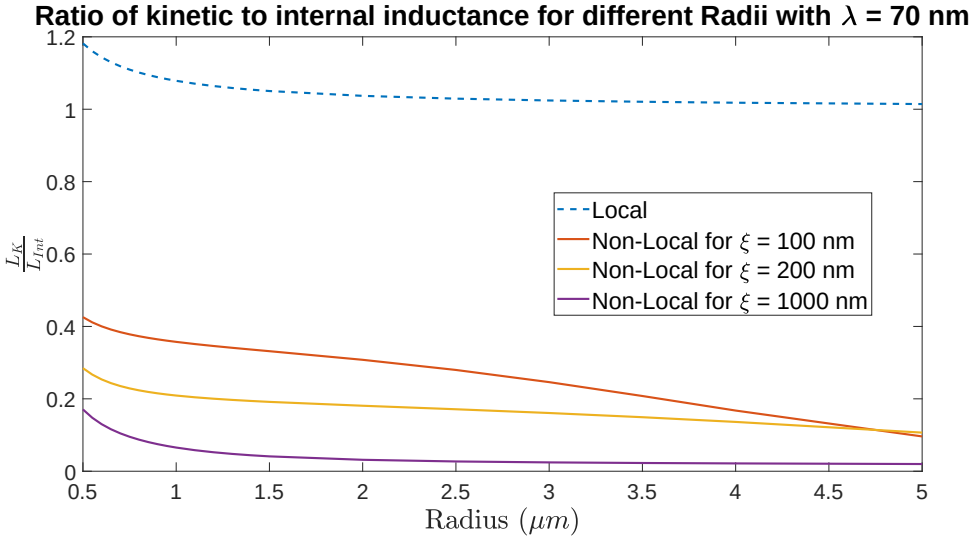

Figure 3.33: Effect of non-locality on the ratio of inductances using the 3D Pippard kernel

As a summary of this chapter, we presented a numerical method for calculations of current densities, magnetic fields, and inductances based on numerical integration

of the Fredholm equation emerging from the Pippard relation. When ξ is comparable to the length scale of the problem (thickness W for the infinite sheet or wire radius R for the cylindrical wire) the system approaches the non-local regime, where it shows magnetic properties that are qualitatively different from the local one. For example, in the non-local regime the wire's energy becomes dominated by internal inductance as opposed to kinetic inductance.

Our calculations also show the benefit of using a 2D Pippard kernel for numerical accuracy and stability. At small ξ our results using the 2D and approximate 3D Pippard kernels agree with each other and the local theory, but the 3D approximate kernel shows numerical oscillations. Thus for calculations where ξ is comparable to λ, the 2D kernel must be used for numerical accuracy. For large ξ, the approximate 3D kernel shows stable results and can be used instead of the 2D kernel.

Chapter 4

Flux Noise in SQUIDs

The flux noise in SQUIDs is believed to originate from impurities on the surface and in bulk of the superconductor. Stephanie LaForest et al. [9] have developed a model for this noise, in the form of a Hamiltonian which ties the spin of the impurity to the flux produced by the SQUID. In this chapter, we elucidate the relevant details of this theory, and then calculate the impact of non-local electrodynamics on the flux noise produced by impurities with spin located in the surface and the bulk of superconducting wires.

4.1 Flux Vector Model

In Chapter 2 Equation 2.55, we considered the flux in a superconducting loop. If we consider the flux from a spin impurity, the equation has a similar form,

$$\Phi_i = \frac{1}{I}\int \boldsymbol{A}_i(\boldsymbol{r})\cdot\boldsymbol{J}(\boldsymbol{r})\,d^3r, \tag{4.1}$$

where $\boldsymbol{A}_i(\boldsymbol{r})$ is the vector potential from the spin $\boldsymbol{s}_i$ located at $\boldsymbol{r}'$ and $\boldsymbol{J}(\boldsymbol{r})$ is the current density in the superconductor. Jackson's *Classical Electrodynamics* [25] provides an expression for the vector potential from a dipole:

$$\boldsymbol{A}_i(\boldsymbol{r}) = -\frac{g\mu_s\mu_0}{4\pi}\frac{\boldsymbol{s}_i\times(\boldsymbol{r}-\boldsymbol{r}')}{|\boldsymbol{r}-\boldsymbol{r}'|^3}, \tag{4.2}$$

where μ_s is the Bohr magneton and g is the g-factor for the electron which is ≈ 2. Plugging the above expression into Equation 4.1, we can write $\Phi_i = -\boldsymbol{F}(\boldsymbol{r}')\cdot\boldsymbol{s}_i$ with,

$$\boldsymbol{F}(\boldsymbol{r}') = \frac{g\mu_s\mu_0}{4\pi}\int \frac{(\boldsymbol{r}-\boldsymbol{r}')\times\boldsymbol{J}(r)}{|\boldsymbol{r}-\boldsymbol{r}'|^3 I}\,d^3r. \tag{4.3}$$

$\boldsymbol{F}(\boldsymbol{r}')$ is called the flux vector, and is simply the Biot-Savart equation for the magnetic field multiplied by $g\mu_s$,

$$\boldsymbol{F}(\boldsymbol{r}') = g\mu_s \boldsymbol{B}(\boldsymbol{r}'). \tag{4.4}$$

For the infinite cylinder geometry we consider, the magnetic field is $\boldsymbol{B}(\boldsymbol{r}') = B(\rho')\,\hat{\boldsymbol{\theta}}$, and can be expressed using Ampère's Law as,

$$B(\rho') = \mu_0 \frac{\int_0^{\rho'} J(\rho)\rho d\rho}{\rho'}. \tag{4.5}$$

Therefore the flux vector can be simplified to:

$$\boldsymbol{F}(\boldsymbol{r}') = F_\theta(\rho') = g\mu_s B(\rho')\,\hat{\boldsymbol{\theta}}. \tag{4.6}$$

4.2 Effect of Non-Locality

Here we present calculations of various quantities relevant for flux noise, using the non-local current density and vector potential calculations of the superconducting cylindrical wire with the 2D Pippard kernel. The results using the 3D approximated Pippard kernel are similar to the results obtained using the 2D Pippard kernel. The figures resulting from the 3D approximated Pippard can be found in Appendix C

4.2.1 Flux Vector

In the local regime, the flux vector inside a cylindrical wire becomes,

$$F_\theta(\rho) = \frac{g\mu_s\mu_0 I}{2\pi R}\frac{I_1(\rho/\lambda)}{I_1(R/\lambda)}, \quad 0 \le \rho \le R, \tag{4.7}$$

where we used our analytical expression for the magnetic field, Equation 3.57. For the non-local flux vector, we use the numerically computed $J(\rho)$ in the equation:

$$F_\theta(\rho) = \frac{g\mu_s\mu_0}{I}\frac{\int_0^{\rho} J(\rho')\rho' d\rho'}{\rho}, \quad 0 \le \rho \le R. \tag{4.8}$$

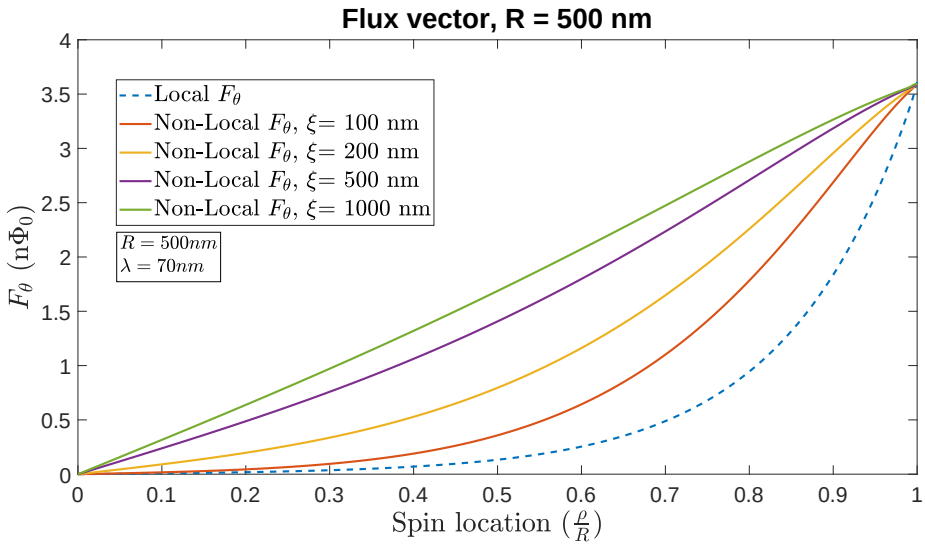

Figure 4.1: Flux Vector in the Non-Local versus Local regime for $R = 500$ nm using the 2D Pippard kernel

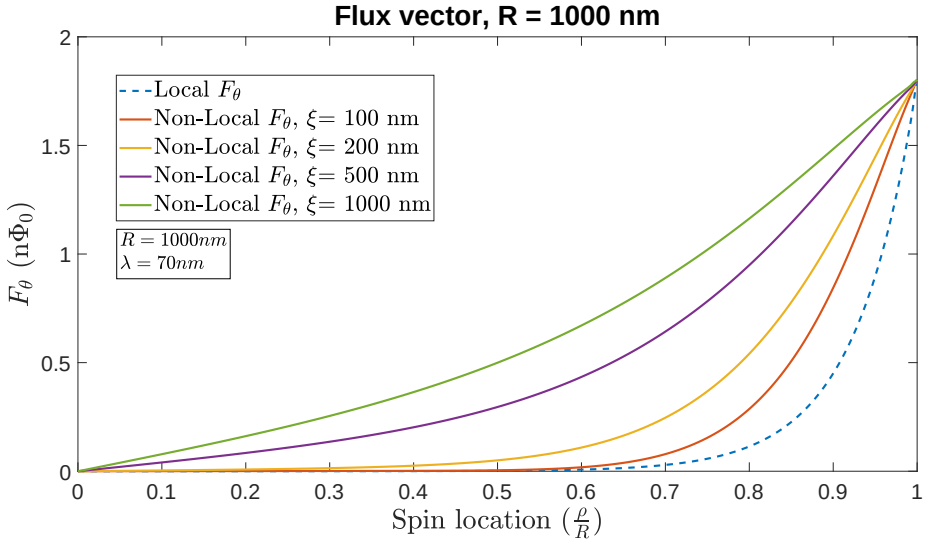

Figure 4.2: Flux Vector in the Non-Local versus Local regime for $R = 1000$ nm using the 2D Pippard kernel

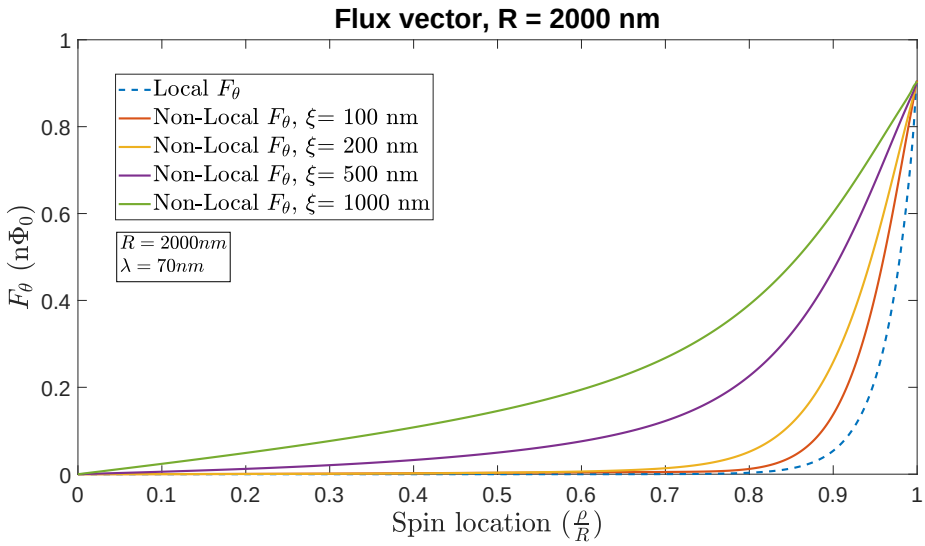

Figure 4.3: Flux Vector in the Non-Local versus Local regime for $R = 2000$ nm using the 2D Pippard kernel

The above results show that the flux vector can have non-zero value even when the spin is located near the center of the cylinder, when ξ is large in comparison to the radius. The non-local flux vector shows convergence towards the local value as $\xi \to 0$.

4.2.2 Flux Noise Power

We can use the flux vector to calculate the total flux noise power. The flux noise power per unit length for surface spins is:

$$\frac{\langle \Phi^2 \rangle}{L} = \frac{s(s+1)}{3}\sigma_2 \int_0^{2\pi} |\boldsymbol{F}(\rho)|^2 \rho d\theta|_{\rho=R} = \frac{s(s+1)}{3} 2\pi R \sigma_2 |\boldsymbol{F}(R)|^2, \tag{4.9}$$

and for bulk spins is:

$$\frac{\langle \Phi^2 \rangle}{L} = \frac{s(s+1)}{3}\sigma_3 \int_0^{R}\int_0^{2\pi} |\boldsymbol{F}(\rho)|^2 \rho d\theta d\rho = \frac{s(s+1)}{3} 2\pi \sigma_3 \int_0^{R} |\boldsymbol{F}(\rho)|^2 \rho d\rho, \tag{4.10}$$

where s is the total spin quantum number of the impurity (taken to be $s = \frac{1}{2}$ in explicit numerical results) and σ_2 is the density of spins on the surface of the superconductor and σ_3 is the density of spins in the bulk of the superconductor. We

use values of $\sigma_2 = 5 \times 10^{16}\, m^{-2}$ and $\sigma_3 = 10^{24}\, m^{-3}$ in our calculations.

As the surface flux noise power depends on the value of the flux vector at the surface, the noise in the local and non-local regimes are identical. However, the bulk flux noise power is proportional to the integral of the flux vector over the volume of the superconductor, thus the non-local regime will have larger bulk noise.

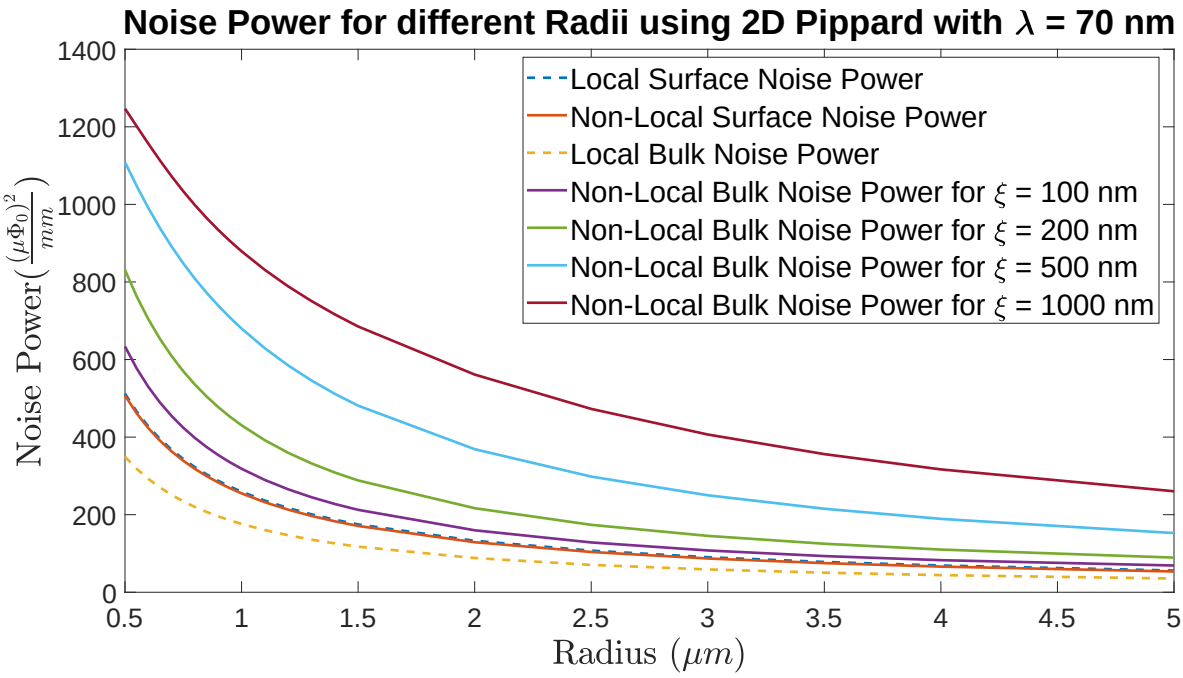

Figure 4.4: Flux Noise Power for 2D Pippard with increasing non-locality

From the above plot it is clear that the bulk noise power increases as ξ increases. As the radius increases, the non-local bulk noise power approaches the local result asymptotically.

Chapter 5

Conclusions

The aim of this thesis was twofold: to determine the non-local electrodynamic behaviour of a superconducting wire, and to investigate the impact of non-locality on the inductance and flux noise of a SQUID. The first aim was fulfilled through developing a Green's function approach to form the non-local electrodynamic equations, and using MATLAB to obtain explicit numerical results. In pursuing these goals, we developed a 1D and 2D analogue to the Pippard equations, and an approximation to the 3D Pippard equation. Through comparing the results from these three equations, we determined that the 2D Pippard equation should be used when ξ is smaller than or comparable to λ and the superconductor length scale. The 3D approximation was found to be numerically stable for large values of ξ.

We obtained results using these equations for 2 geometries; the infinite superconducting sheet and the cylindrical wire. The sheet can serve as an idealized model of the ground plane used in many superconducting devices, and the cylinder serves as a model of a coaxial cable.

Our calculations of the non-local vector potential (See Figures in Chapter 3 Section 3.3) showed that the distribution was flattened with increasing non-locality. This is in qualitative agreement with simple models of non-local electrodynamics (See [19] Equation 3-13) in which the effect of the Pippard equation is given as a modification of the penetration depth, $\lambda_{NL} = 0.58(\lambda^2\xi_0)^{\frac{1}{3}}$. However this does not give a good qualitative description of how the current density behaves inside the wire. Notably, the calculations in this thesis show that the peak of the current density distribution is off the edge of the superconductor in the non-local regime, and is significantly distributed within the bulk of the superconductor.

In satisfying the second aim of this thesis, it was found that the bulk noise power and the internal inductance of the superconducting cylinder increased with increas-

ing non-locality. The kinetic inductance was found to decrease with increasing non-locality, and the surface flux noise power was found to be the same as in the local regime. For all radii investigated in the local regime the surface flux noise power dominated the bulk flux noise power, and the kinetic inductance dominated the internal inductance. In contrast, these relationships were inverted in the non-local regime; the bulk noise power and the internal inductance were the dominant quantities for all cylinder radii.

The results found in this thesis show that the electrodynamics of non-local superconductors differ markedly from local superconductors, and in building nano-scale devices, care must be taken to incorporate these effects into the design. As flux noise is a persistent problem encountered in SQUIDs, we hope our results can be used in improving SQUID design in the future.

Appendix A

Mathematical Tools

Performing calculations on the non-local electrodynamics of superconductors requires many different sophisticated mathematical tools. In this appendix, we will introduce the two main tools that were instrumental in producing the results herein:

1. Nyström Method for solving Fredholm Integral Equations
2. Green's Function Method for solving Poisson's equation boundary value problems

A.1 Fredholm Integral Equations

A Fredholm Integral Equation of the 2^{nd} kind is an equation of the form,

$$\lambda F(x) = \int_a^b K(x, x')F(x')dx' + G(x). \tag{A.1}$$

Here, $F(x)$ is the desired function and we see that it has a self-consistent relation - $F(x)$ is equal to the convolution of itself with some specified kernel $K(x, x')$ plus a given function $G(x)$.
This can be written symbolically as,

$$\lambda F = KF + G, \tag{A.2}$$

$$or \tag{A.3}$$

$$(\lambda - K)F = G. \tag{A.4}$$

This equation can be solved on the interval $[a, b]$ through discretizing x into $n-1$ parts:

$$x = a, a+h, a+2h, ..., b \tag{A.5}$$

$$= x_1, x_2, ..., x_n, \tag{A.6}$$

where $h = \frac{b-a}{n-1}$.

The integral can then be turned into a sum through a quadrature scheme, with appropriate weighting, w_j:

$$\int_a^b K(x,x')F(x')dx' \approx \sum_{j=1}^{n} w_j K(x,x'_j)F(x'_j). \tag{A.7}$$

Thus the value of $F(x_i)$ at any x_i is,

$$\lambda F(x_i) = \sum_{j=1}^{n} w_j K(x_i,x'_j)F(x'_j) + G(x_i). \tag{A.8}$$

We now have n equations and n unknowns, which can solved through inverting the matrix $(\lambda - K)$:

$$F = (\lambda - K)^{-1}G. \tag{A.9}$$

This method of solving Fredholm integral equations is known as the Nyström method. FIE, a MATLAB program implementing a sophisticated version of the above Nyström scheme, has been developed by K.E. Atkinson and L. F. Shapine [26]. This program was used to solve all Fredholm integral equations in this thesis.

A.2 Green's Functions

An equation of the form $\nabla^2_{\mathbf{x}}\phi(\boldsymbol{x}) = f(\boldsymbol{x})$ is known as Poisson's equation, which is simply a generalization of Laplace's equation with the addition of the source term on the right hand side, f. The Laplace operator has the form $\nabla^2 = \frac{\partial^2}{\partial x_1^2} + \frac{\partial^2}{\partial x_2^2} + ... + \frac{\partial^2}{\partial x_n^2}$ in n dimensions. In Poisson's equation, we are attempting to find the value of $\phi(\boldsymbol{x})$ in some domain Ω, when given some information about $\phi(\boldsymbol{x})$ on the boundary of this domain, $\partial\Omega$. If the information is about the value of $\phi(\boldsymbol{x})$ itself on the boundary, this is known as a Dirichlet boundary condition. If the information is about the value of $(\boldsymbol{\nabla}_{\mathbf{x}}\phi(\boldsymbol{x})) \cdot \hat{\boldsymbol{n}}$ on the boundary, where $\hat{\boldsymbol{n}}$ is the unit vector normal to the boundary $\partial\Omega$, it is known as a Neumann boundary condition.

For the purposes of this thesis we will be focusing on solving Poisson's equation in 1D and 2D, with Dirchlet boundary conditions. To see how Green's functions can be employed to obtain a solution, we first define the Green's function in a Dirchlet boundary condition setting:

$$\nabla^2_{\mathbf{x}} G(\boldsymbol{x} - \boldsymbol{x}') = \delta(\boldsymbol{x} - \boldsymbol{x}'), \tag{A.10}$$

$$G(\boldsymbol{x} - \boldsymbol{x}')\big|_{\mathbf{x},\mathbf{x}' \in \partial\Omega} = 0. \tag{A.11}$$

The Green's function is a function that yields a Dirac-delta when operated upon by the Laplacian, and has a value of 0 on the boundary of the domain [1]. In general, this can be defined for any operator - not just the Laplacian. We will now illustrate the utility of this function in solving Poisson's equation in 1D and 2D setting.

A.2.1 1D Poisson equation

We are seeking the solution for a function $\phi(x)$ over some domain $x \in [a, b]$. In 1D, the Laplacian is simply the double derivative: $\nabla^2 = \frac{\partial^2}{\partial x^2}$. Thus Poisson's equation is,

$$\frac{\partial^2}{\partial x^2}\phi(x) = f(x). \tag{A.12}$$

As we are considering Dirichlet boundary conditions, we know the value of $\phi(x)$ on $\partial\Omega : x = \{a, b\}$,

$$\phi(a) = \phi_a, \phi(b) = \phi_b. \tag{A.13}$$

The Green's function is defined as,

$$\frac{\partial^2}{\partial x^2} G(x - x') = \delta(x - x'), \tag{A.14}$$

$$G(x - x')\big|_{x,x' \in \partial\Omega} = 0. \tag{A.15}$$

Using the product rule of differentiation, we can take the Laplacian of the product of the Green's function and $\phi(x')$ (the primed and unprimed coordinates are switched

[1] For a Neumann problem, we would have a similar condition: that $(\boldsymbol{\nabla}_{\mathbf{x},\mathbf{x}'} G(\boldsymbol{x} - \boldsymbol{x}') \cdot \hat{\boldsymbol{n}} = 0$ but the general solution to the Poisson equation has a subtle difference which is not present in the Dirichlet picture.

for clarity of notation in the final solution).

$$\frac{\partial^2}{\partial x'^2}(G(x'-x)\phi(x')) = \frac{\partial^2 G(x'-x)}{\partial x'^2}\phi(x') + G(x'-x)\frac{\partial^2\phi(x')}{\partial x'^2} + 2\frac{\partial G(x'-x)}{\partial x'}\frac{\partial\phi(x')}{\partial x'} \tag{A.16}$$

We can now make use of the fact that,

$$\frac{\partial G(x'-x)}{\partial x'}\frac{\partial\phi(x')}{\partial x'} = \frac{\partial}{\partial x'}\left(G(x'-x)\frac{\partial\phi(x')}{\partial x'}\right) - G(x'-x)\frac{\partial^2\phi(x')}{\partial x'^2} \tag{A.17}$$

This gives,

$$\begin{aligned}\frac{\partial^2}{\partial x'^2}(G(x'-x)\phi(x')) &= \frac{\partial^2 G(x'-x)}{\partial x'^2}\phi(x') - G(x'-x)\frac{\partial^2\phi(x')}{\partial x'^2} + 2\frac{\partial}{\partial x'}\left(G(x'-x)\frac{\partial\phi(x')}{\partial x'}\right) \\ &= \delta(x'-x)\phi(x') - G(x'-x)f(x') + 2\frac{\partial}{\partial x'}\left(G(x'-x)\frac{\partial\phi(x')}{\partial x'}\right).\end{aligned} \tag{A.18}$$

In the last line, we've used Equation A.14 to insert the delta function and Equation A.12 to insert $f(x')$.

We can now integrate over the domain $x' \in [a, b]$.

$$\begin{aligned}\int_a^b \frac{\partial^2}{\partial x'^2}(G(x'-x)\phi(x'))dx' = &\int_a^b \delta(x'-x)\phi(x')dx' - \int_a^b G(x'-x)f(x')dx' \\ &+ 2\int_a^b \frac{\partial}{\partial x'}\left(G(x'-x)\frac{\partial\phi(x')}{\partial x'}\right)dx,\end{aligned} \tag{A.19}$$

$$\implies \frac{\partial}{\partial x'}(G(x'-x)\phi(x'))\Big|_a^b = \phi(x) - \int_a^b G(x'-x)f(x')dx' + 2G(x'-x)\frac{\partial\phi(x')}{\partial x'}\Big|_a^b. \tag{A.20}$$

The 3^{rd} term in the above equation will disappear as we defined the Green's function to vanish on the boundary.

$$\implies \frac{\partial G(x'-x)}{\partial x'}\phi(x')\Big|_a^b + G(x'-x)\frac{\partial\phi(x')}{\partial x'}\Big|_a^b = \phi(x) - \int_a^b G(x'-x)f(x')dx'. \tag{A.21}$$

We can see that the first term is some function with x-dependence which can be calculated from the Green's function, thus we replace it with $h(x) = \frac{\partial G(x'-x)}{\partial x'}\Big|_b \phi_b - \frac{\partial G(x'-x)}{\partial x'}\Big|_a \phi_a$. The second term on the left hand side vanishes as we stipulated that the Green's function is 0 on the boundary in Equation A.15. Thus the solution is,

$$\phi(x) = h(x) + \int_a^b G(x'-x) f(x') dx'. \tag{A.22}$$

Thus we have arrived at a solution for $\phi(x)$ without reference to the actual form of the function $G(x'-x)$. For many problems, the most difficult aspect of the solution is in finding a Green's function which satisfies the conditions in Equation A.15 for the geometry of the problem. In fact, a simple, closed form for the Green's function can only be found in a few highly idealized geometries.

A.2.2 2D Poisson equation

We are seeking the solution for a function $\phi(\boldsymbol{x})$ over some domain $\Omega : \boldsymbol{x} = (x, y)$ with boundary $\partial\Omega$. In 2D, the Laplacian is s $\nabla^2_{\boldsymbol{x}} = \frac{\partial^2}{\partial x^2} + \frac{\partial^2}{\partial y^2}$. Assuming the value of $\phi(\boldsymbol{x})$ on the boundary is constant [2], the problem to be solved is:

$$\nabla^2_{\boldsymbol{x}} \phi(\boldsymbol{x}) = f(\boldsymbol{x}), \tag{A.23}$$

$$\phi(\boldsymbol{x})\big|_{\partial\Omega} = c. \tag{A.24}$$

[2] This does not have to be the case, but makes the problem easier to solve. The derivation still holds for a case where the boundary value of $\phi(x)$ has coordinate dependence.

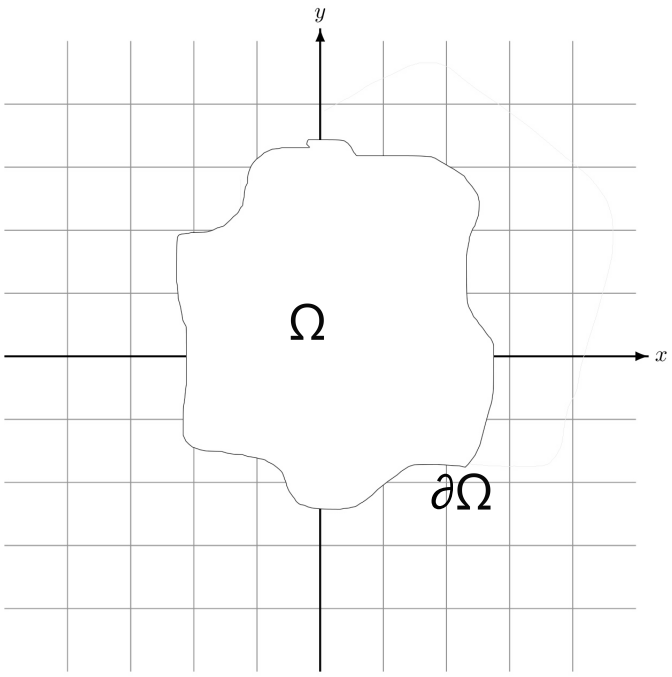

Figure A.1: Schematic diagram of the space on which Poisson's equation is being solved

The Green's function is defined as,

$$\nabla^2_{\boldsymbol{x}} G(\boldsymbol{x}-\boldsymbol{x}') = \delta(\boldsymbol{x}-\boldsymbol{x}'), \tag{A.25}$$

$$G(\boldsymbol{x}-\boldsymbol{x}')\big|_{\boldsymbol{x},\boldsymbol{x}'\in\partial\Omega} = 0. \tag{A.26}$$

To solve the problem in 2D, we must apply Green's theorem[3]. For some vector $\boldsymbol{F}$, this can be written as,

$$\int\int_{\Omega} (\boldsymbol{\nabla}\cdot\boldsymbol{F})dxdy = \oint_{\partial\Omega} (\boldsymbol{F}\cdot\hat{\boldsymbol{n}})ds. \tag{A.27}$$

As this holds for any vector function, choose $\boldsymbol{F} = \phi(\boldsymbol{x'})\boldsymbol{\nabla}_{\boldsymbol{x}'}G(\boldsymbol{x}'-\boldsymbol{x})$. Thus Equation A.27 becomes,

$$\int\int_{\Omega} \left[(\boldsymbol{\nabla}_{\boldsymbol{x}'}\phi(\boldsymbol{x}')).(\boldsymbol{\nabla}_{\boldsymbol{x}'}G(\boldsymbol{x}'-\boldsymbol{x})) - \phi(\boldsymbol{x}')\nabla^2_{\boldsymbol{x}'}G(\boldsymbol{x}'-\boldsymbol{x})\right] d^2\boldsymbol{x}' = \oint_{\partial\Omega} ((\phi(\boldsymbol{x}')\boldsymbol{\nabla}_{\boldsymbol{x}'}G(\boldsymbol{x}'-\boldsymbol{x}))\cdot\hat{\boldsymbol{n}})ds. \tag{A.28}$$

[3]Equivalent to divergence theorem or Stoke's theorem in 2D space

With this in hand, let's repeat the process with $\boldsymbol{F} = G(\boldsymbol{x'} - \boldsymbol{x})\boldsymbol{\nabla}_{\boldsymbol{x'}}\phi(\boldsymbol{x'})$. This produces,

$$\int\int_{\Omega}\left[(\boldsymbol{\nabla}_{\boldsymbol{x'}}G(\boldsymbol{x'}-\boldsymbol{x})).(\boldsymbol{\nabla}_{\boldsymbol{x'}}\phi(\boldsymbol{x'}))-G(\boldsymbol{x'}-\boldsymbol{x})\nabla^2_{\boldsymbol{x'}}\phi(\boldsymbol{x'})\right]d^2\boldsymbol{x'}d^2\boldsymbol{x'} = \oint_{\partial\Omega}(G(\boldsymbol{x'}-\boldsymbol{x})\boldsymbol{\nabla}_{\boldsymbol{x'}}\phi(\boldsymbol{x'}))\cdot\hat{\boldsymbol{n}})ds. \tag{A.29}$$

Now if we subtract Equation A.28 from Equation A.29, the first terms of both equations disappear as $(\boldsymbol{\nabla}_{\boldsymbol{x'}}G(\boldsymbol{x'} - \boldsymbol{x})) \cdot (\boldsymbol{\nabla}_{\boldsymbol{x'}}\phi(\boldsymbol{x'})) = (\boldsymbol{\nabla}_{\boldsymbol{x'}}\phi(\boldsymbol{x'})) \cdot (\boldsymbol{\nabla}_{\boldsymbol{x'}}G(\boldsymbol{x'} - \boldsymbol{x}))$. The second terms of each equation can also be reduced using the definitions of the Green's function and Poisson's equation respectively. Rearranging the resultant equation we arrive at the solution:

$$\phi(\boldsymbol{x}) = \int\int_{\Omega}\left[G(\boldsymbol{x'}-\boldsymbol{x})f(\boldsymbol{x'})\right]d^2\boldsymbol{x'}+\oint_{\partial\Omega}\left[G(\boldsymbol{x'}-\boldsymbol{x})\boldsymbol{\nabla}_{\boldsymbol{x'}}\phi(\boldsymbol{x'})-\phi(\boldsymbol{x'})\boldsymbol{\nabla}_{\boldsymbol{x'}}G(\boldsymbol{x'}-\boldsymbol{x})\right]\cdot\hat{\boldsymbol{n}}ds. \tag{A.30}$$

As we chose the Green's function to have a value of zero at the boundary, this can be simplified further. With this, we finally arrive at the solution to Poisson's equation in 2D with Dirichlet boundary conditions:

$$\phi(\boldsymbol{x}) = \int\int_{\Omega} G(\boldsymbol{x'} - \boldsymbol{x})f(\boldsymbol{x'})d^2\boldsymbol{x'} - \oint_{\partial\Omega}\left[\phi(\boldsymbol{x'})\boldsymbol{\nabla}_{\boldsymbol{x'}}G(\boldsymbol{x'} - \boldsymbol{x})\right] \cdot \hat{\boldsymbol{n}}ds. \tag{A.31}$$

Appendix B

1D vs 2D vs 3D Pippard Kernel: Geometrical Argument

The differences between using the 1D, 2D or 3D Pippard kernel can be understood by considering the physical situation described by the Pippard equation. The Pippard equation describes the current density inside a superconductor at a given point, being dependent on the convolution of the vector potential around that point with a given kernel. The kernel can be thought of as being Gaussian; the highest contribution to the current density is the vector potential at the point in question, and then the contributions fall of exponentially with the radial distance from that point.

The off-edge peaks of the current density is a consequence of this; as the integral is confined to the interior of the superconductor, when calculating the current density at the edge versus the middle, a larger part of the kernel is located outside the superconductor. However, the vector potential is also peaked higher at the edge than at the middle, therefore the off-edge peak for the current density is a result of the competition between these two factors.

When considering the effect of the 2D versus 3D Pippard equation in this context, we can consider a simpler kernel to illustrate its effects. Instead of a 2D or 3D Gaussian, consider kernels of uniform 1D, 2D and 3D unit-radii spheres (A 1D sphere is a line, and a 2D sphere is a circle). As we move these objects towards the edge (intersection of the d-dimensional sphere with a (d-1)-dimensional plane), a portion of the kernel moves outside the superconductor. Taking the ratio of the volume outside the superconductor to the total volume illustrates the differences between each kernel.

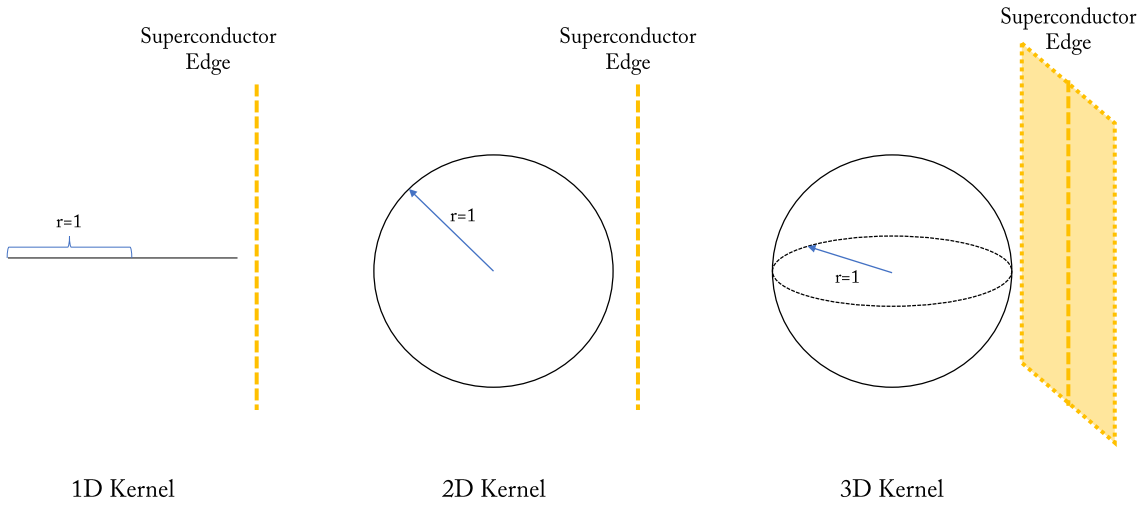

Figure B.1: Simplified spherical kernels in each dimension. Moving each kernel to the right causes it to intersect with the edge of the superconductor, and only the volume inside the superconductor contributes to the current density.

Let x be the distance perpendicular to the edge to which the kernel extends outside. The ratios for the volume outside to the total volume for the 1D, 2D and 3D kernels are given by,

$$
\begin{aligned}
R_{1D}(x) &= \frac{x}{2}, \\
R_{2D}(x) &= \frac{\arccos(1-x) - \sin(\arccos(1-x))}{2\pi}, \\
R_{3D}(x) &= \frac{x^2(3-x)}{4}.
\end{aligned}
$$

Plotting this for $x = 0$ to $x = 1$ corresponds to to moving the kernels from touching the edge till the center of the kernels are on the edge.

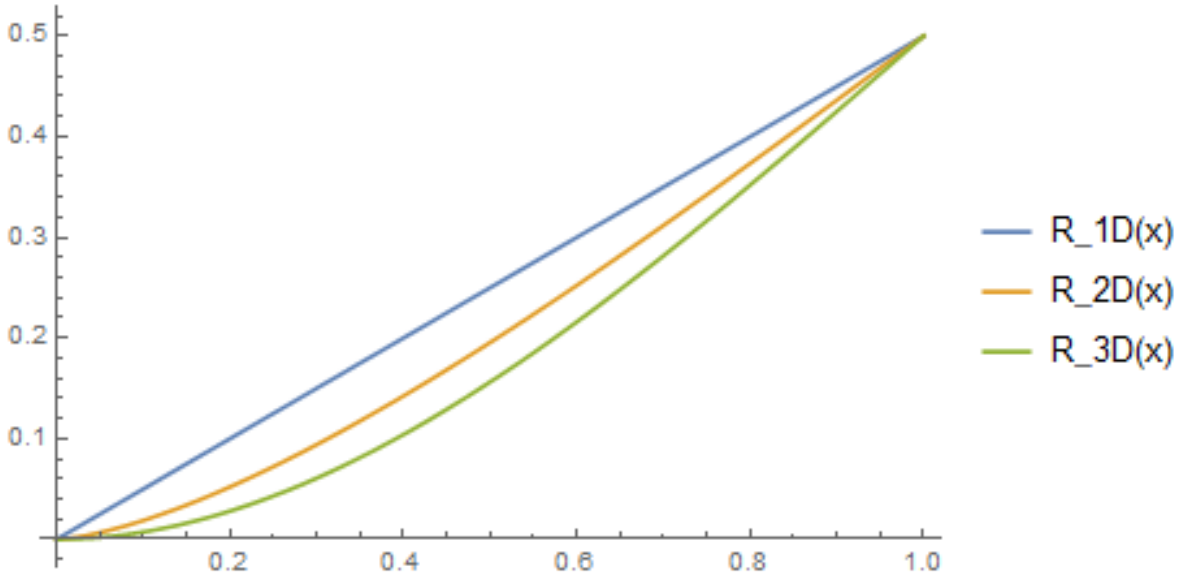

Figure B.2: Ratio of volume outside to total volume of the kernels in 1D, 2D and 3D

This plot illustrates that the 3D kernel has the largest volume inside the superconductor, thus leading to a larger peak of the current density.

Appendix C

Supplementary Plots of Infinite Superconducting Wire

Here we have supplementary plots for of all the different electrodynamic quantities plotted for the infinite superconducting wire, using both the 2D and 3D Approximated Pippard kernel. A penetration depth of $\lambda = 70$ nm was used for all the calculations.

C.1 Current Density and Vector Potential using 2D Pippard

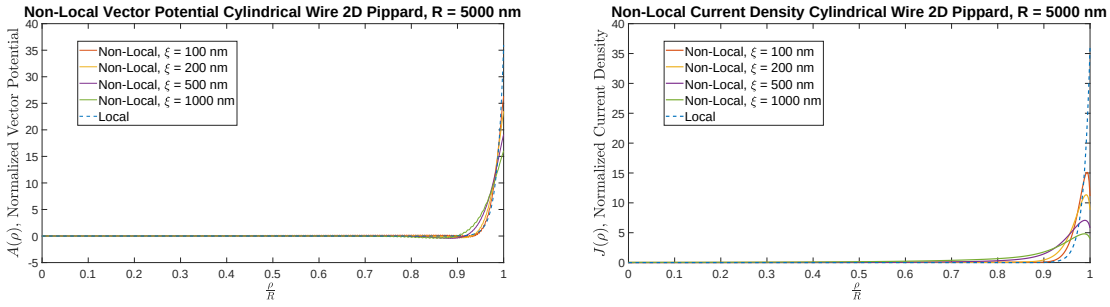

Figure C.1: $A(\rho)$ and $J(\rho)$ for different values of ξ for a superconducting cylinder with radius $R = 5000$ nm

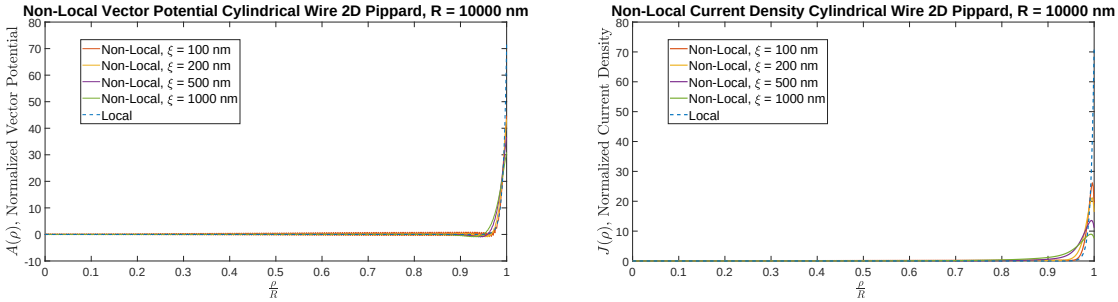

Figure C.2: $A(\rho)$ and $J(\rho)$ for different values of ξ for a superconducting cylinder with radius $R = 10000$ nm

C.2 Current Density and Vector Potential using 3D Approximated Pippard

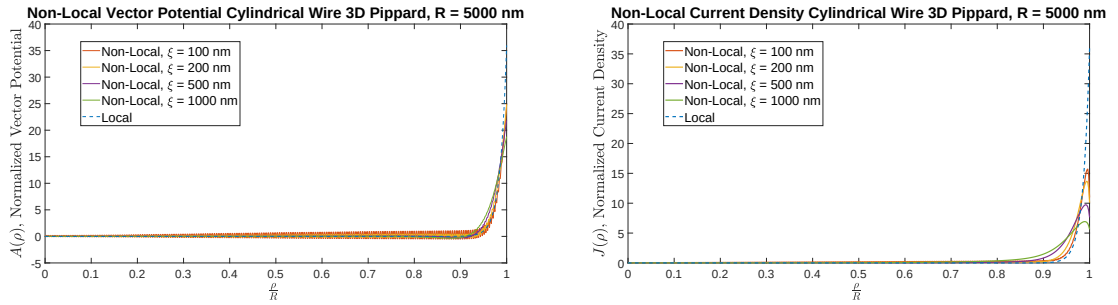

Figure C.3: $A(\rho)$ and $J(\rho)$ for different values of ξ for a superconducting cylinder with radius $R = 5000$ nm

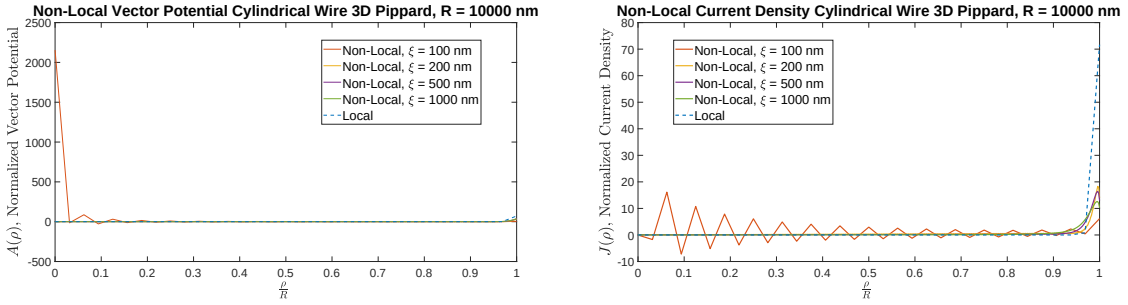

Figure C.4: $A(\rho)$ and $J(\rho)$ for different values of ξ for a superconducting cylinder with radius $R = 10000$ nm

The last figures show the complete breakdown of the numerical scheme used in this thesis.

C.3 Flux Vector and Flux Noise Power using 3D Approximated Pippard

These are the are the quantities discussed in Chapter 4:

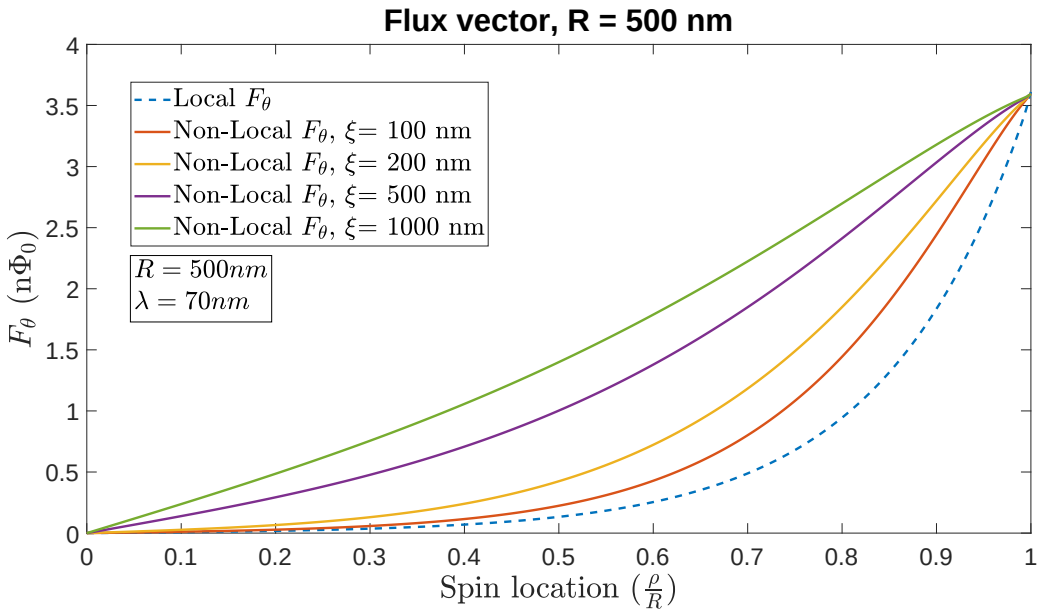

Figure C.5: Flux Vector in the Non-Local versus Local regime for $R = 500$ nm using the 3D Pippard kernel

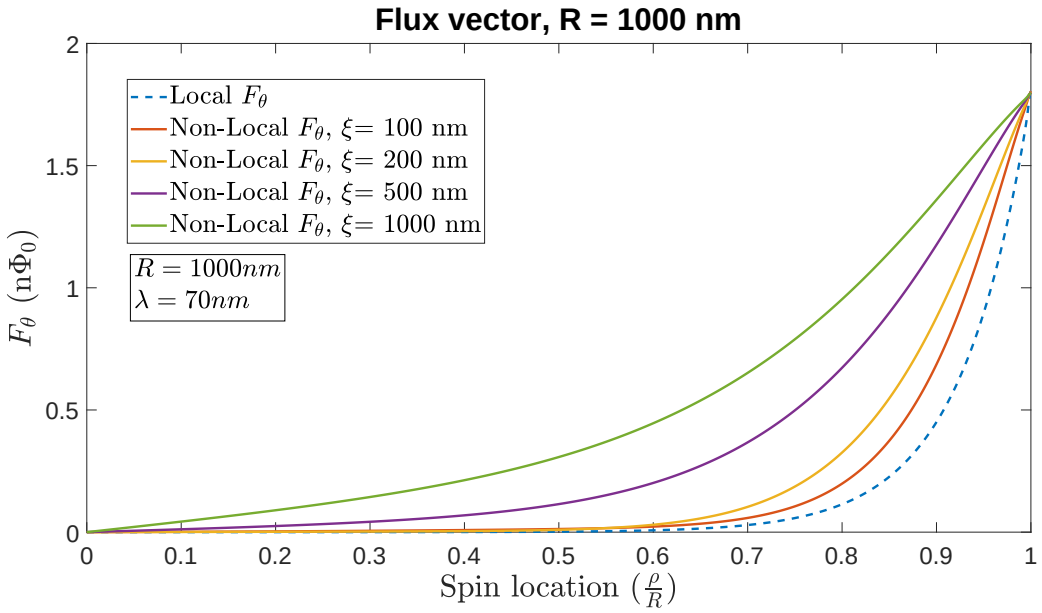

Figure C.6: Flux Vector in the Non-Local versus Local regime for $R = 1000$ nm using the 3D Pippard kernel

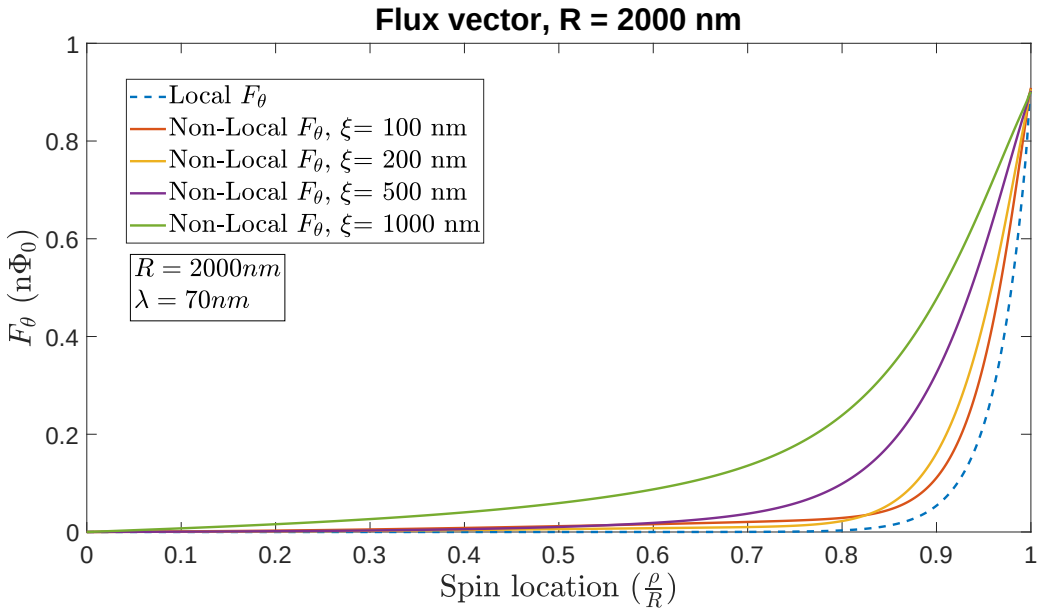

Figure C.7: Flux Vector in the Non-Local versus Local regime for $R = 2000$ nm using the 3D Pippard kernel

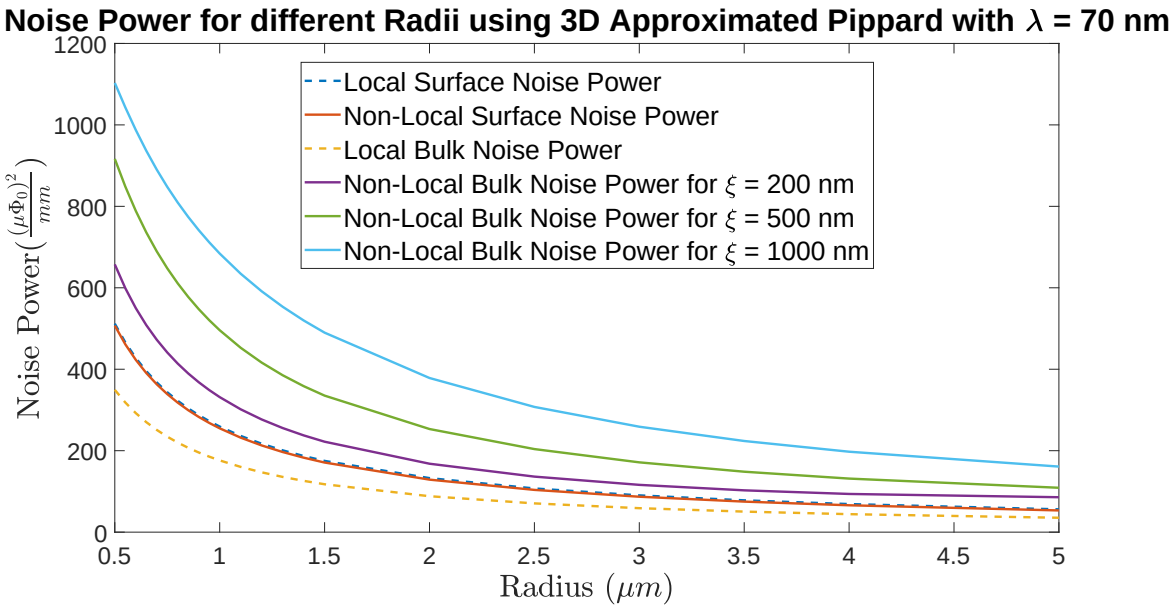

Figure C.8: Flux Noise Power for 3D Pippard with increasing non-locality

Bibliography

[1] C. W. F. Everitt, D. B. DeBra, B. W. Parkinson, J. P. Turneaure, J. W. Conklin, M. I. Heifetz, G. M. Keiser, A. S. Silbergleit, T. Holmes, J. Kolodziejczak, M. Al-Meshari, J. C. Mester, B. Muhlfelder, V. G. Solomonik, K. Stahl, P. W. Worden, W. Bencze, S. Buchman, B. Clarke, A. Al-Jadaan, H. Al-Jibreen, J. Li, J. A. Lipa, J. M. Lockhart, B. Al-Suwaidan, M. Taber, and S. Wang. Gravity probe b: Final results of a space experiment to test general relativity. *Phys. Rev. Lett.*, 106:221101, May 2011.

[2] S. J. Williamson, D. Brenner, and L. Kaufman. Biomedical applications of squids. *AIP Conference Proceedings*, 44(1):106–116, 1978.

[3] R. Kleiner, D. Koelle, F. Ludwig, and J. Clarke. Superconducting quantum interference devices: State of the art and applications. *Proceedings of the IEEE*, 92(10):15341548, Oct 2004.

[4] S. Boixo, T. F. Rønnow, S.V. Isakov, Z. Wang, D. Wecker, D. A. Lidar, J. M. Martinis, and M. Troyer. Evidence for quantum annealing with more than one hundred qubits. *Nature Physics*, 10(3):218224, 2014.

[5] J. Preskill. Reliable quantum computers. *Proceedings of the Royal Society A: Mathematical, Physical and Engineering Sciences*, 454(1969):385410, Aug 1998.

[6] Roger H. Koch, David P. Divincenzo, and John Clarke. Model for1/f flux noise in squids and qubits. *Physical Review Letters*, 98(26), 2007.

[7] R. De Sousa. Dangling-bond spin relaxation and magnetic 1f noise from the amorphous-semiconductor/oxide interface: Theory. *Physical Review B*, 76(24), Jun 2007.

[8] T. Lanting, M. H. Amin, A. J. Berkley, C. Rich, S.-F. Chen, S. Laforest, and R. de Sousa. Evidence for temperature-dependent spin diffusion as a mechanism of intrinsic flux noise in squids. *Physical Review B*, 89(1), Jul 2014.

[9] S. Laforest and de Sousa, R. Flux-vector model of spin noise in superconducting circuits: Electron versus nuclear spins and role of phase transition. *Physical Review B*, 92(5), Mar 2015.

[10] A. Mourachkine. *Room-Temperature Superconductivity*. Cambridge International Science Publishing, 2004.

[11] R. Perry and J. L. Sloop. Liquid hydrogen as a propulsion fuel, 1945-1959. *Technology and Culture*, 21(1):136, 1980.

[12] H. K. Onnes. The resistance of pure mercury at helium temperatures. *Communications of the Physical Laboratory at the University of Leiden*, 12:120, 1911.

[13] W. Meissner and R. Ochsenfeld. Einneuer effektbeieintritt der supraleitfahigkeit. *Naturwissenschaften*, 21:787–788, 1933.

[14] V. L. Ginzburg and L. D. Landau. On the theory of superconductivity. *Zh. Eksperim. Teor. Fiz.*, 20.

[15] J. Bardeen, L. N. Cooper, and J. R. Schrieffer. Theory of superconductivity. *Phys. Rev.*, 108:1175–1204, Dec 1957.

[16] A.B. Pippard. Field variation of the superconducting penetration depth. *Proceedings of the Royal Society of London A: Mathematical, Physical and Engineering Sciences*, 203(1073):210–223, 1950.

[17] A. B. Pippard. An experimental and theoretical study of the relation between magnetic field and current in a superconductor. *Proceedings of the Royal Society A: Mathematical, Physical and Engineering Sciences*, 216(1127):547568, 1953.

[18] G. E. H. Reuter and E. H. Sondheimer. Theory of the anomalous skin effect in metals. *Nature*, 161(4089):394395, 1948.

[19] M. Tinkham. *Introduction to Superconductivity*. Dover Publications, 2nd edition, 2004.

[20] T. E. Faber and A. B. Pippard. The penetration depth and high-frequency resistance of superconducting aluminium. *Proceedings of the Royal Society A: Mathematical, Physical and Engineering Sciences*, 231(1186):336353, Jun 1955.

[21] J.R Hook and J.R. Waldram. A ginzburg-landau equation with non-local correction for superconductors in zero magnetic field. *Proceedings of the Royal Society of London A: Mathematical, Physical and Engineering Sciences*, 334(1597):171–192, 1973.

[22] B. D. Josephson. Possible new effects in superconductive tunnelling. *Physics Letters*, 1(7):251253, 1962.

[23] Y. Makhlin, G. Schön, and A. Shnirman. Quantum-state engineering with josephson-junction devices. *Reviews of Modern Physics*, 73(2):357400, Aug 2001.

[24] T. Van Duzer and C.W. Turner. *Principles of Superconductive Devices and Circuits*. Bibliyografya Ve Indeks. Prentice Hall, 1999.

[25] J.D. Jackson. *Classical Electrodynamics*. John Wiley and Sons, 3rd edition, 1999.

[26] K. E. Atkinson and L. F. Shampine. Algorithm 876: Solving fredholm integral equations of the second kind in matlab. *ACM Trans. Math. Softw.*, 34(4):21:1–21:20, July 2008.